

A STUDY OF DIFFERENT FEM TECHNIQUES FOR
MODELLING 3D METAL CUTTING PROCESS WITH AN
EMPHASIZE ON ALE AND CEL FORMULATIONS

By

SI SUN, B.ENG

A Thesis Submitted

to

the School of Graduate Studies

in Partial Fulfilment of the Requirements for

the Degree Master of Applied Science

McMaster University

© Copyright by Si Sun, December 2014

MASTERS OF APPLIED SCIENCE (2014)

McMaster University

(Mechanical Engineering) Hamilton Ontario

TITLE:

AN STUDY OF DIFFERENT FEM TECHNIQUES FOR MODELLING
3D METAL CUTTING PROCESS WITH AN EMPHASIZE ON ALE
AND CEL FORMULATIONS

AUTHOR: Si Sun, B. Eng. (McMaster University)

SUPERVISORS: Dr. Eu-Gen Ng

NUMBER OF PAGES: xv, 119

ABSTRACT

Finite element(FE) method has been used to model cutting process since 1970s. However, it requires special techniques to cope with the difficulties in simulating extremely large strain when compare to static or small deformation problems. With the advancement of FE techniques, researchers can now have a deeper insight of the mechanism of material flow and chip formation of metal cutting process. Even the stagnation effect of the workpiece material in front of the cutting edge radius can be captured by using FE techniques such as Remeshing and Arbitrary Lagrangian Eulerian(ALE) formulation. However most of this models are limited to plane strain assumption which means they are 2-dimensional.

Although 3D models are existing in the literatures, most of them employ Remeshing technique which is very computationally intensive and has many critics regarding its accuracy due to its frequent remeshing and mapping process. The rest of the 3D models employ Lagrangian formulation. The 3D models by Lagrangian formulation have the same limitations and drawbacks as in 2D models, as it requires failure criteria and in most of the cases predefined partition surfaces are also required. ALE technique on the other hand resolves all the drawbacks of the other formulations, it not only

inherits the advantages of the other techniques but also has its own unique advantages such as it can simulate a longer time span up to couple seconds more economically by fixing the number of elements used. Although it's commonly accepted that ALE formulation is superior to other formulations of techniques in modeling metal cutting process, its usage is only limited to 2D models. Limited 3D ALE metal cutting models is available in the literature. Thus the main objective of this research is to explore the possibility of building a 3D metal cutting model with ALE formulation. The reliability and limitations will also be studied.

Furthermore, Couple Eulerian-Lagrangian(CEL) formulation is a recent developed formulation that has a lot of potential in modeling metal cutting process in 3D. It will be compared with ALE models to study its potential and limitations in modeling metal cutting process.

A new frictional model will also be proposed, which suggests that the frictional phenomenon in metal cutting is a consolidated effect of both friction between material interface and shear yield of the workpiece material. This idea provide a brand new perspective of viewing the friction phenomenon of metal cutting compared to those existed models.

ACKNOWLEDGEMENT

If it wasn't because my parents who encouraged me and supported me I wouldn't have accomplished my studies and researches. My parents financially supported me during my undergraduate study so I can focus on what I'm interested in. I would like to say thank you to them and I really love them.

I wish to express my sincerest gratitude to my supervisor Dr. Eugue Ng for his inspiring advice, patient guidance and motivational encouragement. The research area that Dr.Ng led me to was really interesting and the skills I learned from it will help me a lot in my future career. I am greatly thankful to Youssef Ziada and Keyvan for their software and laboratory assistance. Many thanks also go to McMaster University, NSERC and Canadian Network for Reserch and Innovation for Machining (CANRIMT) for its financial support.

Finally, special thanks to my future girlfriend who never shows up and distracts me during the two years of my graduate studies and researches.

ABSTRACT	III
ACKNOWLEDGEMENT	V
LIST OF TABLE CAPTIONS.....	XII
NOMENCLATURE AND LIST OF SYMBOLS.....	XIII
CHAPTER 1 INTRODUCTION	1
1.1 BACKGROUND	1
1.2 METHODS FOR MODELING METAL CUTTING	1
1.3 FINITE ELEMENT FORMULATIONS AND TECHNIQUES	4
1.3.1 Lagrangian Formulation.....	4
1.3.2 Remeshing.....	6
1.3.3 Arbitrary Lagrangian-Eulerian (ALE)	7
1.3.4 Couple Eulerian-Lagrangian (CEL).....	8
1.4 OBJECTIVES	12
CHAPTER 2 LITERATURE REVIEW	15

2.1	EXISTING FE MODELS.....	15
2.2	MATERIAL MODELS.....	21
2.3	FRICTION MODELS	24
CHAPTER 3	DEVELOPING OF 3D MODELS	31
3.1	2D MODELS.....	33
3.1.1	ALE Model	35
3.1.2	CEL Model.....	41
3.1.3	Comparison of Simulation Results	45
3.2	SEMI-3D MODELS.....	52
3.2.1	ALE Model	54
3.2.2	CEL Model.....	61
3.2.3	Comparison of Simulation Results	63
3.3	FULL-3D MODEL.....	66
3.3.1	Full 3D ALE Model	67
3.3.2	Full 3D CEL Model	85
3.3.3	Comparison of Simulation Results	89

CHAPTER 4	DISCUSSIONS.....	91
4.1	NATURAL TRANSITION FRICTION MODEL.....	91
4.2	MATERIAL MODEL.....	103
4.3	ROBUSTNESS AND LIMITATIONS OF MESH SMOOTH METHODS.....	105
4.4	LIMITATIONS OF CEL FORMULATION	108
4.5	PROPOSED PROCEDURE FOR BUILDING 3D ALE CUTTING MODEL	109
4.6	CONSIDERATIONS OF EFFICIENCY VS. EFFECTIVENESS	111
CHAPTER 5	CONCLUSIONS AND FUTURE WORK.....	113
	REFERENCES.....	116

LIST OF FIGURES CAPTIONS

Figure 1 Merchant's circle [2]	3
Figure 2 Volume smoothing method [5]	7
Figure 3: A 2D example of material motion and mesh motion in CEL [7]	9
Figure 4 Eulerian material represented by VF in a Eulerian mesh grid [5]	10
Figure 5 The definition of the penetration for a void element [7]	11
Figure 6 Four types of chip formation: (a) Continuous, (b) Continuous with built up edge, (c) Discontinuous, (d) Segmental	12
Figure 7 Continuous chip formation by Lagrangian formulation [10]	15
Figure 8 (a) Boundary conditions, regional partitioning scheme, and material flow, (b) Chip formation	16
Figure 9 Geometry of the FE model showing (a) 3-D viewing, (c) cross-sectional view showing element distribution [6]	17
Figure 10 Chip formation by CEL formulation. The contours display the equivalent plastic strain [7]	18
Figure 11 (a) 3D turning model [13] (b) 3D drilling model [14] (c) 3D oblique cutting model [16]	18
Figure 12 3D turning model with predefined parting planes [17]	19
Figure 13 Proposed initial mesh assembly of the ball nose end mill model [17]	20
Figure 14 (a) 3D milling operation geometry (b) simulation result [18]	21
Figure 15 Flow stress versus temperature for AISI 1045 at strain rate of 7.5×10^3 /s. The dotted lines represent the models, the markers are the experimental data [21]	23
Figure 16 Temperature factor versus temperature used in Eq.5 [22]	24
Figure 17 Curves representing normal and frictional stress distributions on the tool rake face [27]	27
Figure 18 Measured normal and shear stress distribution on cutting tool rake face in orthogonal cutting of LCFCS using the split-tool method [24]	30
Figure 19 2D Cutting configuration	34
Figure 20 Eulerian surfaces in 2D ALE model	36
Figure 21 Boundary conditions and adaptive mesh constraints of 2D ALE model	37
Figure 22 chip formation by ALE formulation at different moment of time (Mises stress contour)	40
Figure 23 construction of 2D CEL model	42
Figure 24 chip formation by CEL formulation at different moment of time (Mises stress contour)	44
Figure 25 Mesh Topology of (a) ALE and (b) CEL models	46
Figure 26 Von Mises stress distribution of (a) ALE and (b) CEL models	47
Figure 27 Temperature Distribution of (a) ALE and (b) CEL models	48

Figure 28 Path along which the data are plotted	48
Figure 29 Stresses comparison of ALE and CEL	49
Figure 30 Velocities comparison of ALE and CEL	49
Figure 31 Temperature comparison of ALE and CEL	50
Figure 32 Strains comparison of ALE and CEL	50
Figure 33 Forces comparison of ALE and CEL	52
Figure 34 (a) 2D cutting configuration, (b) semi-3D cutting configuration	53
Figure 35 Expected chip geometry from semi-3D cutting	53
Figure 36 Solid Element Geometries	55
Figure 37 (a) cube meshed by hex. (b) cube meshed by tetra	57
Figure 38 Cross sections of semi-3D workpiece	58
Figure 39 Plane partitions transform from middle plane to surface plane	58
Figure 40 Assembly of semi-3D ALE model	59
Figure 41 Time lapse from 0s to 0.001s for semi-3D ALE	60
Figure 42 Top view of the workpiece without the tool at 0s and 1ms	61
Figure 43 Assembly of semi-3D CEL model	62
Figure 44 Time lapse from 0s to 0.001s for semi-3D CEL, stress contour	63
Figure 45 Stress distribution for (a) ALE, (b) CEL semi-3D model	64
Figure 46 Cutting/Feeding forces vs. time of ALE and CEL model	65
Figure 47 Chip cross sections	66
Figure 48 Full 3D configuration, turning with cutting nose	67
Figure 49 Volumetric Poly Cube Deformation [35]	70
Figure 50 Two cutting areas in Full 3D configuration [38]	71
Figure 51 (a) Expected workpiece and chip geometry (b) simplified initial geometry	72
Figure 52(a) Mesh generated automatically by ABAQUS/CAE (b) Enlarged elements	74
Figure 53 (a) Workpiece initial geometry (b) a geometry partitioned into cells (c) meshed workpiece front view with tool (d) meshed workpiece rear view without tool	75
Figure 54 (a) Simplified ALE mesh before deformation (b) Simplified ALE mesh during deformation	77
Figure 55 New design of the initial geometry	79
Figure 56 (a) New initial workpiece geometry design and its partitions, (b) Pre-machined surface & newly machined surface, (c) Transition surface & co-plane surface	80
Figure 57 Structural meshed initial geometry	80
Figure 58 BC's & AMC's of full-3D ALE model, front/right/top views	82
Figure 59 3D ALE model at different times with portion of the chip hidden	83
Figure 60 Three critical factors of 3D ALE model	84

Figure 61 Full 3D ALE assembly (a) wireframe view and (b) mesh view	86
Figure 62 BC's for full-3D ALE model in step-1(a) and step-2(b), front/left/top views	87
Figure 63 Simulation result of full-3D CEL model at time frame of 0s, 37.5us, 187us and 412us	88
Figure 64 Chip formation at 525 μ s by different views	89
Figure 65 Predicted forces of both ALE and CEL 3D models	90
Figure 66 Stress distributions from rear tool forces: AISI C1045 [32]	93
Figure 67 Distribution of normal stress and shear stress along the contact length of mild steel [31]	94
Figure 68 Predicted contact stress [43]	96
Figure 69 Predicted contact stress [44]	96
Figure 70 Predicted contact stress [42]	96
Figure 71 Apparent friction coefficient vs. sliding velocity [40]	97
Figure 72 Expected normal stress and shear stress along contact length by natural transition model	99
Figure 73 Velocity distribution of natural transition friction model	100
Figure 74 Self-contact that bend the chip over	101
Figure 75 Flow stress versus temperature for AISI1045 at strain rate of 7.5.	104
Figure 76 Velocity contour plot reveals the BUE	105
Figure 77 Test of the mesh smooth method in 3D	106
Figure 78 2D example of the problematic mesh smooth method	107
Figure 79 Surface approximation base on volume fraction	108
Figure 80 Better boundary approximation with finer mesh	109
Figure 81 Flow chart of proposed 3D ALE modeling procedure	110

LIST OF TABLE CAPTIONS

Table 1 Friction constants from split-tool test for equation (11) [26]	30
Table 2 Unit System	31
Table 3 Material Properties for Workpiece and Tool	32
Table 4 2D Cutting Model parameters	34
Table 5 Semi-3D Cutting Model Cutting Conditions	53
Table 6 3D Cutting Model Cutting Conditions	67
Table 7 Predicted results of ALE, CEL models at time=0.3ms.	90
Table 8 Extracted shear stress and normal stress data from plot	99
Table 9 Parameters for equation (4) for AISI1045	103
Table 10 Simulation informations fro each models	112

NOMENCLATURE AND LIST OF SYMBOLS

w : Width of cut (mm)

v : Cutting speed (m/min)

v_c : Chip velocity (m/min)

f : Feed rate (mm/rev)

t : Undeformed chip thickness (mm)

t_c : Chip thickness (mm)

PSZ : Primary shear zone

SSZ : Secondary deformation zone

R : Resultant force (N)

F_c : Cutting force (N)

F_t : Thrust force (N)

F_z : Axial force (N)

F_s : Shear force (N)

F_r : Friction force (N)

α : Tool rake angle (deg)

β : Friction angle (deg)

φ : Shear angle (deg)

μ : Local coefficient of friction COF (-)

$\bar{\mu}$: Overall coefficient of friction COF (-)

COF : Coefficient of friction (-)

BUE : Built-up edge

R_e : Tool cutting edge radius (μm)

R_n : Tool cutting nose radius (μm)

l_p : Sticking region along the tool-chip interface (mm)

l_c : Contact length along the tool-chip interface (mm)

τ_{fric} : Shear stress (MPa)

σ_n : Normal stress (MPa)

τ_{max} : Maximum shear stress (MPa)

LF : Lagrangian Formulation

ALE : Arbitrary LagrangianEulerian

FE : Finite Element

m : (When used in friction models) Shear friction factor (-)

n : (When used in friction models) Constant for variable shear friction model (-)

k : Shear flow stress of workpiece material (MPa)

σ_y : Material yield stress (MPa)

AISI : American Iron and Steel Institute

A : (When used in J-C equation) Material constant (MPa)

B : (When used in J-C equation) Material constant (MPa)
 C : (When used in J-C equation) Strain rate coefficient (-)
 $\bar{\epsilon}_{pl}$: Plastic strain (-)
 $\dot{\epsilon}_{pl}$: Plastic strain rate (s-1)
 $\dot{\epsilon}_0$: (When used in J-C equation) Reference plastic strain rate (s-1)
 T : Temperature (°C)
 T_{ref} : (When used in J-C equation) Reference temperature (°C)
 T_{melt} : Workpiece material melting temperature (°C)
 m : (When used in J-C equation) Thermal index (-)
 n : (When used in J-C equation) Strain hardening index (-)
 a : Blue brittleness constant in modified J-C equation
 E : Young's Modulus (GPa)
 ρ : Density (kg m-3)
 α : (When used for material property) Thermal expansion (°C-1)
 cp : Specific heat capacity (J kg-1 °C-1)
 k : (When used for material thermal property) Thermal conductivity (W m-1 °C-1)
 k : (When used to describe structure dynamic behavior) Stiffness (N mm-1)
 m : (When used to describe structure dynamic behavior) Mass (kg)

CHAPTER 1 INTRODCUTION

1.1 Background

In the world of manufacturing, turning, milling and drilling are the most commonly used machining operations. No matter which operation is considered the physics of the metal cutting is the same, i.e. it is the process when the edge of the tool engages the workpiece and removes the material to generate chip and newly machined surface of the workpiece. Thus understanding metal cutting process and achieving the ability of predicting the outcomes of such process will essentially improve productivity, reduce cost and obtain desirable surface quality of the products. For examples, the ability to predict stresses acting on the tool can be used to optimize the tool design to achieve higher product precision and the ability to predict tool life can prevent catastrophic tool failures and reduce finished machined part rejection.

1.2 Methods For Modeling Metal Cutting

The study of the metal cutting has lasted for more than a century.

According to Chen the earliest scientific studies of metal cutting was from Cocquilhat in 1851 [1]. Cocquilhat's experiments were to determine the work required to remove a unit volume of material. Mallock established the shear plane model which is the basis of the modern analytical models of metal cutting in 1881. From here, Merchant further studied the mechanics of metal cutting and proposed Merchant's Circle as showed in Figure 1 which is an intuitive tool to study the relationships between the accompanying forces, shear plane, chip thickness. Merchants work was further developed by Lee and Shaffer and Oxley to improve the ability of their analytic models to predict the shear plane [1]. Although the analytic models are capable of predicting the geometries of the chip, tool forces even temperatures by 1970's, they don't provide detailed information such as the stress distribution, temperature distribution and residual stresses.

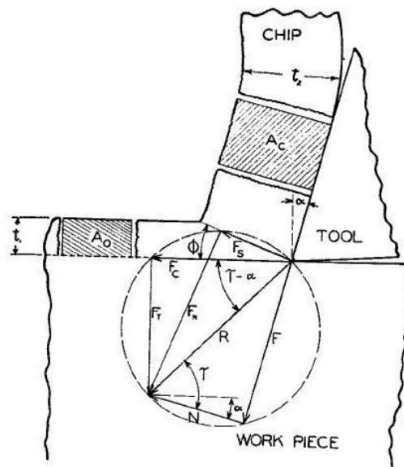


Figure 1 Merchant's circle [2]

Metal cutting process in the real world is a very complex three dimensional problem. It involves very high strain, strain rate and temperature within a very small volume. It's almost impossible for conventional analytical methods to achieve a solution for a three dimensional metal cutting process. After 1950's, with the advancement of numerical methods, finite element technique became the new hope for resolving this problem and together with the enhancement of computer processor architecture, simulating the metal cutting process became possible with finite element method. With the help of commercial FE solvers such as ABAQUS, developing FE models became much easier than before. Many 2D FE cutting models have been proposed and verified, but challenges still exist in constructing 3D numerical cutting models. In this research, FEM will be utilized to study the process of metal cutting and

constructing a reliable 3D cutting model will be the focus.

1.3 Finite Element Formulations And Techniques

The existing FE formulations for simulating the metal cutting process can be categorized into five categories which are: Lagrangian, Eulerian, Remeshing, Arbitrary Lagrangian Eulerian (ALE) and Coupled Eulerian Lagrangian (CEL). The relationship is subtle. The Lagrangian is the fundamental. The others utilized different remeshing principles from the Lagrangian formulation to achieve the same goal of element distortion control for large strain problems such as metal cutting and forging processes. Lagrangian, remeshing and ALE have been heavily used in modeling metal cutting in 2D or 3D, while CEL has just started being applied to metal cutting model and the reliability of CEL and its advantages in modeling metal cutting has not yet been well investigated.

1.3.1 Lagrangian Formulation

Lagrangian formulation is probably earliest and most commonly used formulation in metal cutting simulations. It is straight forward to use and the motion of the material is easy to visualize as the mesh is the representation

of the material. However, when simulating the cutting process the large strain at the cutting edge of the tool will cause the element to distort excessively. Severe distorted element will result in unreliable prediction and even induce the simulation to terminate. In order to address this problem, failure criteria are required to delete severe distorted elements or to separate nodes before distorted elements can cause any problems. However there is one major issue with failure criterion, that is difficult to acquire and lacks repeatability, parameters have to be tuned every time according to the new cutting parameters to generate a reasonable solution. Due to the nature of mesh motion of Lagrangian formulation, it can hardly capture two of the vital areas of metal cutting which are the stagnation zone and sticking zone in front of the cutting edge. Many authors[3], [4] assert that a predefined parting line is required for Lagrangian formulation when simulating metal cutting process, but this is not true. A predefined parting line is only necessary when a very regular new surface following the cutting tool has to be generated. A new surface can be generated anyway without a predefined parting line if the failure criterion is assigned to the entire workpiece, but it might be very rough because the elements which are deleted base on the failure criterion may not align in a straight path.

1.3.2 Remeshing

Remeshing is the intuitive solution for controlling the element distortion of Lagrangian formulation. The idea is simple, if the mesh is highly distorted during the simulation then a new mesh should be generated which is based on the deformed geometry of the workpiece. A process known as mapping will transfer the solutions from the lightly distorted mesh to the new mesh basing on their relative position in space, interpolations usually take place during this process since the nodes of the old mesh and those of the new mesh don't usually coincide. After the solutions including the stress, stain and temperature etc. are mapped to the new mesh the simulation is able to continue with refreshed and less distorted elements. There is no strict limitation for the topology of the new mesh, as long as it shares the same geometry boundary with the old mesh. The new mesh can even have different types of elements than the previous mesh if manually remeshed thus the number of elements and nodes can vary from the previous mesh to the new mesh. Due to this fact, interpolation will be employed extensively during the mapping process and the accuracy of the solution will thus deteriorate as the errors may accumulate after repetitive remeshing occurred [3].

1.3.3 Arbitrary Lagrangian-Eulerian (ALE)

ALE formulation can be considered as a special case of remeshing. Both ALE and remeshing have the goal of element distortion control, but ALE formulation has more strict rules for the generation of the new mesh. In remeshing the topology of the mesh can vary each time a new mesh is generated, while in an ALE simulation the same topology will be carried through the entire simulation. Instead of remeshing the deformed geometry from scratch, ALE relocates the positions of the nodes according to the mesh smoothing methods applied. One of the most common element smoothing method is referred as volume smoothing. The new position of a node is determined by a volume-weighted average of the centers of the elements adjacent to the node of interest. For example, the position of node M is determined by the position of the element centers C_1 , C_2 , C_3 , C_4 relative to node M combined with the area of each element as detailed in Figure 2.

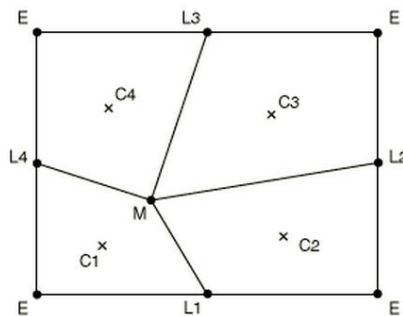


Figure 2 Volume smoothing method [5]

Same mapping process as in remeshing which will take place after the element smoothing sweep is finished. Due to the element smoothing method principle of ALE, it appears that the nodes are floating over the material which is in fact associated with all the properties and solutions. In another word, the material is free to flow underneath the mesh. This unique characteristic of ALE differs itself from traditional remeshing and make it very suitable for simulating problems with flow of material such as extruding, rolling and of course metal cutting. Furthermore, with Eulerian boundaries which allow material to enter via the boundary of elements, ALE formulation is able to simulate a dynamic steady state process for a very long period with a fixed number of elements which is not possible if remeshing technique is used. This characteristic will be discussed in more details in Chapter 3.

1.3.4 Couple Eulerian-Lagrangian (CEL)

CEL formulation is similar to ALE, in which the relocation of nodes and the mapping process of solution will happen after Lagrangian computations. "Eulerian FE formulation involves a Lagrangian step with an additional advection step" [6]. "During the Lagrangian phase of the time increment nodes are assumed to be temporarily fixed within the material, and

elements deform with the material. During the Eulerian phase of the time increment deformation is suspended, elements with significant deformation are automatically remeshed" [5]. Such process is illustrated in Figure 3. The mesh is usually designed as a grid in which all the nodes fixed in space. During the relocation process, i.e. Eulerian step will always move the nodes to their original positions, thus it seems like the mesh doesn't move at all.

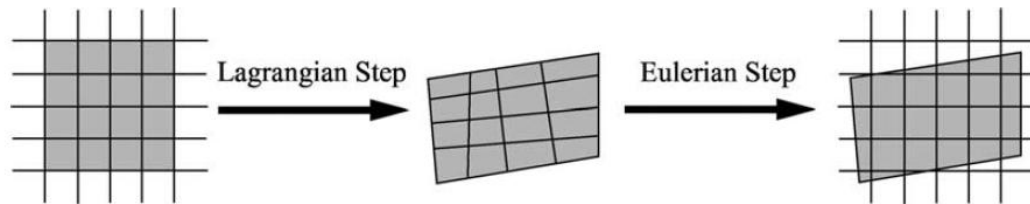


Figure 3: A 2D example of material motion and mesh motion in CEL [7]

The most unique characteristic of CEL is the definition of free surfaces. The boundary of the material doesn't coincide with the boundaries of elements. In CEL simulations elements can be void, partially occupied or fully occupied by material. The volume of the material in an element is measured by volume fraction, which is the volume of the material divided by the total volume of the element. An element which is fully occupied by material has a volume fraction of one of that material; a void element has a volume fraction of zero. An element can be occupied by more than one material

simultaneously. The sum of the volume fractions of all the materials including the "void" material in an element is always one. Figure 4 shows a disc being represented by volume fraction number. Since the free surface of the Eulerian material doesn't correspond to any boundaries of the elements and approximation of the material boundary/free surface is computed basing on the volume fractions of all the elements during each time increment.

0.0	0.0	0.0	0.0	0.0	0.0
0.0	0.32	0.91	0.91	0.32	0.0
0.0	0.91	1.0	1.0	0.91	0.0
0.0	0.91	1.0	1.0	0.91	0.0
0.0	0.32	0.91	0.91	0.32	0.0
0.0	0.0	0.0	0.0	0.0	0.0

Figure 4 Eulerian material represented by volume fraction in a Eulerian mesh grid [5]

Eulerian material can not only interact with Eulerian material but can also interact with Lagrangian parts. Therefore, simulations which involve this kind of interaction are called Coupled Eulerian-Lagrangian (CEL) analyses otherwise are called Eulerian analysis if only interactions of Eulerian materials are involved. Penalty formulation is the most commonly used method due to its simplicity and robustness. The penetration of a Lagrangian body into an Eulerian element is shown in Figure 5.

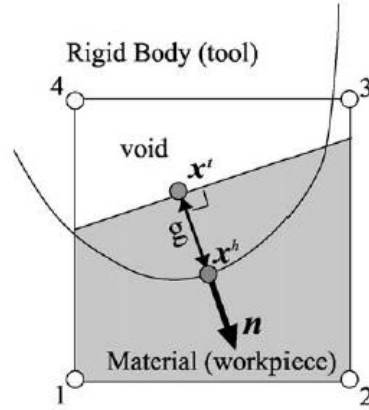


Figure 5 The definition of the penetration for a void element [7]

The contact force is expressed with Eq 1

$$\mathbf{f}^{RB} = -kgn, \quad \text{Eq. 1}$$

which is applied to the boundary nodes, where k is the penalty stiffness, and g is the penetration. The advantages of CEL formulation are obvious. The immediate benefit of having a fixed mesh in space is that element distortion is completely eliminated. On top of that, there is no need to generate a conforming mesh, in fact a regular grid of mesh usually generates the most accurate results[5]. However there are also some limitations of this developing formulation. The most immediate problem is the ambiguous definition of the material boundary, as nodes don't generally lie on the boundary of the material. Thus the reliability of the interaction between parts including thermal and frictional contacts is questionable.

1.4 Objectives

It's been several decades since FEM is applied to simulate the metal cutting process, there are many recent advances of 2D metal cutting FE models. For examples, different types of chip formations including continuous, discontinuous, segmental chips including continuous with built up edge (BUE), had been successfully simulated as showed in Figure 6.

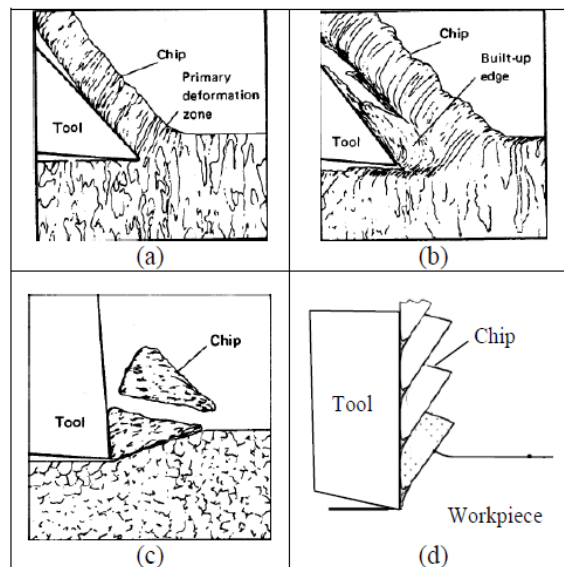


Figure 6 Four types of chip formation: (a) Continuous, (b) Continuous with built up edge,(c) Discontinuous, (d) Segmental

The effect of microstructure in the workpiece can be simulated with different material property assignments for different elements in the workpiece. The effect of cutting edge radius can also be captured with ALE or Remeshing techniques. However most of these models assume plain strain condition

which is true for laboratory setups, but not usually the case in the real world of machining. Thus 3D cutting models which have the same predictive capabilities are in need and the construction of 3D cutting models is the goal of this research. Different formulations can be applied to simulate the same cutting process. Each formulation would have its own advantages and disadvantages. For example, Lagrangian formulation can be used to address the micro-structure effects on the chip formation while Arbitrary Lagrangian-Eulerian can be used to capture the cutting edge radius's plowing effect [8, 9]. Lagrangian formulation can be easily adopted in 3D, but ALE on the other hand has never been successfully adopted in a 3D model. Thus the main objective of this study is to investigate the feasibility of constructing a 3D ALE metal cutting model that can capture the effects of the cutting edge radius and can inherit the advantages of ALE formulation in 2D. Such a 3D model can be used as the base for more challenging simulations which had been successfully conducted in 2D models such as tool wear simulations and residual stress simulations.

Recent developed Couple Eulerian-Lagrangian formulation will also be studied to determine its reliability and potential applications in modeling 3D metal cutting process. In summary the objective of this research is not to improve the predictive capabilities of FE models but to expand the

current modeling techniques which can be applied to simulate 3D metal cutting processes. This study lays the groundwork for 3D FE metal cutting models and it ought to be a start point for future research in building 3D FE models as simple as oblique cutting or as complicated as any real world cutting configurations.

CHAPTER 2 LITERATURE REVIEW

2.1 EXISTING FE MODELS

Lagrangian formulation has been widely applied in 2D FE cutting models. Figure 7 shows a typical Lagrangian cutting model where a predefined parting line is present in front of the cutting edge of the tool. Continuous chip was formed and the shear deformation represented by the shear of the elements after the material passing the shear plane can be observed [10].

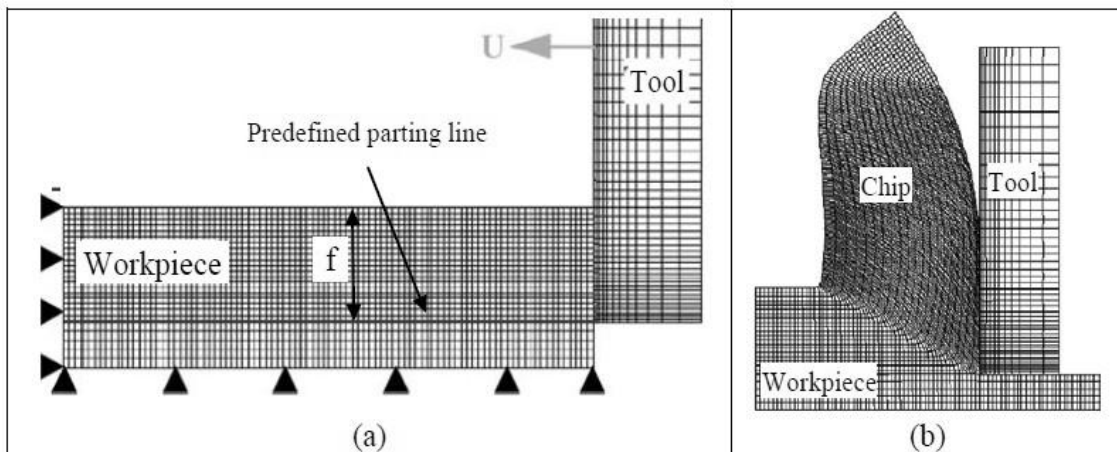


Figure 7 Continuous chip formation by Lagrangian formulation [10]

In 1999 M. R. Movahhedy successfully applied ALE formulation for orthogonal cutting models and generated good agreements between the simulations and experiments [11]. In 2006 Nasr, et al. further extended the

advantages of ALE formulation by including the cutting edge radius of the tool into the cutting model to capture the effects of the tool-edge radius on residual stresses [4]. ALE formulation eliminates the need of the predefined parting line and failure criterion but it does require more efforts to build the model due to defining the constraints of the adaptive mesh in different regions. As showed in Figure 8(a), nodes in region B are completely constrained, nodes in region A and C are only constrained in 2-direction while those in D are free and Figure 8(b) shows the result of the 2D ALE model. Materials are allowed to flow from region to region while the motion of the nodes cannot contradict to the motion of the material and the adaptive mesh constraints.

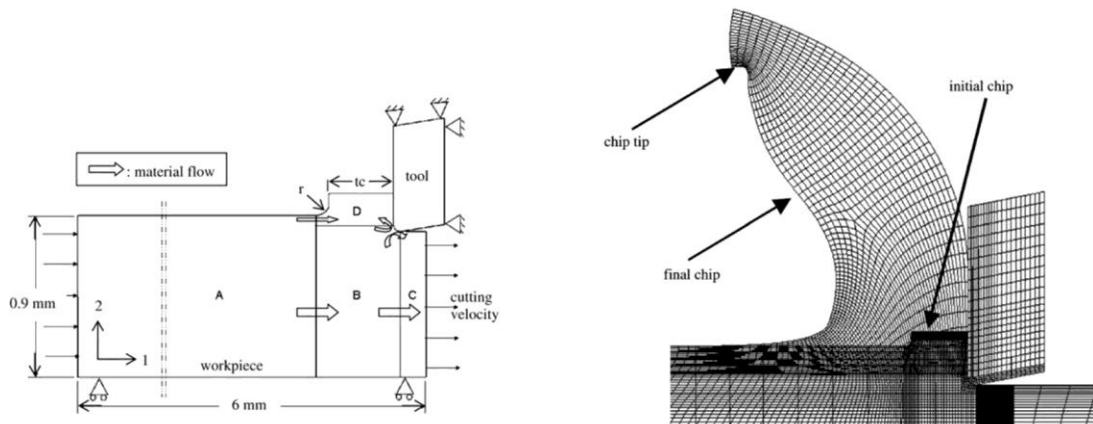


Figure 8 (a) Boundary conditions, regional partitioning scheme, and material flow, (b)

Chip formation [4]

Benson and Raczky are among those earliest researchers who attempted to apply CEL formulation to simulate orthogonal cutting process [6,

7]. The greatest concern for simulating machining is how to remove the chip from the workpiece, and both authors were able to simulate chip separation without a separation criterion by using CEL formulation [6, 7]. The assembly of the CEL model by Raczy is showed in Figure 9 while the simulation result of the CEL model by Benson is showed in Figure 10.

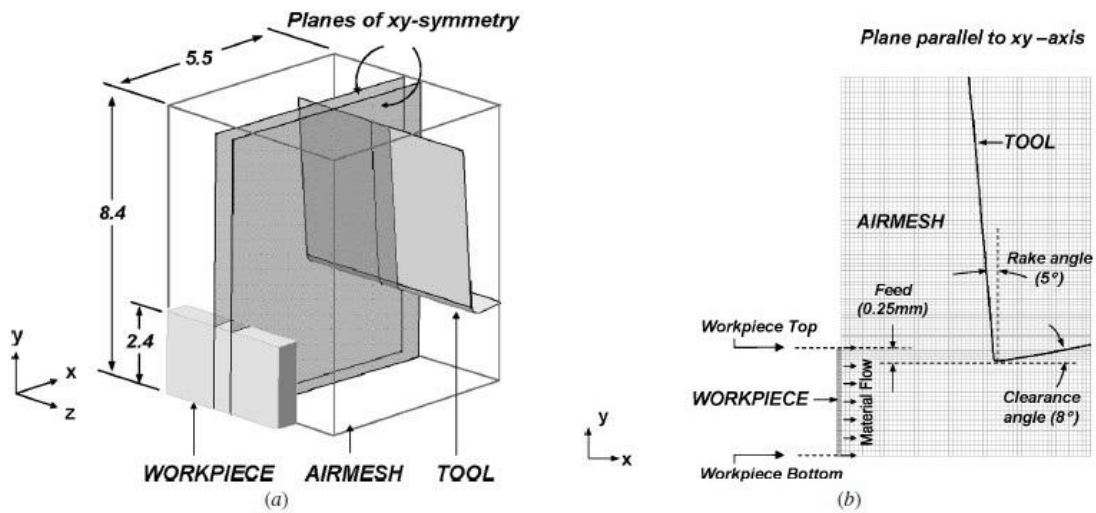


Figure 9 Geometry of the FE model showing (a) 3-D viewing, (b) cross-sectional view showing element distribution [6]

However neither of the models they built was 3-dimensional nor thermal coupled. The heat generated by plastic deformation is a very essential factor that affects the properties of the material. Since maximum temperature can easily get up to 1000 °C in high speed machining [12] which will dramatically weaken the flow stress of the material and thus affects the results of the simulation.

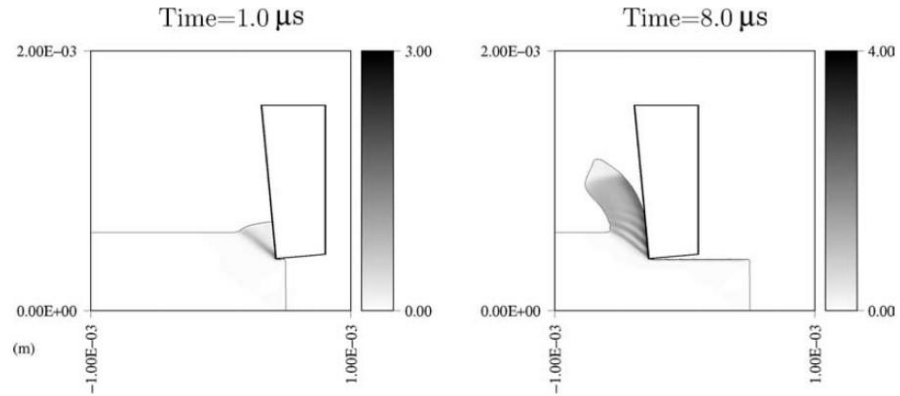


Figure 10 Chip formation by CEL formulation. The contours display the equivalent plastic strain [7]

There are also 3D metal cutting FE models. Buchkremer, Wu *et al.* simulated 3D turning operation [13], Abouridouane simulated 3D drilling process [14], while both Ceretti [15] and Fang [16] successfully built 3D oblique cutting models all with commercial FE code Deform 3D. Figure 11 shows the simulation results of those 3D models of turning, drilling and oblique cutting respectively.



Figure 11 (a) 3D turning model [13] (b) 3D drilling model [14] (c) 3D oblique cutting model [16]

With no exceptions all these models used remeshing technique and thus with

extensive remeshing processes the computation time for these models could last for weeks even with multiple CUPs [13].

Other than those models which utilize remeshing techniques are some 3D models which utilize failure criteria instead. Soo *et.al.* constructed a 3D model of turning operation with predefined parting faces as showed in Figure 12 [17].

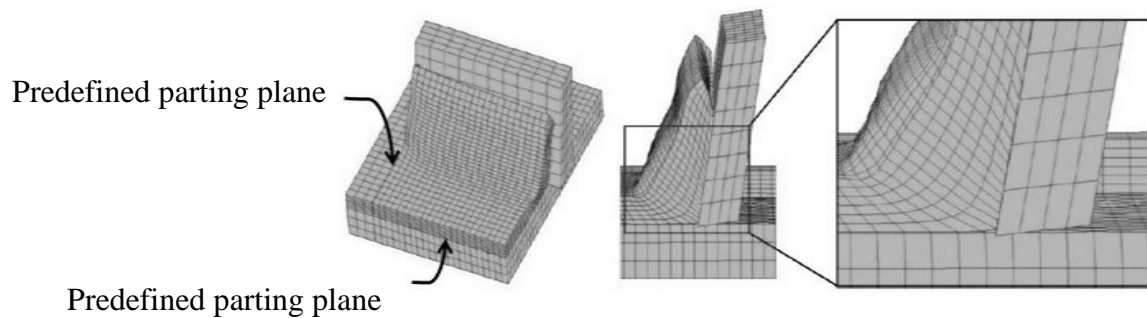


Figure 12 3D turning model with predefined parting planes [17]

In this model neither the cutting nose radius nor the cutting edge radius are present, these simplifications are not favorable in practical operations where complicated geometry are present. Thus the author mentioned that they would continue the work by using the same method to simulate more complicated operation such as end milling operation as Figure 13.

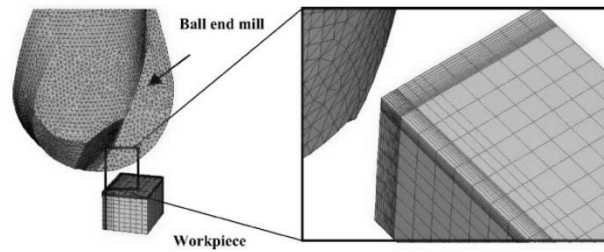


Figure 13 Proposed initial mesh assembly of the ball nose end mill model [17]

Although the author stated that they will communicate the results in future publications, related works by the same authors have never been found in the literature. The difficulty that the authors might have ran into was that the construction and the generation of the mesh of the 3D parting surface inside the workpiece for the end mill operation, such a parting surface cannot be simply represented by planes as in the simplified turning model.

Different from the work so Soo *et.al.*, A. Maurel-Pantelet *al.* applied the failure criterion to the whole workpiece instead of defining any parting surfaces when simulating the milling process [18]. The problem of such modeling method can be immediately seen in the simulation result as in Figure 14. The new surface of the workpiece after cut is very rough, and the roughness is caused by the finite size of the solid elements in the workpiece. A lot of noise will be generated due to the contact of the tool and the bumpy workpiece, the accuracy of the interactions between the tool and the workpiece as well as the simulation results are questionable.

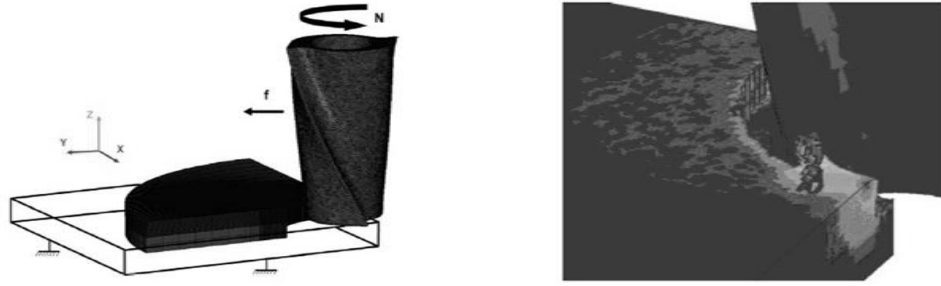


Figure 14 (a) 3D milling operation geometry (b) simulation result [18]

2.2 MATERIAL MODELS

Material model is probably the most critical input that directly affects the accuracy of the any FE simulations. In the primary and secondary shear zone of the cutting process the strain, strain rate and temperature can be as high as $4 \times 10^6/s$ and $1000\text{ }^\circ\text{C}$ respectively [19]. Thus it's commonly accepted that material model used in metal cutting simulation can only be described by empirical constructive relationship between the flow stress and influences due to the extreme conditions involved.

Among the numerous empirical equations, Johnson-Cook(J-C) [20] equation is probably the most widely used constitutive law in metal cutting simulation, where the static yield stress, σ^0 , is assumed to be of the form shown in Eq. 2.

$$\sigma^0 = (A + B\bar{\epsilon}_{pl}^n) \left[1 + C \ln \left(\frac{\dot{\epsilon}_{pl}}{\dot{\epsilon}_0} \right) \right] \left[1 - \left(\frac{T - T_{ref}}{T_{melt} - T_{ref}} \right)^m \right], \quad \text{Eq. 2}$$

where A, B, C, n, m and $\dot{\epsilon}_0$ are material parameters measured by experiments at or below the reference temperature, T_{ref} at 25 °C. $\bar{\epsilon}_{\text{pl}}$ and $\dot{\bar{\epsilon}}_{\text{pl}}$ are the equivalent plastic strain, equivalent plastic strain rate respectively. J-C equation assumes that the effects of the strain, strain rate and temperature on the yield stress are independent from each other.

Other than J-C equation there are other commonly used constitutive relations such as Zerilli-Armstrong's equations for f.c.c and b.c.c. materials [21]. The equation for b.c.c materials is written as shown in Eq.3.

$$\sigma = C_0 + C_1 \exp(-C_3 T + C_4 T \ln \dot{\bar{\epsilon}}^*) + C_5 \bar{\epsilon}^n, \quad \text{Eq. 3}$$

and for f.c.c materials as shown in Eq.4.

$$\sigma = C_0 + C_2 \bar{\epsilon}^{1/2} \exp(-C_3 T + C_4 T \ln \dot{\bar{\epsilon}}^*), \quad \text{Eq. 4}$$

Material behaviours in metal cutting conditions are generally determined by split Hopkinson pressure bar (SHPB) test. Jasper who used SHPB to determine the J-C equation parameters for AISI 1045 and concluded that J-C equation doesn't give a good description when compared to Zerilli-Armstrong constitutive relation due to the blue brittleness effect that all low carbon steels exhibit. As shown in Figure 15, the flow stress for AISI 1045 increases significantly above 500 °C. Since the furnace that the author used had a temperature limit of 600 °C this phenomenon couldn't be further investigated. This increase of flow stress is called the blue brittleness effect.

The dotted lines from J-C equation apparently failed to capture such phenomenon.

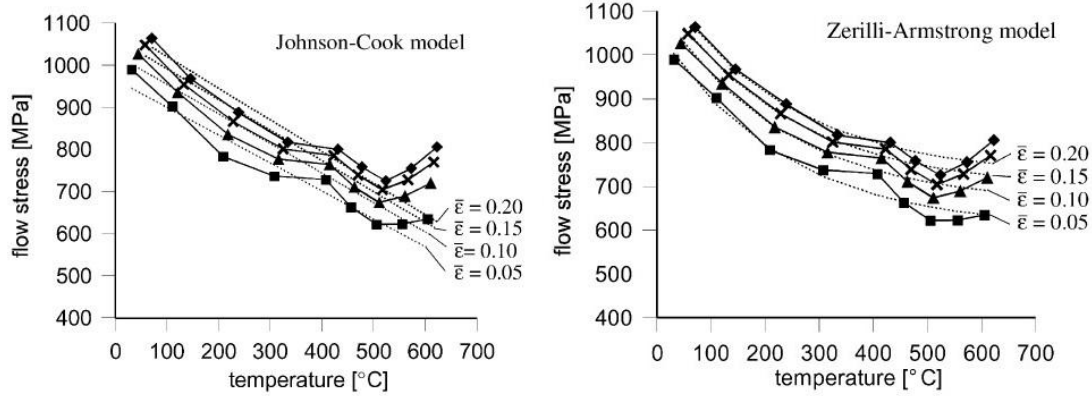


Figure 15 Flow stress versus temperature for AISI 1045 at strain rate of $7.5 \times 10^3/s$. The dotted lines represent the models, the markers are the experimental data [21]

Sartkulvanich modified J-C equation to capture the blue brittleness effect and the new equation is written as Eq.5.

$$\sigma^0 = (B \bar{\epsilon}_{pl}^n) \left[1 + C \ln \left(\frac{\dot{\bar{\epsilon}}_{pl}}{\dot{\epsilon}_0} \right) \right] \left[\left(\frac{T_{melt} - T}{T_{melt} - T_{ref}} \right) + a e^{-0.00005 (T - 700)^2} \right], \quad \text{Eq. 5}$$

where the B , C , n , a , m are the material flow stress parameters and $\dot{\epsilon}_0$ is the reference strain rate with a magnitude of 1000/s [22]. The significance of such modification can be seen in Figure 16.

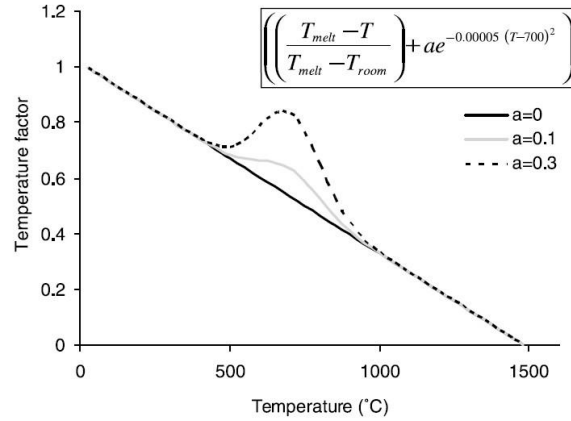


Figure 16 Temperature factor versus temperature used in Eq.5 [22]

Except using SHPB test there are also researchers who used FE model itself to calibrate the material properties under cutting conditions [23].

2.3 FRICTION MODELS

Friction model is another critical input factor used for FE metal cutting models beside material model. It has significant effect on almost every aspect of the simulation result such as the chip thickness, contact length, cutting forces, temperature distribution and stress distribution [24]. Many efforts have been devoted into developing friction models for metal cutting process. Current common friction models used to simulate metal cutting can be categorized into three types, Coulomb's friction model, split region friction model and empirical stress characteristic model.

Coulomb's Friction Model

Coulomb's friction model or also known as dry sliding model assumes that the ratio of the sliding force and normal force is a constant which is the friction coefficient as shown in Eq.6.

$$\mu = \frac{\tau_{fric}}{\sigma_n}, \quad \text{Eq. 6}$$

where τ_{fric} is the friction shear at the interface of the workpiece and tool, σ_n is the normal stress on the rake face of the tool and μ is the coefficient of friction (COF). Thus the phenomenon of friction can be described by such a friction coefficient which is independent of applied load, sliding speed, surface finish, apparent area of contact and temperature of the sliding surfaces [25]. At the current level of simulation the COF has to be estimated as an input. The most common method used to estimate the mean value of COF along the tool-workpiece contact length is by using Eq.7 derived from Merchant's circle:

$$\bar{\mu} = \frac{F_c \sin \alpha + F_t \cos \alpha}{F_c \cos \alpha - F_t \sin \alpha}, \quad \text{Eq. 7}$$

where $\bar{\mu}$, F_c , F_t and α are the mean COF, cutting force, feeding force and rake angle respectively [25]. However $\bar{\mu}$ in Eq.7 and μ in Eq.6 are not equivalent. μ is the local COF which is the ratio of the shear stress and normal stress of a point at the tool-workpiece interface [26]. While $\bar{\mu}$ is actually the ratio of the cutting force and feeding force. When α is 0 Eq.7 can

be simplified into Eq.8.

$$\bar{\mu} = \frac{F_t}{F_c}, \quad \text{Eq. 8}$$

Eq.8 calculates the mean COF of Eq.6 when the cutting force and feeding force in the metal cutting process are purely induced by the normal force and friction force on the rake face of the tool. However this assumption is not true for most of the high speed machining processes where the feed is small, usually around 0.2mm/rev, and the radius of the cutting edge and the flank face are present at the tip of the tool. Thus the cutting force is actually the sum of the normal force on the rake face, the normal force on the cutting edge radius and the friction force on the flank face of the tool, while the feeding force is the consolidated result of the friction force on the rack face and the ploughing effect at the cutting edge.

Eq.6 implies that the friction stress can increase as long as the normal stress increases. However this is not true. According to Zorev [27], the normal stress increases from zero from the far end of the tool-workpiece interface away from the cutting edge and reaches the maximum at the cutting edge, while the shear stress increases from the same start spot but saturates in the sticking region due to the maximum limit of the shear flow stress of the workpiece material at the interface, as shown in Figure 17:

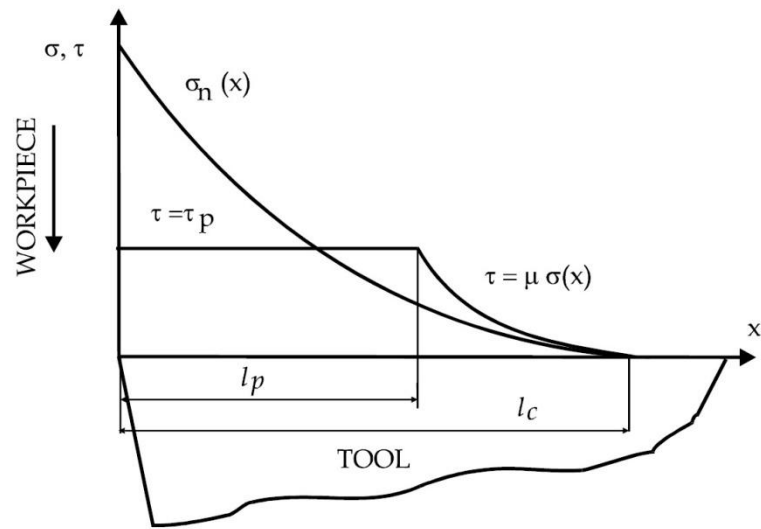


Figure 17 Curves representing normal and frictional stress distributions on the tool rake face [27]

Thus Coulomb's friction model is over simplified if employed for metal cutting process due to the extreme conditions at the tool-workpiece interface.

Thus the following friction model is proposed.

Split Region Friction Model

In this model the contact length is split into two regions and different models are applied to each model. The most immediate way to separate the sticking region and the sliding region is by using the sticking length itself. As a consequence the following model is formed:

Constant Shear friction in sticking region and Coulomb's friction in sliding region

Due to the limit of Coulomb's friction model it is only applied in the sliding region, which is the contact length l_c minus the sticking region l_p . While a constant friction shear stress which is equal to a fraction of the shear flow stress of the material is applied to the entire length of the sticking region. The model can be summarized as in equations Eq.9a and Eq.9b [24].

$$\tau_{fric} = mk \quad \text{when } 0 < x < l_p, \quad \text{Eq. 9a}$$

$$\tau_{fric} = \mu\sigma_n \quad \text{when } l_p < x < l_c, \quad \text{Eq. 9b}$$

where k is the shear flow stress of the workpiece material and m is the shear friction factor m which is a value smaller than 1.

However, at least the length of the sticking region has to be determined by experiment in order to implement this model to the simulation. The length of the sticking region can be determined by the wear mark on the tool and the total length of contact doesn't need to be pre-defined, it will form as a output in the simulation.

This model is commonly used in metal cutting FE simulations especially for those Lagrangian formulation based simulations. As m is smaller than 1, no sticking actually occurs even it's in the pre-defined sticking region, the workpiece material still slides along the rake face but the friction shear stress is limited by mk .

-Zorev's Sticking-Sliding Friction model

Zorev's friction model as known as the maximum shear stress limit friction model also separates the contact length into sticking and sliding region, however it overcomes the disadvantage of the requirement of the pre-knowledge of the sticking region length as in the previous model. This model can be summarized as in Eq.10a and Eq10b[27].

$$\tau_{fric}(x) = \tau_{max} \quad \text{when } \mu\sigma_n(x) \geq \tau_{max}, \quad \text{Eq. 10a}$$

$$\tau_{fric}(x) = \mu\sigma_n(x) \quad \text{when } \mu\sigma_n(x) < \tau_{max}, \quad \text{Eq. 10b}$$

where τ_{max} is theoretically the workpiece shear flow stress at the interface of workpiece and tool, but is practically estimated as an input.

Empirical Stress Characteristic Model

Instead of split the contact length into different region and treat them differently many researchers have proposed empirical relationships between the normal stress and friction shear stress over the entire contact length which can be described by a single equation as shown in Eq.11 as proposed by Usui and Shirakashi [28].

$$\tau_{fric} = k[1 - e^{-(\mu\sigma_n/k)}], \quad \text{Eq. 11}$$

Dirikolu et al. further modified Usui and Shirakashi's equation by introducing a friction factor m and exponent n [29] as detailed in Eq.12.

$$\tau_{fric} = mk[1 - e^{-(\mu\sigma_n/k)^n}]^{1/n}, \quad \text{Eq. 12}$$

Constants μ , m , n can be determined by experiments such as photoelastic method, split tool method. Dirikolu experimentally obtained the constants in Eq.12 at different cutting conditions for various materials and the results are summarized in Table 1.

Cutting speed (m/min)	PbLCFCS			LCFCS			MCFCS		
	μ	m	n	μ	m	n	μ	m	n
50	0.75	0.05	1.3	0.80	0.75	2.2	1.5	0.70	1.0
100	0.77	0.52	1.3	0.90	0.78	2.2	1.6	0.68	1.0
150	0.80	0.54	2.2	1.0	0.80	1.7	1.7	0.66	1.0
200	1.05	0.64	1.8	1.3	0.80	1.7	1.6	0.67	1.0
250	1.3	0.74	1.8	1.6	0.80	1.7	1.5	0.66	1.0

Table 1 Friction constants from split-tool test for equation (11) [29]

Many experiments based on split tool method had been conducted. Similar results for the stresses distribution on the rake face of the tool were obtained by different researchers [30-32]. Figure 18 is a typical plot for the normal stress and shear stress distributions on the rake face:

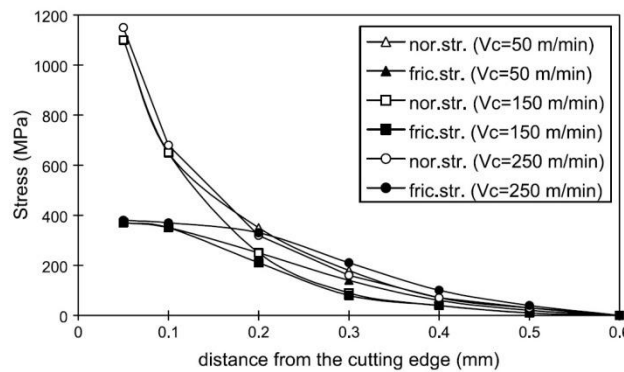


Figure 18 Measured normal and shear stress distribution on cutting tool rake face in orthogonal cutting of LCFCS using the split-tool method [24]

CHAPTER 3 DEVELOPING OF 3D MODELS

In this chapter 2D and 3D thermal coupled metal cutting models will be constructed by both ALE and CEL techniques. Although the goal of this study is to construct 3D metal cutting model, 2D models will be first constructed as a preliminary step to get more knowledge of the modeling techniques before constructing the 3D models. The simulation results will be discussed in later chapter to investigate the feasibility of a 3D ALE metal cutting model and the reliability of CEL technique in modeling cutting process.

Unit system:

This is a thermal coupled problem, so the units of thermal properties have to be dealt carefully. The basics units used for the entire study are listed in Table 2. The other thermal properties are converted into corresponding units base on this fundamental units system.

Table 2 Unit System

Mass	Ton	t
Time	Second	s
Length	Millimetre	mm
Temperature	Celsius	°C
Force	Newton	N
Pressure	Million Pascal	MPa

Materials:

AISI 1045 with hardness of 200~220 BHN was used as the workpiece material throughout this study. The cutting tool used was TNNA 332. Johnson-Cook plasticity model was used to describe the plastic behaviour of the workpiece due to its simplicity and also due to its general acceptance in metal cutting simulations.

The material parameters for the cutting tool and workpiece including those for using Johnson-Cook equation are summarized in Table 3 which were obtained by using split Hopkinson Pressure Bar test [33].

	Workpiece	Tool
Young's Modulus, E [MPa]	205×10^3	560×10^3
Poisson's Ratio, ν	0.3	0.22
Density, ρ [t/mm ³]	7.85×10^{-9}	14.5×10^{-9}
Thermal Expansion, α [°C ⁻¹]	13×10^{-6}	5.4×10^{-6}
Specific Heat, c_p [mm ² s ⁻² °C ⁻¹]	220×10^6	220×10^6
Conductivity, k [t*mm*s ⁻³ °C ⁻¹]	40	40
JC Material Constants:		
A [MPa]	553.1	
B [MPa]	600.8	
n	0.234	
C	0.0134	
m	1.0	
$\dot{\epsilon}_0$ [s ⁻¹]	1.0	

The purpose for constructing these two models is to compare ALE

and CEL formulations, for the sake of simplicity the temperature dependency of thermal expansion, thermal conductivity and specific heat are neglected. Values for those properties are chosen at an elevated temperature of 400 °C.

Friction Model:

Coulomb's friction model or as known as dry sliding model is a simple and robust friction model which was heavily used in early research of metal cutting FE models; it assumes that the ratio of the sliding force and normal force is a constant which is the friction coefficient:

$$\mu = \frac{\tau_{fric}}{\sigma_n} \quad \text{Eq.1}$$

where τ_{fric} is the friction shear at the interface of the workpiece and tool, σ_n is the normal stress on the rake face of the tool and μ is the coefficient of friction (COF).

3.1 2D Models

Model Geometries and Cutting Parameters:

The domain of interest of metal cutting is actually very small. It's

the point where the tool cutting edge contacts the workpiece. The grey rectangular on the left of Figure 19 shows the actual size of the cutting tool insert. Inside the dash-line rectangular is the area of interest and it is enlarged on the right to show the details.

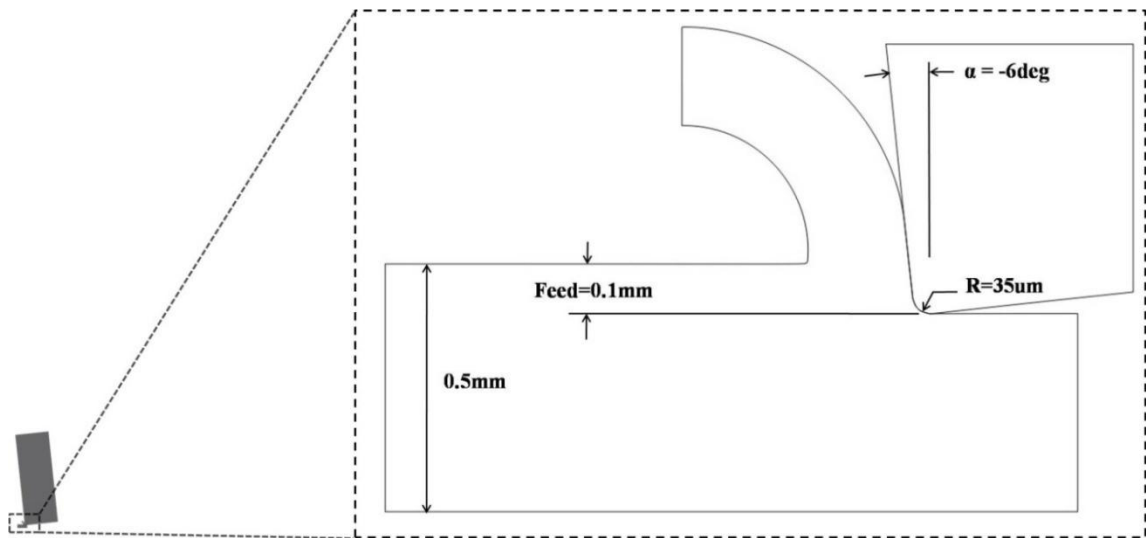


Figure 19 2D cutting configuration

The cutting parameters for the 2D FE models are summarized in

Table 4

Table 4 2D Cutting Model parameters	
Rake Angle, α [deg]	-6
Feed Rate, f [mm rev ⁻¹]	0.1
Cutting Speed, V [m min ⁻¹]	250
Cutting Edge Radius, R_e [mm]	0.035

The overall dimension of the FE model has to be small to reduce the total number of elements required but yet big enough so the boundary conditions applied to the model is reasonable. After couple trials and errors, it was determined for a 2D model the reasonable size for such model is about $1\text{mm} \times 2\text{mm}$ in which high stress areas are included and stresses are low at the model boundaries.

3.1.1 ALE Model

An initial shape of the workpiece that includes the shape of the chip is modeled. However the final chip formed will not be affected by the shape of the initial chip [3, 4], it's just a start point for designing a suitable mesh for the evolved shape of the chip. The entire workpiece is assigned as an adaptive mesh domain and multiple adaptive mesh constraints are applied to the domain for the purpose of maintain the quality of the elements. Keep in mind that the mesh is independent from the material, thus the adaptive mesh constraints applied to the nodes will not actually affect the material flowing underneath the mesh.

Eulerian Surfaces

Due to the steady state nature of the cutting process it's favourable to confine everything inside a control volume. The control volume is enclosed by the Eulerian surfaces and free surfaces of the workpiece material. Three Eulerian surfaces are assigned to the workpiece mesh to realize the inlet and outlets of the control volume as illustrated in Figure 20. The workpiece material is allowed to flow into the mesh from the inlet and flow out of the mesh through the outlet on the right and the outlet at the boundary of the chip as indicated by the arrows. The other surfaces are defined as sliding surfaces where the nodes of the mesh on the surface is independent of the underneath material in the tangential direction but move together with the material in the perpendicular direction of the surface.

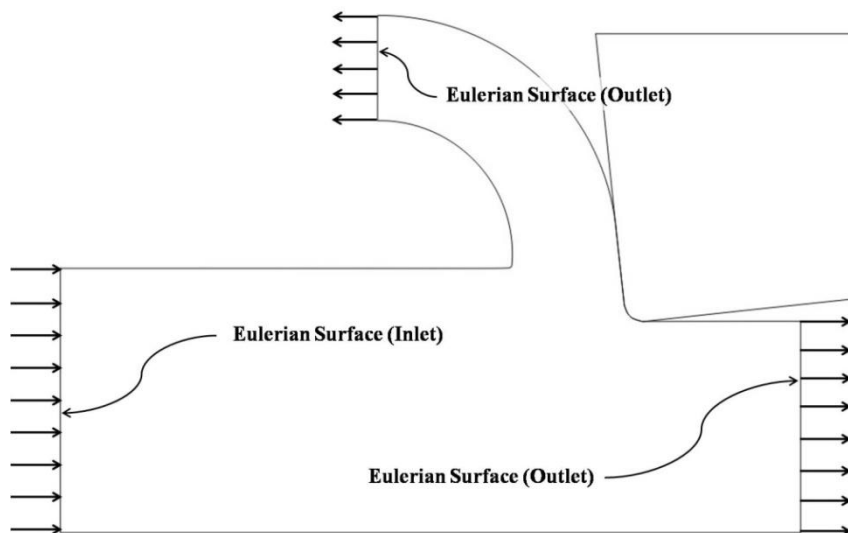


Figure 20 Eulerian surfaces in 2D ALE model

Boundary Conditions(BC)

The boundary conditions for the 2D ALE model are shown in Figure 21. Displacement BC's are applied to the tool and a velocity BC of 4167mm/s in the y-direction is applied to the bottom of the workpiece so that the tool is stationary and the workpiece is moving to the right.

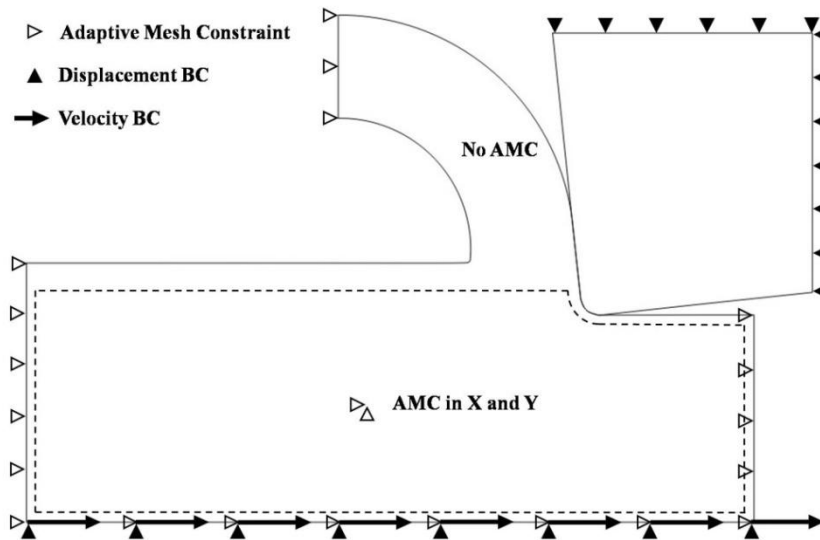


Figure 21 Boundary conditions and adaptive mesh constraints of 2D ALE model

Adaptive Mesh Constraint (AMC)

An Eulerian surface without AMC will act like a sliding surface, that is to say the inlet and outlet effect cannot be realized with Eulerian surface definition alone, the nodes on the Eulerian surface must be constrained in the perpendicular direction of the surface in order to prevent the nodes moving with the material. The implementation of the AMC's is

illustrated in Figure 21, where the AMC's are represented by white filled triangles. The nodes inside the area enclosed by dash lines are constrained in both X and Y directions by an AMC, i.e., all nodes in this area are completely fixed in space to reduce the computational cost on adjusting the position of the nodes and maintaining the quality of the elements. Such an AMC is allowed to be applied due to the fact that the area enclosed by the dash lines is expected to be filled by the material throughout the entire process.

Simulation Results

The simulation result is shown in Figure 22. The velocity boundary condition on the bottom of the workpiece drags material into the left boundary region and pushes material out of the right boundary region. Although there is a presumed initial chip geometry, it will eventually be pushed out of the Eulerian surface at the tip of the chip and thus the presence of the initial chip geometry doesn't affect the result of the simulation. The shape of the initial chip merely serves as a foundation so that the mesh for the final chip can be created and it doesn't affect the final chip shape or the mechanics of cutting [3, 4]. The material keeps deforming and the mesh adjusts itself according to the smooth methods and the AMC's. After the simulation reached steady state in which the shape of the chip, stress/strain/temperature distributions in the

workpiece don't change any more. On the other hand, the heat keeps propagating into the tool thus the temperature distribution inside the tool doesn't reach steady state as fast as the workpiece does. However, since the study at this stage focuses on the workpiece plus the temperature distribution in the tool doesn't really affect the boundary conditions of the workpiece tool interface, we consider the whole model is steady once the workpiece reaches steady state.

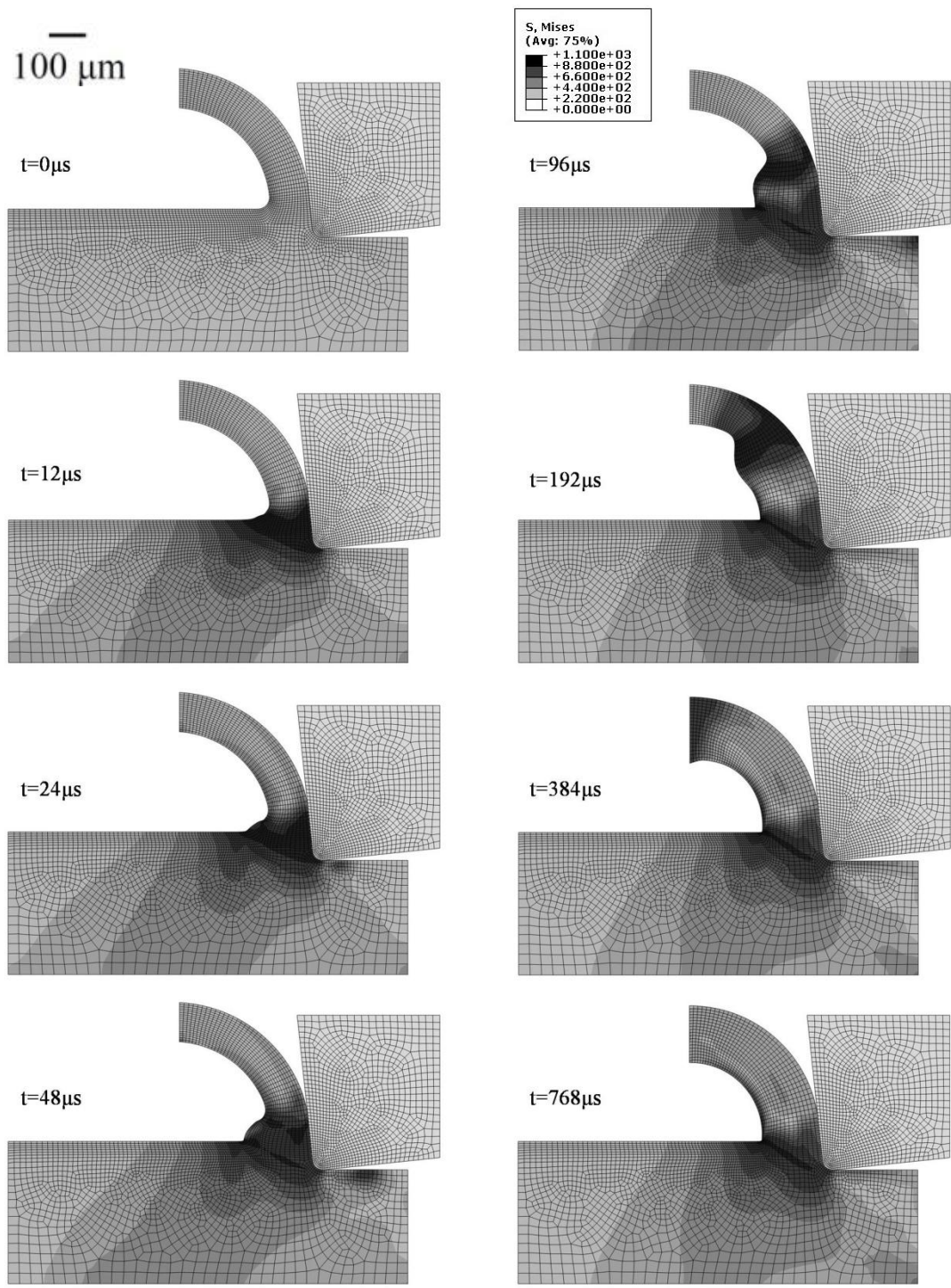


Figure 22 chip formation by ALE formulation at different moment of time (Mises stress contour)

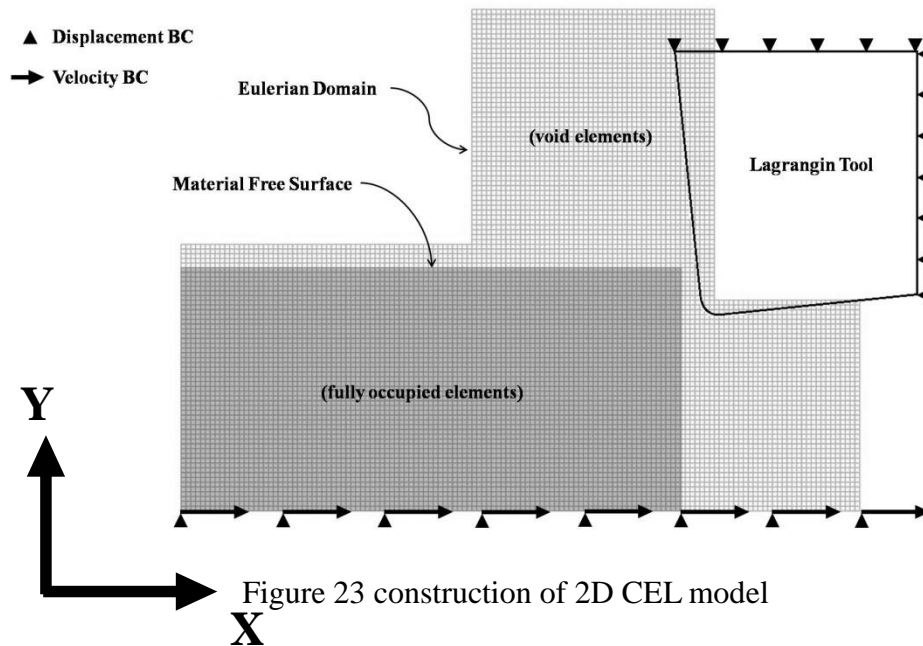
3.1.2 CEL Model

In the CEL model, tool is modeled as a Lagrangian body which is identical to the one in the ALE model. Since a deliberate design for the mesh is not necessary, the workpiece is enclosed by a grid of structural mesh which has enough room for the chip to form and grow as shown in Figure 23. Material exits the domain of the Eulerian mesh grid will be lost from the simulation. The complexity of building a FE model for metal cutting process is dramatically reduced by using CEL formulation when compared to ALE formulation. Neither the initial chip geometry nor a special designed mesh is necessary in a CEL analysis, such a model can be built in 15 minutes by an experienced CAE engineer with the help of CAE software.

Boundary Conditions

Same boundary conditions as in the ALE model are applied to the CEL model, the tool is fixed in space and a velocity boundary condition is applied to the button of the workpiece. It is worth noted that the velocity boundary condition for the workpiece is actually applied on the mesh other than the material inside the Eulerian region. If the material is moving away from the boundary of the Eulerian region as on the left boundary of the

Eulerian region in Figure 23, material will generate automatically and occupies the elements base on the current solutions at the Eulerian region boundary.



Simulation Results

Figure 24 shows the process of chip formation of the 2D CEL model as time elapses. The intact block of workpiece material starts to move to the right as a result of the velocity boundary condition applied on the bottom surface. The workpiece material is free to flow into the void elements until it reaches the cutting Lagrangian cutting tool. The contact algorithm prevents the Eulerian material from occupying the same space as the Lagrangian body occupies and the chip forms naturally. The material keeps entering from the

left boundary of the Eulerian domain, thus the total mass in the control volume increases. Until the time reaches $96\mu\text{s}$, the right side of the free surface of the workpiece material reaches the right boundary of the Eulerian domain, the material is lost from the simulation once it exit the Eulerian domain. The chip keeps growing until the top of the chip reaches the Eulerian domain boundary at time equals to $\sim 384\mu\text{s}$ with a cutting speed of 4166m/s . After this point the mass inside Eulerian domain reaches a constant value and the shape and stress distributions inside the workpiece reaches steady state as well.

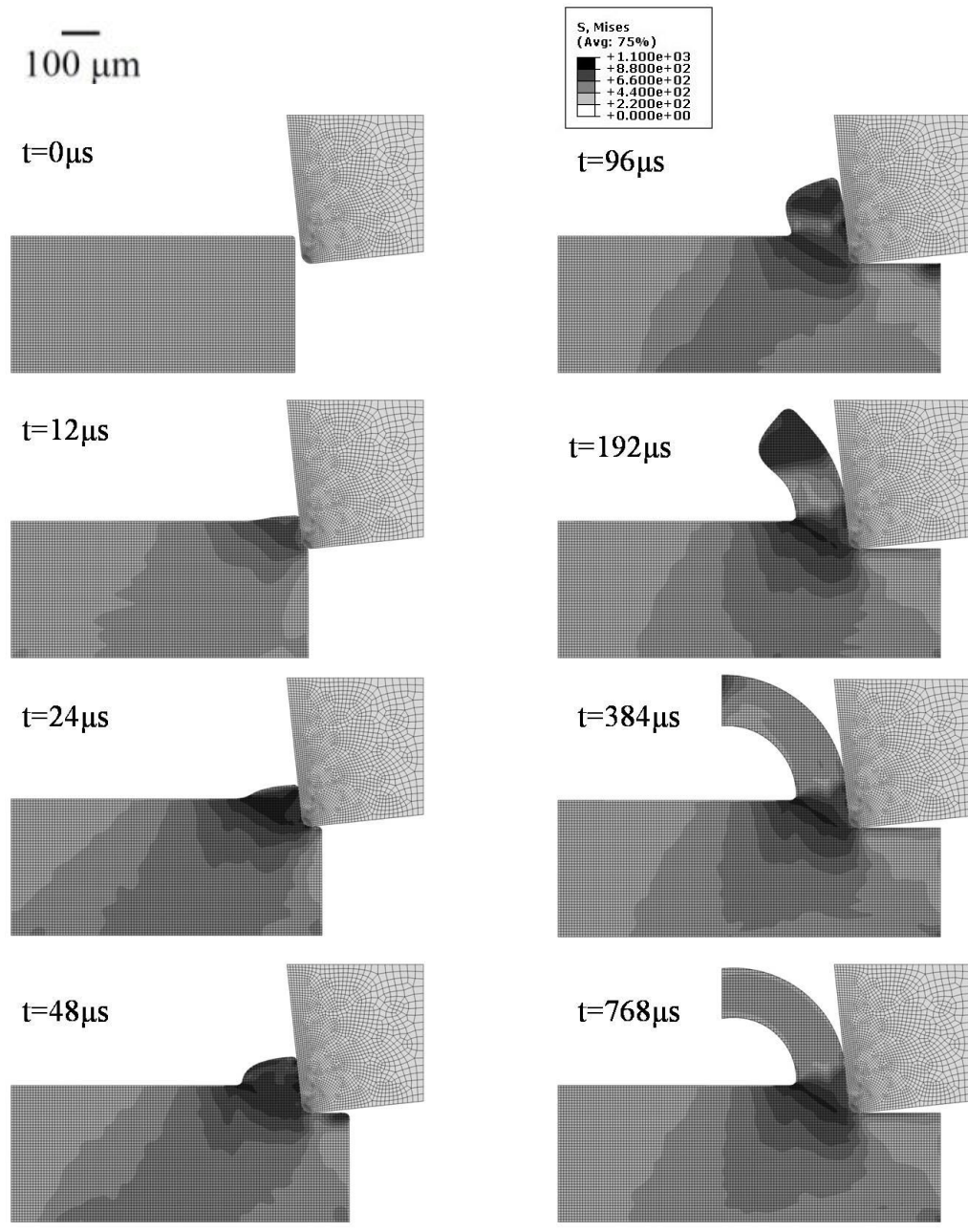


Figure 24 chip formation by CEL formulation at different moment of time (Mises stress contour)

3.1.3 Comparison of Simulation Results

ALE had been proved to have a fairly accurate prediction ability in cutting process, thus ALE model will serve as a reference to benchmark the performance of CEL model. For the purpose of this research the simulations here are not compared to experiment results.

Two models had been constructed by using ALE formulation and CEL formulation. These two models are constructed base on the same orthogonal cutting process, which means they have the same material properties and cutting parameters such as cutting speed, feed rate and rake angle. The only difference between them is the formulation they used. The time span of both the ALE and CEL models can be extended as long as possible which could be a very valuable feature for tool wear simulations.

The results can be distinguished by the topology of the meshes easily. It can be seen that in the ALE model which is shown in (a) (b)

Figure 25(a), the mesh is designed in such a way that the mesh fits the deformed material very well. The adaptive mesh control has successfully prevented the element from severe distortion. On the other hand, in the CEL model on shown in (a) (b)

Figure 25(b), the boundary of the deformed material does not

correspond to an element boundary, the mesh kept its original grid structure even after the material deformed extensively. The boundary of the material is marked by thick line which is computed basing on the material volume fractions in each element. Although the topology of the mesh employed in both models are completely different, the curvature and the thickness of the chips are quite similar.

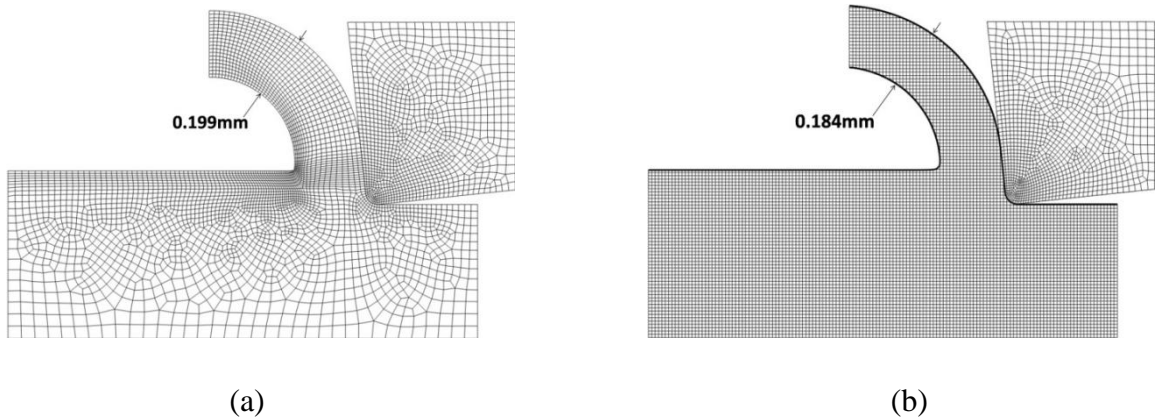


Figure 25 Mesh Topology of (a) ALE and (b) CEL models

The distributions of the Von Mises stress and temperature in the work piece after a cutting time of 1.6ms are plotted in Figure 26 and Figure 27. The overall stress distributions are fairly close. The maximum stress in the ALE model is about 10% higher than that of the CEL model, but important, the contour of the stress distribution are quite similar.

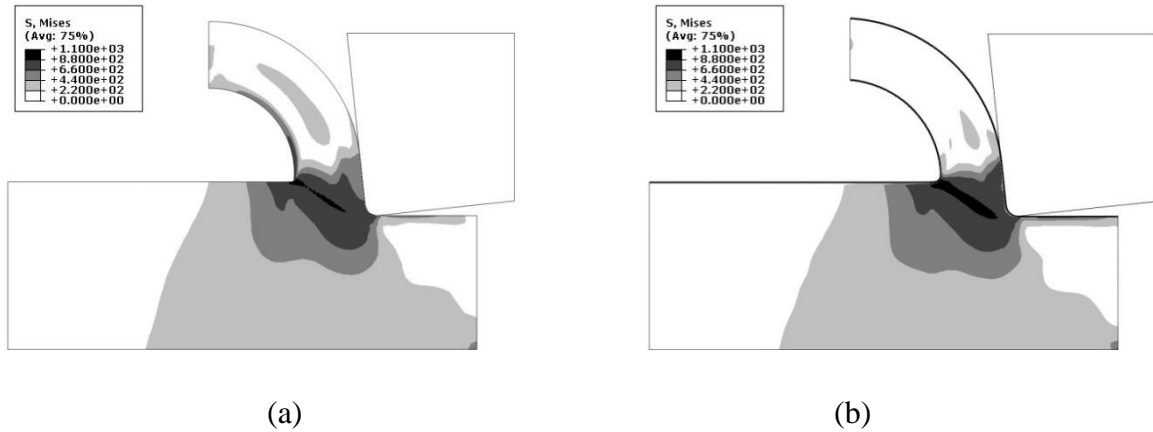


Figure 26 Von Mises stress distribution of (a) ALE and (b) CEL models

Temperature distributions for both cases are plotted with the same manner as stress distribution. There is a relative big difference between the maximum temperatures of the two models which is about 200 °C. The maximum temperature for ALE model is 1000 °C while the CEL model is in the 800 °C range. The contours of the temperature distributions look obviously different above the primary deformation zone inside the chip. With a closer examination, it appears that the difference of the temperature distribution is mainly caused by the high temperature in the secondary shear zone where the new surface of the chip contacts and rubs against the rake face of the tool. Below the secondary shear zone the temperature distributions for both cases are almost the same. Thus it's very likely that the difference of the contact

algorithm of these two formulations caused the discrepancy of the temperature prediction, such discrepancy will be further discussed in Chapter 5.

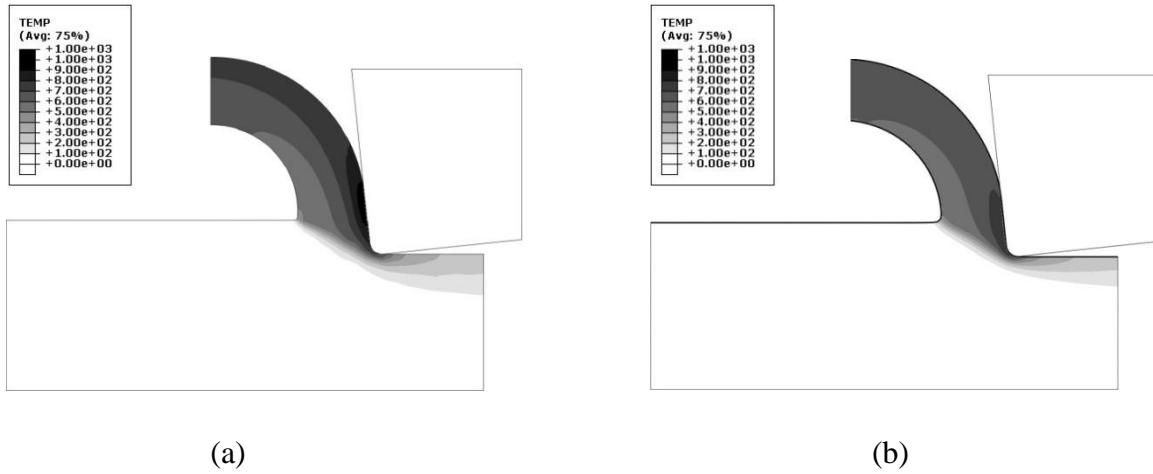


Figure 27 Temperature Distribution of (a) ALE and (b) CEL models

CEL model actually generated very similar results what ALE model did when compared with ALE models as shown in Figure 32, 33, 34 and 35. These plots show how the predicted stress, temperature and vertical speed respectively change along a straight line which is marked as a arrow in Figure 28. The distance is measured from the tool-chip interface.

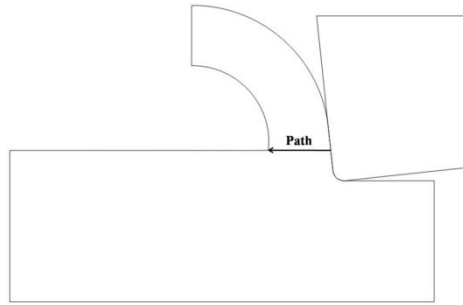


Figure 28 Path along which the data are plotted

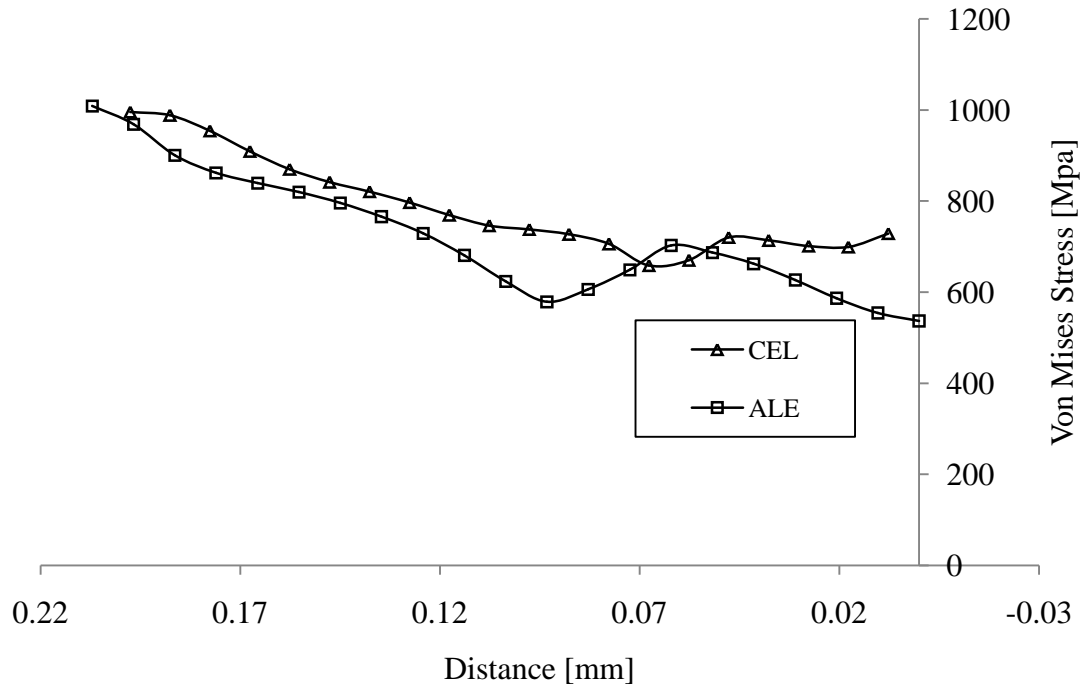


Figure 29 Stresses comparison of ALE and CEL

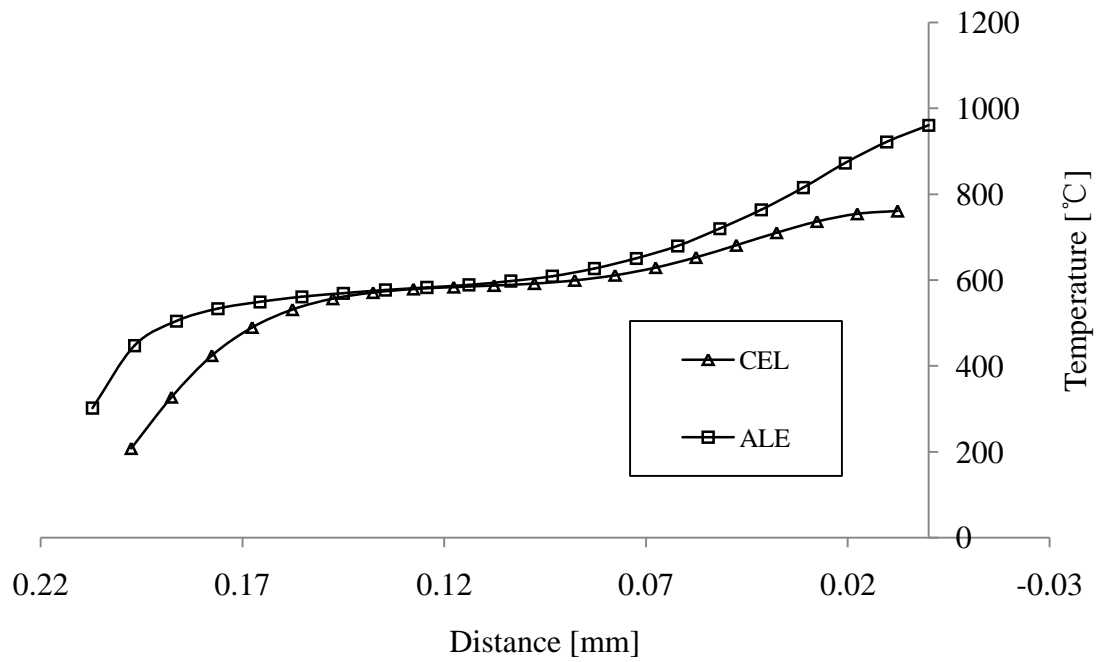


Figure 30 Temperature comparison of ALE and CEL

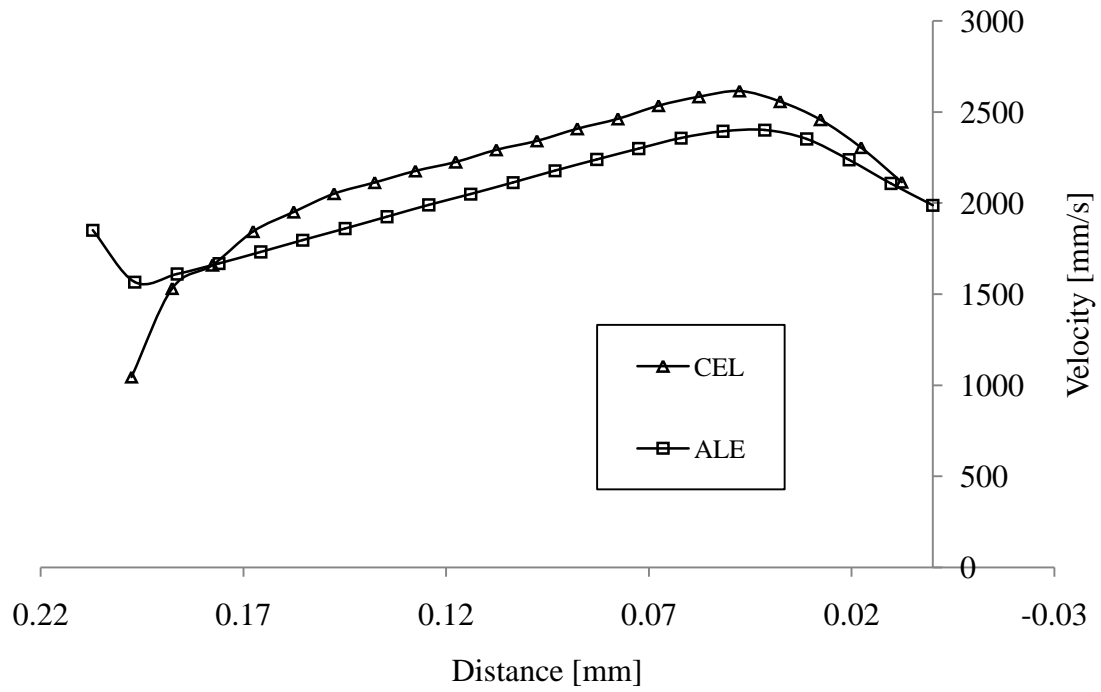


Figure 31 Velocity comparison of ALE and CEL

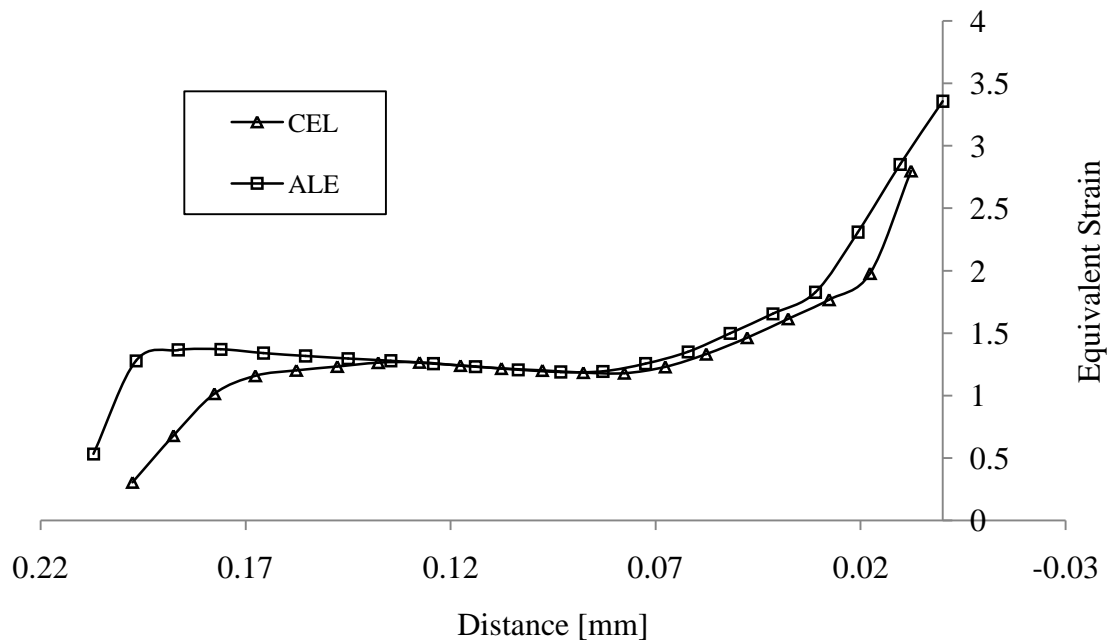


Figure 32 Strains comparison of ALE and CEL

One may have noticed that the curves for CEL model the end points of the curves don't correspond to the free surface of the chip. This is due to the fact that the surface is approximated inside elements and nodes at which the solutions can be extracted don't lie on the approximated free surfaces, thus on the free surface there is no solutions to be plotted.

CEL model has very close results especially in the middle range of the path when compared to ALE model as shown in Figures 29 to 32. However the solutions close to the free surfaces of the chip, i.e. both ends of the path do have some discrepancies. Again the causes of these discrepancies will be discussed later in Chapter 5.

Although there are some obvious difference for the stress and temperature distributions inside the chip, the cutting forces and feeding forces on the other hand are almost exactly the same when compare the two models, as shown in Figure 33. Both models have a cutting force of 175 N/mm and a feeding force of 100 N/mm after steady state is reached. This is because the cutting forces are mainly affected by the solution of the temperature and the stress distribution in the primary shear zone instead of the area above it.

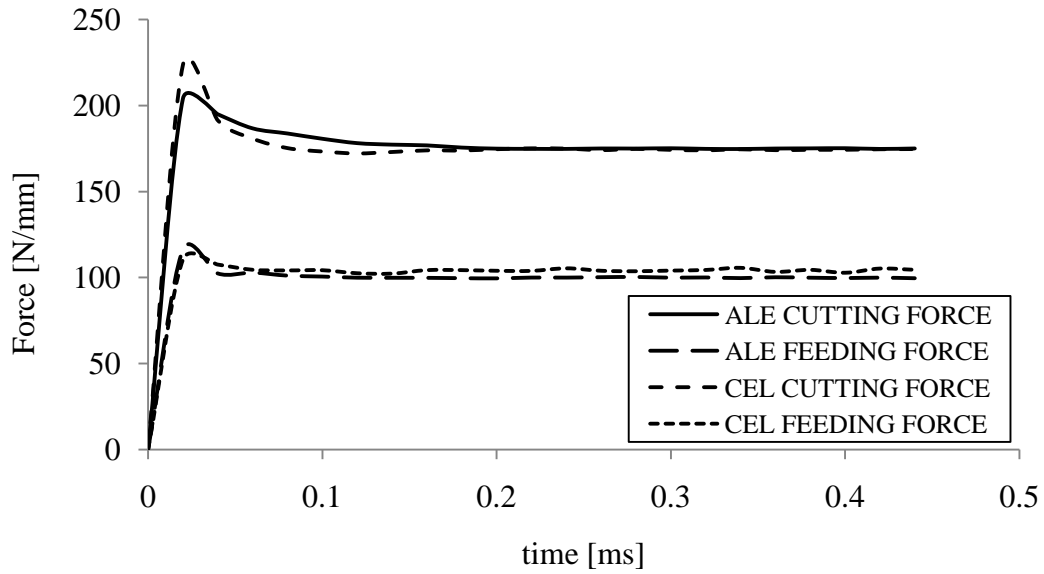


Figure 33 Forces comparison of ALE and CEL

3.2 Semi-3D Models

This semi-3D model is used as an intermediate transition from the 2D model to the full 3D model, because a full 3D model has many modeling technique challenges which will be discussed in the later section. Thus the semi-3D model was first attempted in order to have a better idea of the characteristics and limitations of both modeling techniques in a three dimensional environment before attempting the full 3D model. The semi-3D configuration is shown in Figure 34(a). This cutting configuration is similar to the orthogonal cutting configuration that commonly used in experiments setups for 2D FE modeling validation as shown in Figure 34(b). Except in the

semi-3D configuration the tool nose engages the workpiece instead of the straight cutting edge.

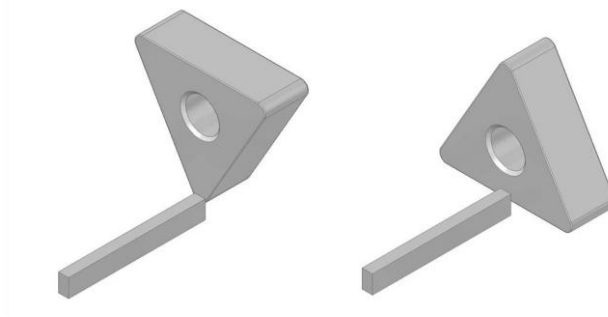


Figure 34 (a) semi-3D cutting configuration, (b) 2D cutting configuration

Geometry and Cutting Conditions

Table 5 Semi-3D Cutting Model Cutting Conditions

Rake Angle, α [deg]	0
Feed Rate, f [mm rev ⁻¹]	0.35*
Cutting Speed, V [m min ⁻¹]	250
Cutting Edge Radius, R_e [mm]	0.075
Nose Radius, R_n [mm]	0.794

*measured at the lowest point of the tool nose

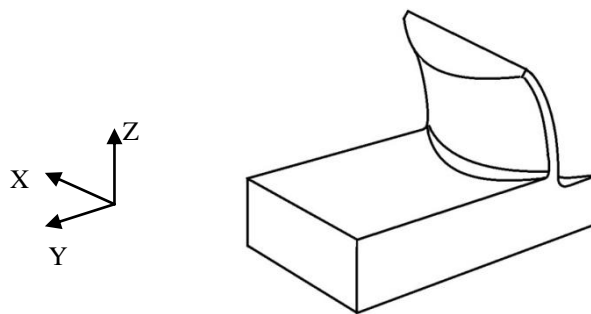


Figure 35 Expected chip geometry from semi-3D cutting

The radius of the nose will induce a dimension variation in the z-direction and thus cannot be simply described by a 2D model, strain will

occurs in the z -direction and the material will flow in the z -direction as well. The chip generated by this configuration will have a uneven thickness as the 2D depth of feed changes due to the curvature of the cutting nose. It's called semi-3D because all the cross sections in the z plane share the same contour without dramatic change. This attribute can be visualized when the workpiece is sliced into pieces by parallel planes of x -plane.

3.2.1 ALE Model

3.2.1.1 Initial Geometry

Similar to 2D ALE model a initial chip is necessary in the workpiece. The initial chip thickness varies by connecting the thickest point to the thinnest point by an arc. There is no specific reason of what dimensions should be used for the initial chip, it's based on the experience of successful 2D ALE models and intuitions. As long as the simulation can complete successfully the solution is not sensitive to the minor changes of the initial chip geometry.

3.2.1.2 3D Elements & Concept of Adaptivity

There are three different shapes for 3D solid (continuum) elements in ABAQUS, tetrahedron, hexahedron (brick) and wedge as shown in Figure 36. All are commonly used in meshing solid bodies.

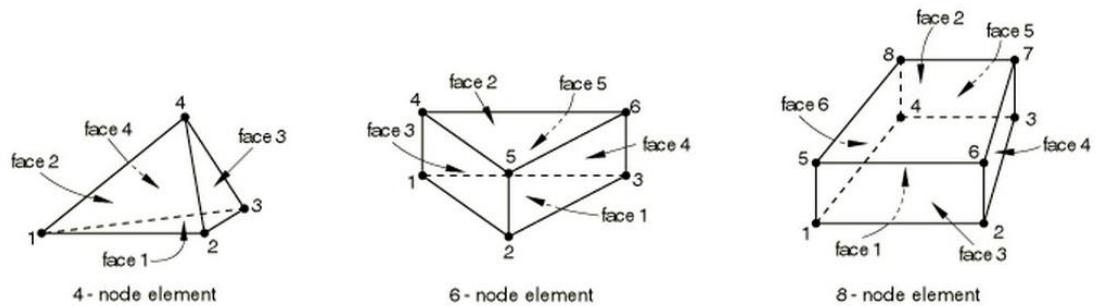


Figure 36 Solid Element Geometries

There is no restrictions to what shapes of continuum elements are used for most of the FE models which employ Lagrangian formulation. There are no restrictions at all to what shapes of the elements are used to mesh the workpiece in the 2D ALE model. The elements can be triangular, quadrilateral or a combination of both. On the other hand, hexahedron elements must be used for 3D ALE model not only because their superior numerical properties but mainly because the geometry of the elements used in a ALE model will directly affect the adaptivity of such model. The level of the adaptivity of a node inside a ALE domain is dependent on the number of the adjacent elements. When this number increases the adaptivity is reduced. Adaptivity of

a node refers to how well the position of a node can be relocated during the Eulerian stage of an increment based on the element smoothing methods such as volume smoothing method which was discussed earlier. The better the adaptivity of the nodes of a model the better the mesh can adjust itself while the workpiece deforms, so less likely to crash during the transition stage. In fact the 2D ALE has no restrictions to the shapes of the elements, this is because the situation in which a node is shared by five or more elements is rarely seen, unless it is intentionally created. On the other hand, if tetrahedral elements are used for an irregular 3D geometry, it's almost impractical to control the number of the adjacent elements with the current FE preprocess softwares. This fact can be demonstrated by the following simple illustration as shown in Figure 37. If a simple cube is meshed, each node is surrounded by 8~10 elements normally if hexahedron elements are used as shown in Figure 37(a). However for tetrahedral elements a node can be easily surrounded by more than 12 elements, as shown in Figure 37 (b), the center node is surrounded by 24 tetrahedral elements. ABAQUS sets a limit of 14 elements as the threshold for determining nonadaptive nodes. Which means whenever a node is shared by more than 14 elements the adaptivity of such node is so poor that it is considered as a nonadaptive node.

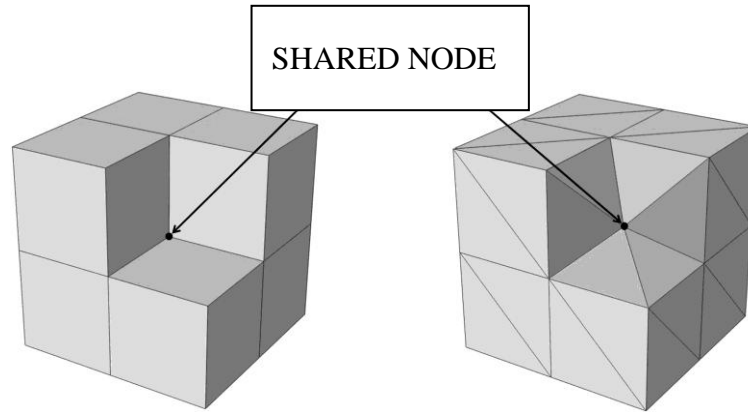


Figure 37 (a) cube meshed by hex. (b) cube meshed by tetra

Nonadaptive nodes will not be relocated during each increment i.e. they are attached to the material and will cause the surrounding elements to distort extensively and eventually crash the model. Thus the presence of the nonadaptive nodes is unacceptable for models which simulate large material flow phenomena such as extrusion and metal cutting. Due to this fact the workpiece has to be meshed by structured hexahedron elements only.

Hexahedron elements are preferred in FE models. This is because smaller number of elements is required to mesh a geometry when compared with tetrahedral elements with the same edge length. As shown in Figure 37(a) for the same cube, only 8 hexahedron elements are required to mesh the solid cube while 24 elements are required if tetrahedral elements are used. The difference in computational cost by using two different elements will be large for a simulation that potentially requires days to be completed.

3.2.1.3 Mesh Design

Although the dimensions vary in the transverse direction the topology doesn't change as illustrated in Figure 38, the same number of lines and arcs segments are present for every cross section and the connection order of these segments are the same as well.

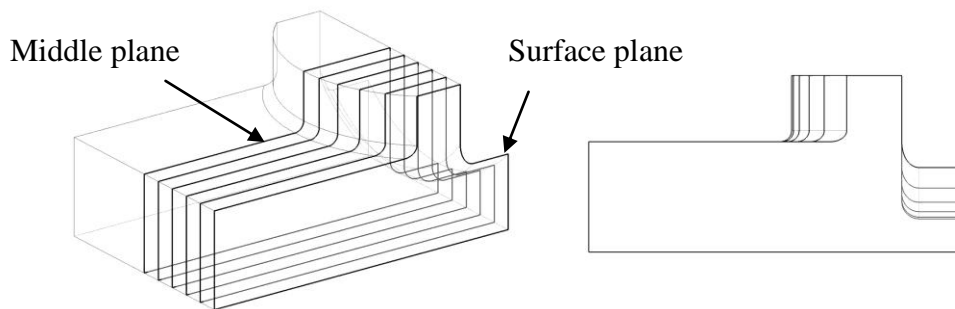


Figure 38 Cross sections of semi-3D workpiece

Therefore the same mesh topology can be swept from the middle plane along the transverse direction and map on to the boundary plane as shown in Figure 39. In fact, this semi-3D configuration was chosen for the purpose of simplifying the mesh design process so that ALE technique can be applied.

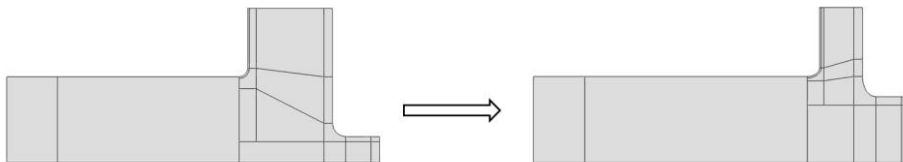


Figure 39 Plane partitions transform from middle plane to surface plane

Due to this configuration's symmetrical property only half of the workpiece is model shown in Figure 40. For the sake of simplicity the tool is model as a rigid surface thus no deflection, heat transfer will occurs for the tool, surfaces which are unlikely to be in contact with the workpiece are excluded from the simulation.

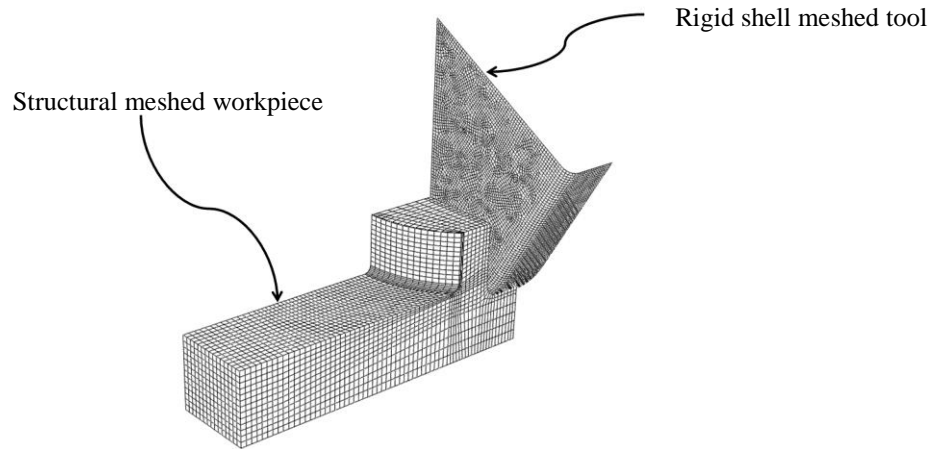


Figure 40 Assembly of semi-3D ALE model

3.2.1.4 BC's & AMC's

The rigid body tool is fixed in space, velocity boundary condition (BC) is applied to the button surface of the workpiece similar to the 2D ALE model. Corresponding BC's are added to the symmetry plane. AMC's are applied to the material inlet and outlets including the outlet of the chip in the directions of the material flow to prevent the nodes on the Eulerian boundaries to move with the material. There is no BC or AMC on the free surfaces thus

the mesh is free to adapt itself to the deforming workpiece.

3.2.1.5 Simulation Results

Results of the stress contour are plotted at different time frame at 0s, 0.05ms, 0.21ms and 1ms from left to right in Figure 41. The result is mirrored to complete the other half of the model for visualization purpose. Same as the 2D model, material flows in and flows out from both the rear of the tool and the top of the chip, thus the chip doesn't seem to grow.

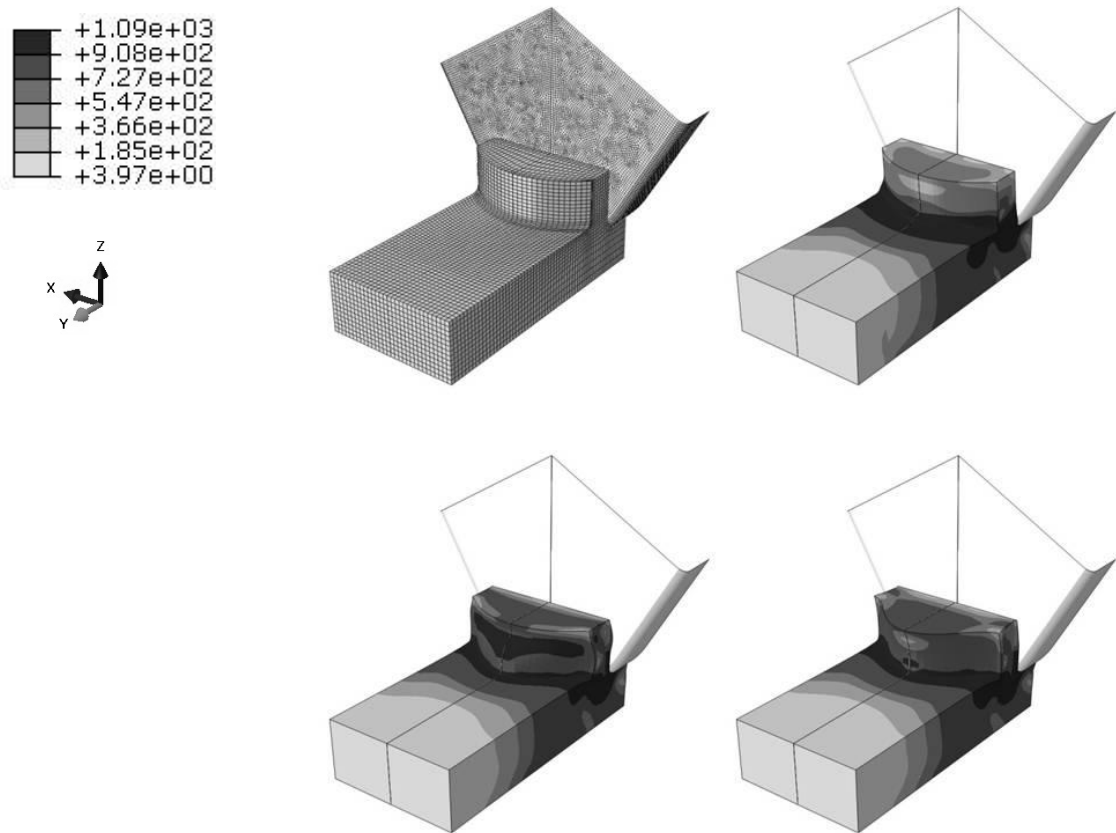


Figure 41 Time lapse from 0s to 0.001s for semi-3D ALE

As expected, after the solution converges the chip is thinner at the edges. The bulging due to the ploughing effect at the workpiece free surface near the cutting edge radius can be observed. This bulging is in the x-direction and is more visible from the top as in Figure 42.

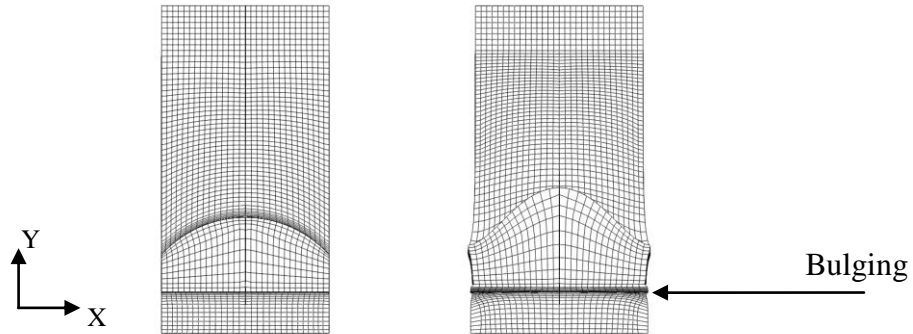


Figure 42 Top view of the workpiece without the tool at 0s and 1ms

Although this bulging is minor it confirmed that ABAQUS's mesh smooth method has the ability to adapt nodes in all three directions simultaneously according to the deforming material. The mesh smooth method can also handles this semi-3D configuration fairly well even without any AMC's for the internal nodes of the workpiece.

3.2.2 CEL Model

Follow the same procedure of 2D CEL model, the semi-3D CEL model is quite straight forward to build. As shown in Figure 43, Similar to the 2D CEL model, a pre-assumed chip geometry is not necessary neither as the

Eulerian elements does not have to conform the workpiece geometry. The Eulerian domain encloses half of the volume with enough space for the chip to grow till chip and tool separation occurs.

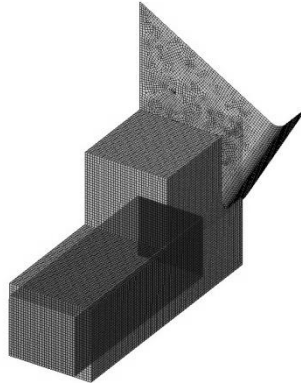


Figure 43 Assembly of semi-3D CEL model

Results of the stress contour are mirrored and plotted at different time step at 0 ms, 0.05 ms, 0.25 ms and 1 ms are shown in Figure 44 with CEL formulation. The tool and workpiece comes into contact as the workpiece moves toward the rigid tool, workpiece material starts to deform at $0.05\mu\text{s}$ and the chip starts to form. Different from the ALE mode, the growth of the chip can be observed from $0\ \mu\text{s}$ to $1\ \mu\text{s}$ until the chip reaches the boundary of the Eulerian region and later the whole model reaches steady state where fields of the material and stress don't change any longer inside the Eulerian region as the time elapses.

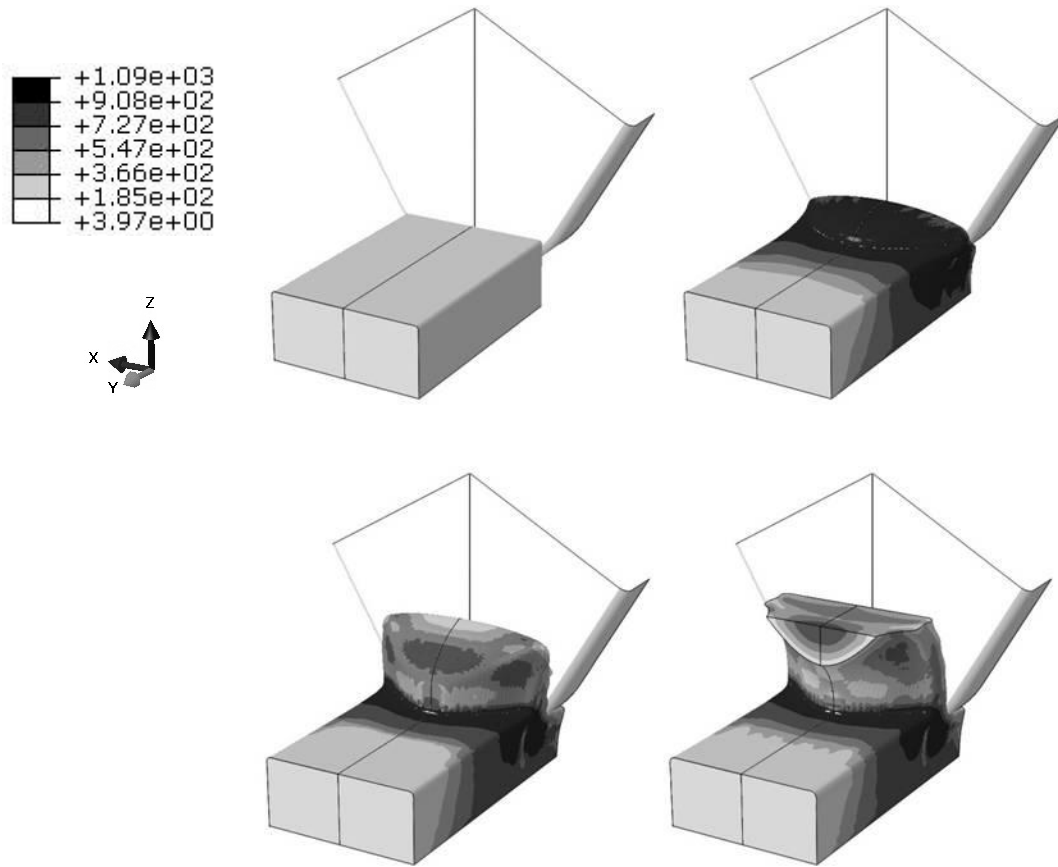


Figure 44 Time lapse from 0s to 0.001s for semi-3D CEL, stress contour

3.2.3 Comparison of Simulation Results

Figure 45 shows the stress distributions of the workpiece for both ALE and CEL models by looking at half of the newly generated face of the chip of the workpiece with cutting tool hidden. The primary shear zone and secondary shear zone are quite distinctive in the ALE model indicated by the highest stress (black) while only the primary shear zone is visible in the CEL

model. This result is quite similar to what was obtained in the 2D models where the primary shear zones of both techniques had the same magnitude of stress around 1GPa but the secondary shear zone is somehow absent in the CEL model.

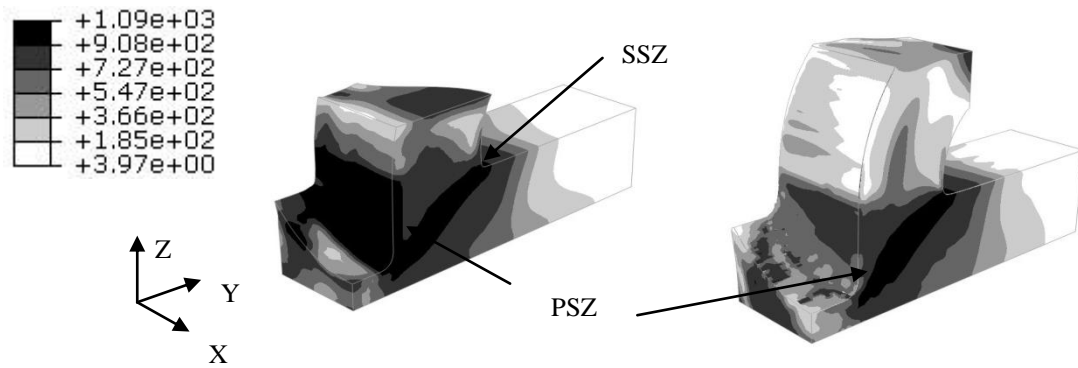


Figure 45 Stress distribution for (a) ALE, (b) CEL semi-3D model

Figure 46 shows the cutting forces and feeding forces for the ALE and CEL model, the difference between the two models during the transaction period from 0s to about 0.03ms is irrelevant as the initial geometries for the two models are different. Discrepancies between the forces are obvious for the two techniques, this was not expected from the results of the 2D models. The ratios between feed and cutting forces for ALE and CEL models are 0.55 and 0.46 respectively.

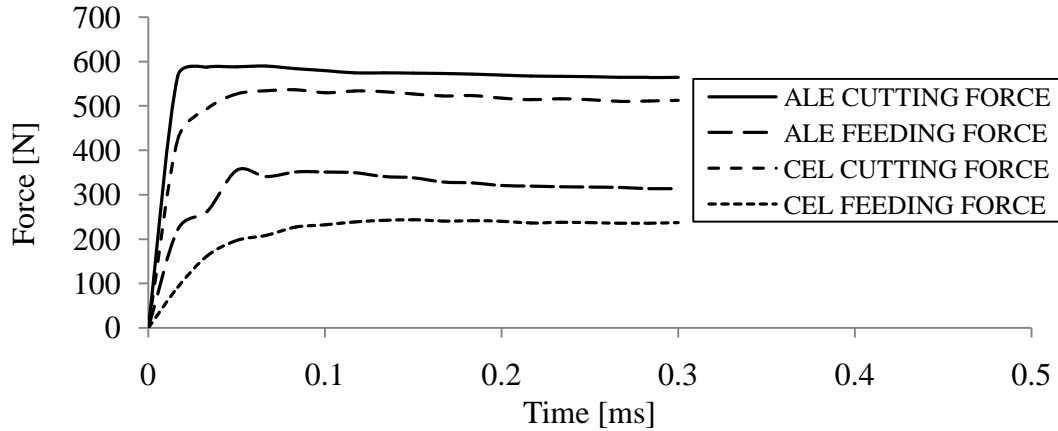


Figure 46 Cutting/Feeding forces vs. time of ALE and CEL model

The ratio between feed and cutting forces in the model can be interpreted as the COF along the tool/workpiece interface as the rake angle is 0. According to the COFs the CEL model ought to have a thinner chip thickness when compared to ALE model [25], and this is confirmed by superimposing the two cross sections of the chips which is illustrated in Figure 47. Same as the difference in temperatures of the 2D models, all these discrepancies of the CEL model and the ALE model including the differences of forces and chip thickness are the consequence of different predicted shear frictions at the tool/workpiece interface. The absence of the secondary shear zone in the CEL model is again another evidence that suggests there is an issue in the CEL contact algorithm when simulating the cutting process. Thus in order to reveal the cause of the problem some basic friction model test simulations have to be conducted before applying CEL formulation to

simulate the cutting process. Such test simulations were conducted and discussed in Chapter 5.

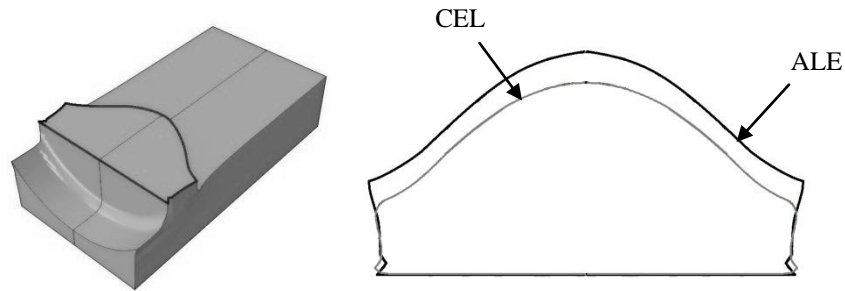


Figure 47 Chip cross sections

3.3 Full-3D Model

Geometry and Cutting Conditions

Instead of cutting with only the straight edge of the tool as in the 2D configuration or with only the nose of the tool as in the semi-3D configuration, a full 3D simulation will have both the edge and nose of the tool engaging the workpiece. This type of turning operation is common seen in industry and as illustrated in Figure 48. For the FE model the cutting parameters are listed in Table 5. These type of configurations which include two cutting areas for major and minor cutting edges as shown in Figure 50 are referred as full-3D cutting configurations, because they can't be described by a planar shape nor a semi-3D that sweeps a planar geometry into 3D geometry as the geometry is

highly nonlinear in all dimensions. Due to this complexity of the tool/workpiece interface geometry the chip formed in such configuration is expected to be fairly complicated as well in all three dimensions.

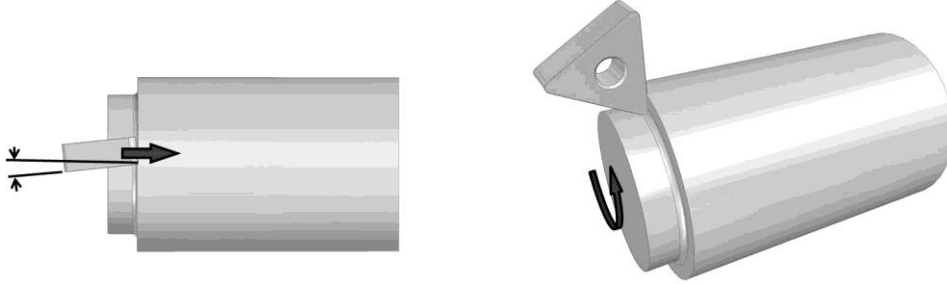


Figure 48 Full 3D configuration, turning with cutting nose

Table 6 3D Cutting Model Cutting Conditions

Rake Angle, α [deg]	-6
Feed Rate, f [mm rev ⁻¹]	0.1
Depth of Cut, h [mm]	3
Cutting Speed, V [m min ⁻¹]	250
Cutting Edge Radius, R_e [mm]	0.075
Nose Radius, R_n [mm]	0.794

3.3.1 Full 3D ALE Model

FE modeling techniques such as Lagrangian and remeshing had been employed extensively for modeling 3D cutting process by different authors as prescribed in Chapter1. The majority of the 3D numerical models are Lagrangian models with failure criteria. For example, Saffar used modeled

drilling operation by Lagrangian formulation with failure criterion and pre-define parting lines [35] while Maurel-Pantel simulated a similar drilling process without pre-define parting lines [18]. Other than the Lagrangian models the rest of the 3D models which can be found in the literature employ remeshing techniques. For example, E. Ceretti who used remeshing technique to simulate oblique cutting processes [15] and S. Buchkremer used remeshing technique to simulate turning process with both straight cutting edge and nose radius [13]. The 3D cutting models which employs ALE technique is hardly found in the open literature.

ALE's obvious advantages in modeling cutting process had been demonstrated in the 2D model as mentioned in the earlier chapter and its reliability is commonly accepted by researchers [3, 4]. ALE formulation is more computational efficient than remeshing technique and more versatile in capturing the contact between the workpiece and the tool when compared with Lagrangian formulation. Although ALE had been used in 2D models extensively, 3D ALE model has not yet been attempted for its inherent modeling challenges. These modeling challenges will be discussed in details later in this section. Therefore the attempt of building a 3D ALE model is very meaningful. A successful ALE 3D model will fill the void of FE cutting model family of different techniques and ought to provide a better chance for

obtaining more reliable 3D results with less of computational time when compared to those models with lagrangian or remeshing techniques.

3.3.1.1 Difficulties In Hex Meshing Irregular Geometry

Most of the objects we see in our daily life are hard to mesh with hex elements. "Automatic meshing of arbitrary objects with high quality, or well shaped, hexahedra remains an open problem. Consequently, industrial practitioners still largely rely on a variety of semi-manual approaches which require considerable user interaction, and can involve days or even weeks to generate meshes of complex shapes[36]." Meshing an random geometry with only hexaderon elements automatically is an ongoing research topic for the areas of finite element preprocessing and computer graphics. Numerous researchers have proposed their methods to address this problem, such as James Gregson who used a method called Volumetric PolyCube Deformation to realize the automation of the hex meshing process [36]. The process starts with converting the initial geometry into a PolyCube geometry which can be partitioned easily and structural meshed with hex elements, then the mesh for the PolyCube geometry can be deformed back to the original geometry as illustrated in Figure 49. Although many researchers asserted that their

methods are robust and reliable, no similar functions can be found in commercial softwares yet [36-38]. Thus practically, no matter it's for industrial production or academic researches manual or semi-manual approaches are the only solutions to generate meshes for complex shapes.

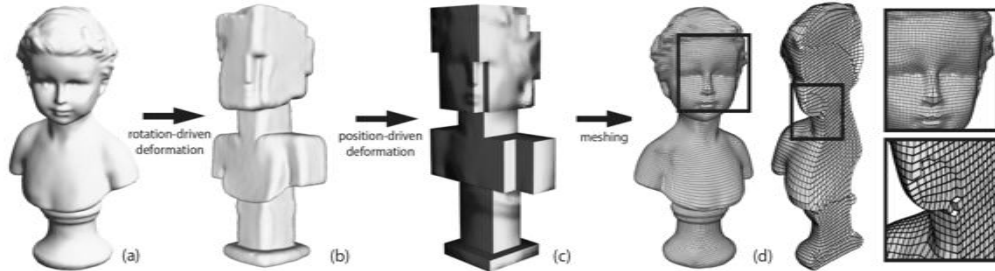


Figure 49 Volumetric Poly Cube Deformation [36]

3.3.1.2 Initial workpiece Geometry and Its meshability

The first step to lay the groundwork for a ALE model is to construct the initial geometry of the workpiece including the initial chip geometry. As illustrated in Figure 50, the engaged cutting edge includes both the straight section of the cutting edge and the arc section of the cutting nose. It will cause the feed to change along the engaged cutting edge as the nominal feed of 0.1 mm within major cutting edge gradually decreases to 0 mm in the minor cutting edge.

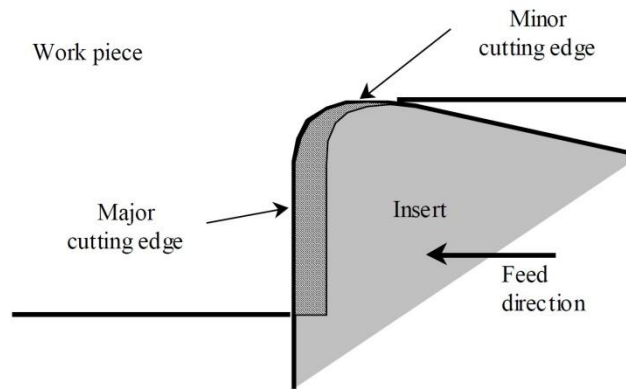


Figure 50 Two cutting areas in Full 3D configuration [39]

The smaller the feed becomes the thinner the chip gets. When the feed approaches 0mm the chip thickness will approach 0 mm, as well and the sharp edge forms. Base on this hypothesis and chip images in Buchkremer's work [13] the initial geometry of the workpiece can be visualized and modeled. Similar to the semi-3D model, the full 3D model has to be meshed by hexaheron elements only due to the same reason which had been discussed earlier in section 3.2.1. However simple face to face sweeping meshing technique is no longer adequate to hex-mesh such an irregular geometry nor a automatic meshing function exists. Thus when modeling the initial workpiece geometry, it has to be close enough to the solution shape so that the initial mesh can conform the solution shape but yet simple enough so that it can be structurally meshed with hexahedron elements. These two objectives contradict with each other on how much detail the geometry should include.

The solution shape of the workpiece in 3D can be fairly complicated with radii at the root of the chip and with sharp edge as illustrated in

Figure 51(a). Too much simplification will cause the simulation to crash due to the poor conformability, on the other hand too many details bring challenges to the meshing process for the workpiece, sometimes it is even impossible to generate the mesh for the workpiece.

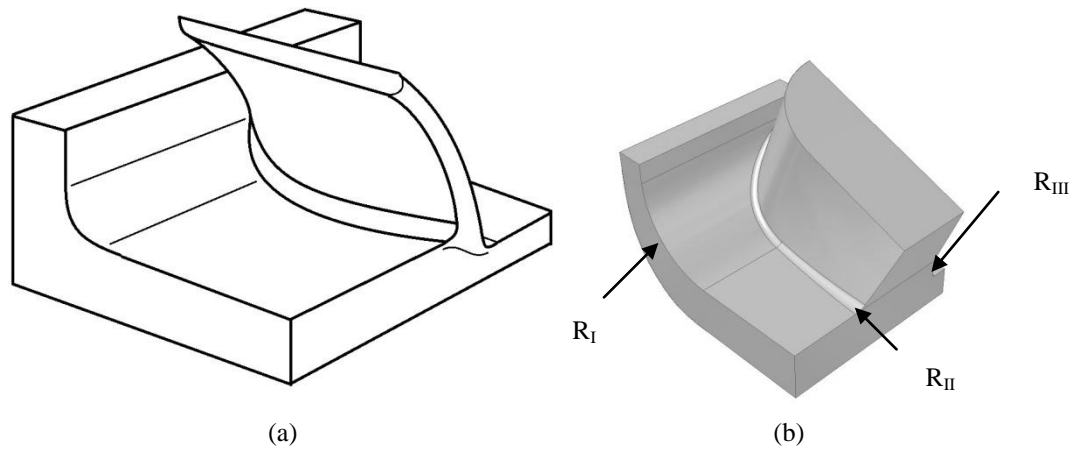


Figure 51 (a) Expected workpiece and chip geometry (b) simplified initial geometry

The initial guess of the workpiece geometry with sharp edges, curved surfaces and radii in different direction is structural-mesh unfriendly, thus it must be simplified further so that it can be partitioned into structurally meshable partitions while still captures all the major features of the solution shape such as the radius that caused by the previous pass of the cutting tool nose radius and radius caused by the tool cutting edge radius.

As shown in

Figure 51(b) three major radii are preserved which include the radius at the cutting edge(R_{III}), the radius at the root of the chip(R_{II}) plus the radius which generated by the previous pass of the cutting tool radius(R_I). Three radii thus exist simultaneously in this geometry model and they meet each other to form an intersection at the corner of the root in front of the nose of the cutting tool as shown in

Figure 53(b). This highly irregular intersection imposes complexity to this geometry as far as its structure meshability is concerned. Another radius is added to the button of the workpiece to reduce the size of the model but more importantly to reduce the difficulty in meshing. Such geometry can be automatically meshed by tetrahedral elements easily in many commercial CAE preprocess softwares such as Abaqus/CAE, Hypermesh and ANSYS workbench. Those meshing functions are highly automatic, global size of the element is the only mandatory input parameter that is required.

Figure 52(a) shows the mesh generated automatically by Abaqus/CAE with tetrahedron elements. It looks alright with the first gaze but a closer look will reveal the nodes which are shared by more than 14 elements. These nodes are nonadaptive and marked by black dots. One of these nodes and its surrounding elements are enlarged in

Figure 52(b), this node is surrounded by 17 elements in total which means its nonadaptive by the definition of ABAQUS. Thus this automatically generated mesh is not usable in an ALE model because the presence of nonadaptive nodes will cause the model to crash eventually. The function to structurally mesh an arbitrary geometry is not yet available in any commercial softwares, thus manually meshing the workpiece is inevitable.

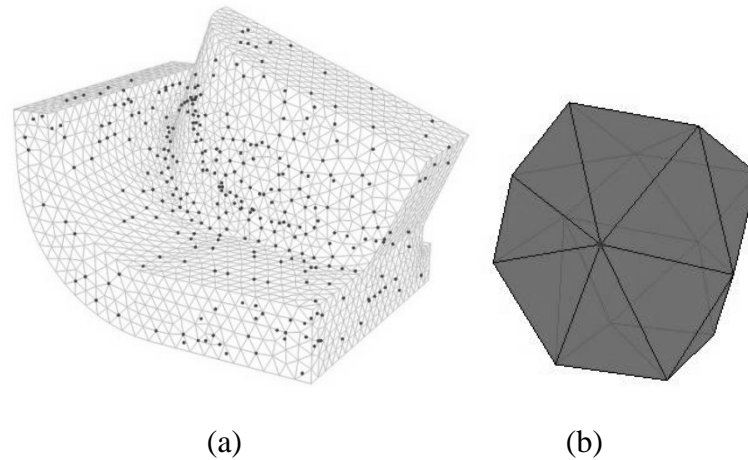


Figure 52(a) Mesh generated automatically by ABAQUS/CAE (b) Enlarged elements

After considerable amount of efforts and thoughts the initial workpiece geometry as shown in

Figure 53(a) was carefully divided into more than 40 partitions as shown in

Figure 53(b). The solution for partitioning for such geometry is almost unique.

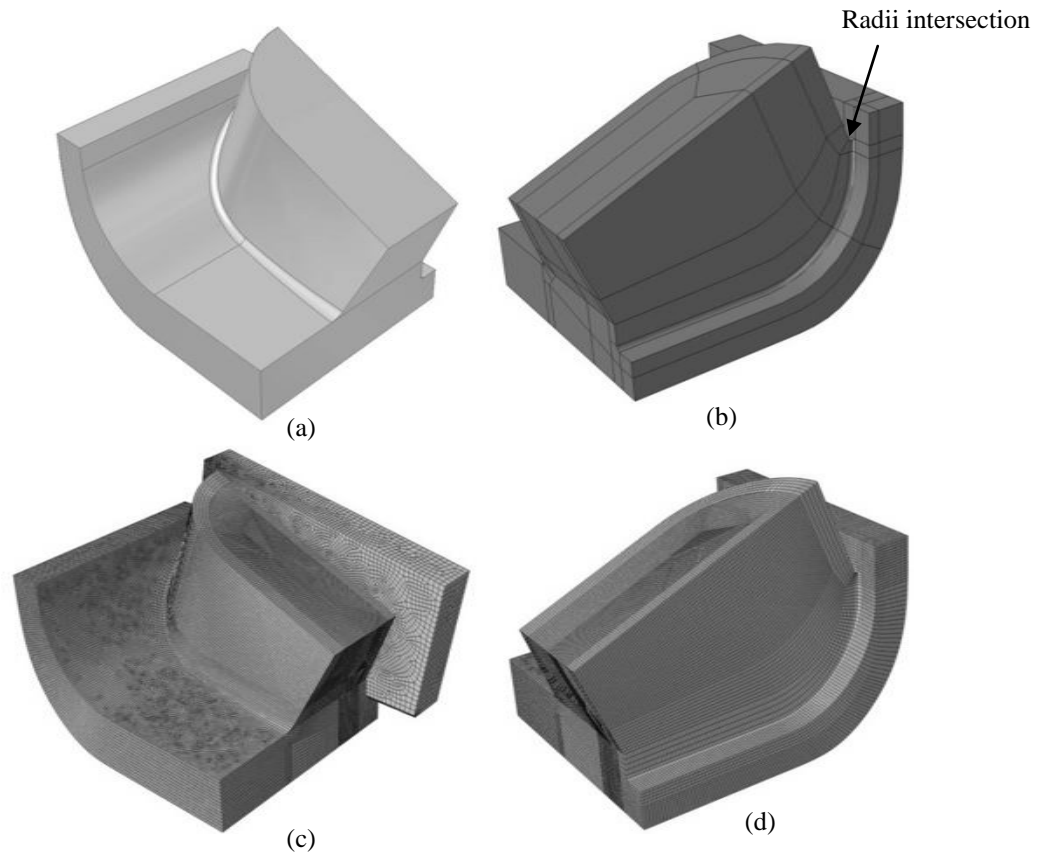


Figure 53 (a) Workpiece initial geometry (b) a geometry partitioned into cells (c) meshed workpiece front view with tool (d) meshed workpiece rear view without tool

After number of simulation attempts the mesh design in

Figure 53(c) was determined as not suitable for simulating the cutting process. One of the problems is that the initial chip thickness is too thick compared to the solution chip thickness, thus the initial mesh has difficulties to conform the solution geometry and crashing of the simulation is inevitable. Trial and error had to be carried out in order to determine the right dimensions of the initial geometry and the right topology of the initial mesh for the

workpiece. The complexity of generating a mesh of the geometry as in

Figure 53 is obvious. With such a complicated initial geometry, the trial and error process would be very time consuming. Therefore the initial geometry has to be further simplified in order to speed up the trial and error process so that a suitable initial mesh of the workpiece can be discovered for a particular cutting configuration.

3.3.1.3 Alternative Approach for 3D ALE Mesh Design

In traditional 2D ALE model, the radii are modeled prior to the simulation. The initial workpiece geometry is designed to be very close to the solution geometry thus the transition from the initial shape to the evolved shape happens smoothly. However these radii will increase the complexity of meshing dramatically in a 3D model. Thus eliminating the radii of the initial geometry is necessary but the dilemma is that a initial geometry without radii is very different from the solution geometry and thus it will impose challenges to the current ABAQUS mesh smooth method in adapting the initial mesh to the evolving workpiece geometry.

The key idea is to fully explore the mesh adaptivity ability of ALE formulation in ABAQUS. If the mesh smooth method is robust enough in 3D then a simple starting point of the initial geometry is adequate for the

simulation proceed.

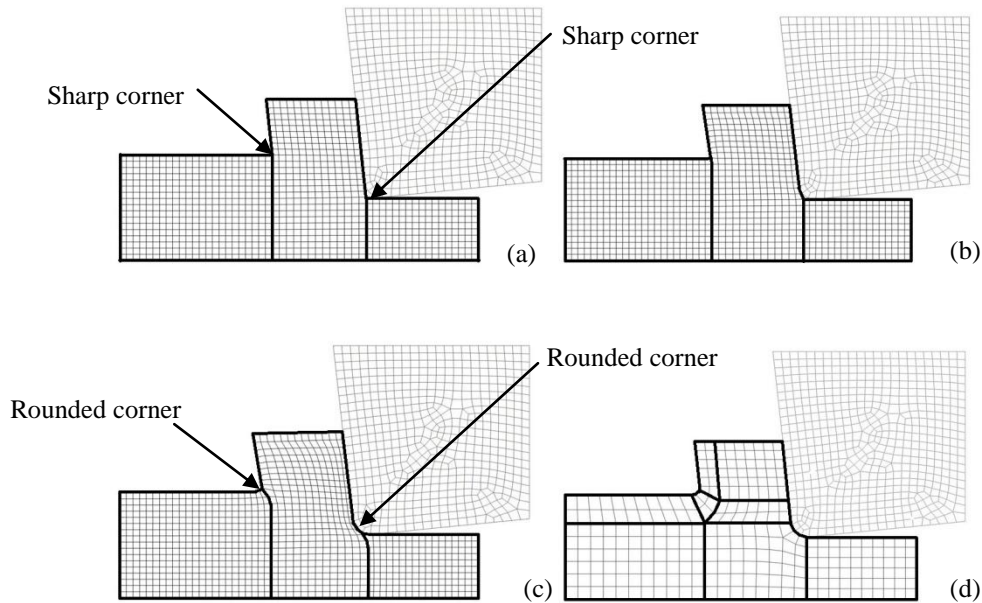


Figure 54 (a) Simplified ALE mesh before deformation (b) Simplified ALE mesh during deformation (c) Simplified ALE mesh after deformation (d) Special designed ALE mesh

To illustrate this idea we can consider the following example. In the 2D ALE model, instead of having the geometry and mesh design which includes the radii, a simpler form of initial geometry as shown in Figure 54(a) can be employed. In the simplified geometry design the radii are eliminated, so that the workpiece can be partitioned into three simple rectangular regions. The topology of such mesh is much simpler when compared with the original mesh topology as in Figure 54(d) which has 8 partitions due to the present of the radii. The sharp corners in the initial workpiece geometry are certainly not

realistic, but it is just a starting point. With the simplified workpiece geometry the simulation now needs one more engaging step before the simulation can actually proceed. During the first step, i.e the engaging step, the tool will engage the workpiece as shown in Figure 54(b) and force the workpiece to take the shape of the cutting edge radius, the sharp corner on the top surface of the workpiece will grow into a radius as well after the workpiece deforms which is demonstrated in Figure 54(c). After the engaging process the simplified mesh now has the same contour/solution as the detailed geometry mesh in Figure 54(d), which means the simple mesh workpiece is now ready to proceed to the second step in the same manner as the detail workpiece although they have different mesh topologies.

This 2D example demonstrate how simple the initial geometry can be in a 2D ALE cutting model if details such as the radii are eliminated. The same idea can be extended and applied to the 3D ALE model by removing the radii and consider the initial chip thickness as constant. The question now is whether the mesh smooth method can effectively handle the transition between the initial mesh and the deformed mesh in 3D.

By applying the same idea to the 3D model, the initial geometry can now be simplified as Figure 55 from

Figure 53(a).

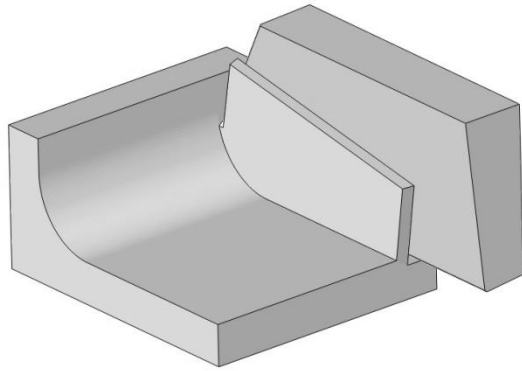


Figure 55 New design of the initial geometry

The simplification is obvious, the geometry is much easier to be partitioned, in fact only 20 partitions are needed to make the entire geometry structurally meshable. Some of the extra partitions are needed in this model to have a more detail control of the AMC's inside the workpiece as showed in

Figure 56(a). As illustrated in

Figure 56(b) the pre-machined surface and the newly machined surface are at different height, however they are also in the same plane and contacted to each other by the co-plane surface. The height difference causes the inconsistency of the geometry in the y-direction, while the change from different height to the same height for the pre-machined and the newly-machined surfaces causes the inconsistency of the geometry in the x-direction. Thus a partition surface that resolves this inconsistency is constructed inside the root of the chip, it is labeled as transition surface and enclosed by thicken black line, as shown in

Figure 56(c), which the cells of the initial chip are hidden.

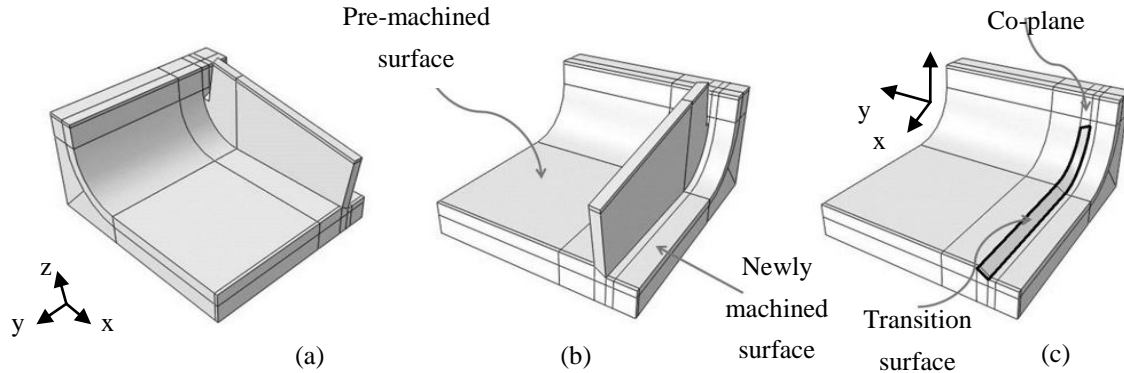


Figure 56 (a) New initial workpiece geometry design and its partitions, (b) Pre-machined surface & newly machined surface, (c) Transition surface & co-plane surface

With this transition surface, the pre-machined surface, newly machined surface and the co-plane surfaces can now be united into one continuous surface from a mesh topology point of view. With the transition partition surface the initial geometry can now be meshed structurally as showed in Figure 57. Portion of the elements are hidden to reveal the internal structural mesh of the workpiece.

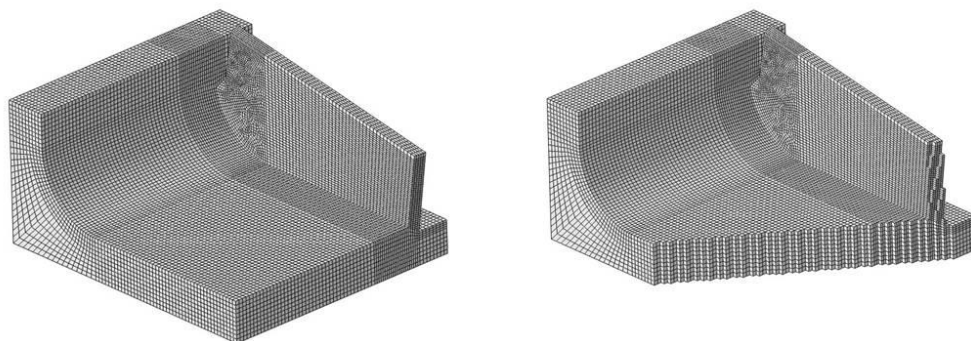


Figure 57 Structural meshed initial geometry

Similar to the 2D example as shown in Figure 54, during the first step, with the simplified mesh design the workpiece will be first set as stationary, the tool approaches and engages the workpiece and "shapes" the cutting edge area of the workpiece into expected shape. After the workpiece takes the form of the tool, the simulation proceeds to step-2 where the tool now is stationary and workpiece begins to move against the tool as the material flows into and out of the Eulerian surfaces. Ideally the shape of the chip will evolve and the mesh smooth method will keep tracking on the material boundary and redistribute the nodes nicely on the surface and also the nodes inside the body of the workpiece during every predefined number of increments. Thus no elements will be highly distorted and a 3D ALE cutting model can be realized.

3.3.1.4 Model Assembly and BC's & AMC's

Except the mesh design for the workpiece, the model assembly and BC's are similar to those of the semi-3D ALE model. Some extra AMC's (adaptive mesh constraints) are required to limit the unfavourable mesh motion. Unfavourable mesh motion is generally the result of uneven element density distribution in the initial geometry and the deactivation of the geometry edge detection function. Issues regarding special treatments of the full-3D ALE model will be further discussed in the discussion session. Figure

58 shows the general BC's and AMC's of the model assembly.

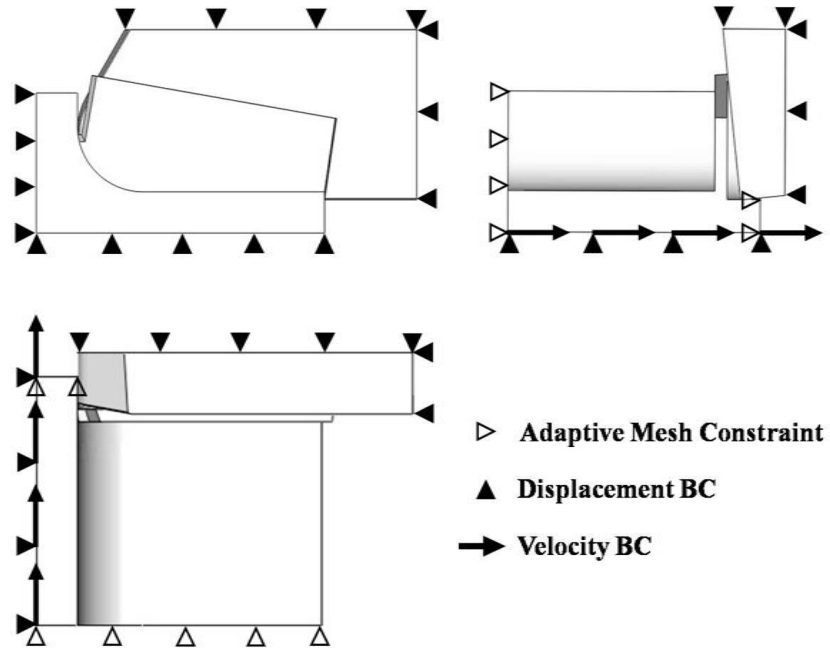


Figure 58 BC's & AMC's of full-3D ALE model, front/right/top views

Velocity BC's are applied to the button and the back planes so that the material will be dragged into the front Eulerian surface and pushed out of the rear Eulerian surface. AMC's (empty triangles) are applied to the front and the rear faces to ensure the independency of the elements from the flowing material so that the Eulerian surfaces can be realized.

3.3.1.5 Simulation Results

The simulation was able to run and useful results of the 3D ALE model was obtained after steady state is reached. The computational time for a cut of 1.5mm is about 12 hours with a single CPU at a speed of 3.7 GHz. Simulation stress results at different time frames are displayed in Figure 59.

Due to complexity of the chip geometry Eulerian surface and AMC are not applied to the top of the chip, thus the growth of the chip can be observed but the time span the simulation is able to run is limited as the elements in the chip will eventually crash when being stretched too much.

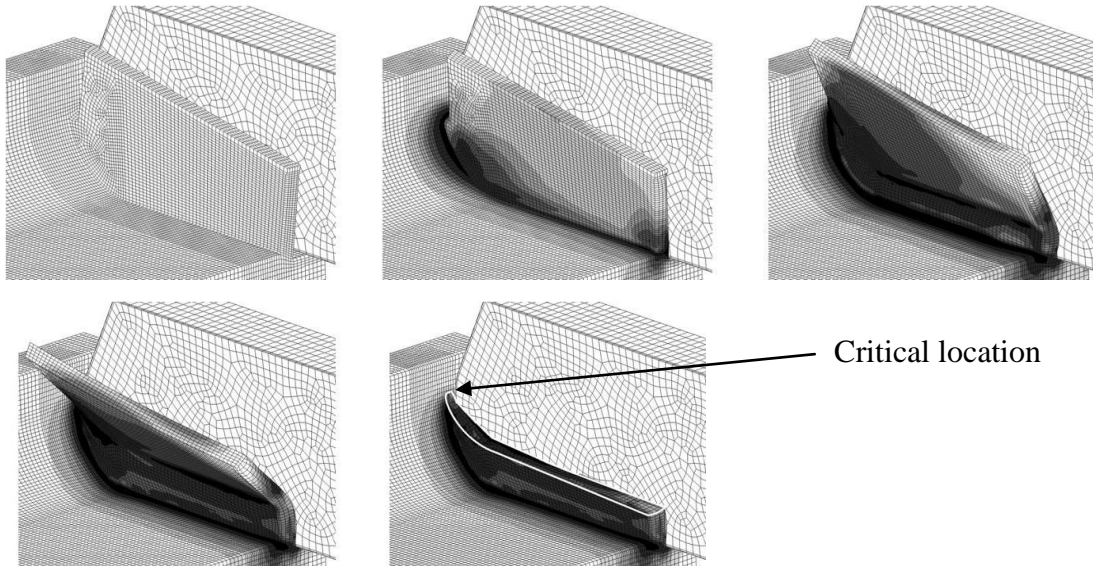


Figure 59 3D ALE model at different times with portion of the chip hidden

3.3.1.6 Termination of the Simulation

In this particular case the simulation was terminated eventually due to the distortion of the element at the chip where the tool nose exit the workpiece (critical location) as showed in Figure 59. In fact, most simulation attempts crashed earlier before useful data can be extract. Only a few of then can last long enough to reach steady state. The direct cause of the terminations of the simulations is the mesh smooth method failed to effectively adapt the mesh at the very unstable (unstable of the solutions)

critical location. Generally, there are three factors which are 1) initial geometry, 2) initial mesh and 3) mesh smooth method that determine the chance of successful completion of a 3D ALE cutting simulation. The relationship between this factors can be demonstrated in Figure 60.

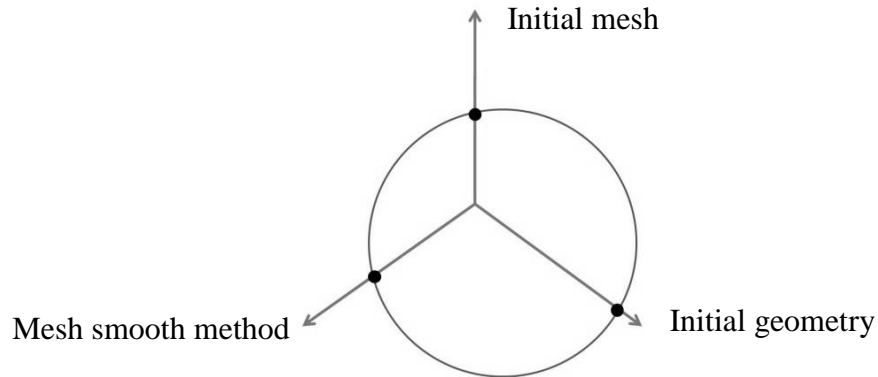


Figure 60 Three critical factors of 3D ALE model

Firstly, the initial geometry axis represent how close the initial geometry is to the solution geometry, the closer the better. Secondly, the initial mesh axis measures how evenly the elements are distributed. Finally, the mesh smooth method axis measures how well the the nodes can be relocated by the mesh smooth method. The area of a circle that intersect all three points represent the chance that a model can be completed successfully. If one of these three factors is superior then the requirements for the other two are less strict. For example, for the same area of the circle, if the initial geometry is really close to the final solution geometry then the initial mesh

and the mesh smooth method can play a less important role accordingly in determining the chance of successful completion of the model and vice versa.

3.3.2 Full 3D CEL Model

The easiness of using CEL formulation has been demonstrated in the 2D and semi-3D models. It doesn't make much difference in the modeling procedures when both the nose and the straight cutting edge of the cutting tool are included in the metal cutting process. Once the inlet geometry and the B.C's are define the model is ready to run. In fact this CEL model was used as an reference to build the initial geometry of the workpiece in the full 3D ALE model because it is unecessary to assume any inital geometry of the chip. Different than the semi-3D CEL model, in this full-3D CEL model the tool will be model as a deformable solid and heat conduction between the tool and the workpiece will also be included.

The thermal conductance of the interface between the tool and the workpiece as a function of clearance is not supported in ABAQUS. Thus instead of assigning the thermal conductance as a function of gap distance it is assumed to be a function of contact pressure. Due to the lack of reference for such a thermal contact property, a very high conductivity is used which means

there is no heat resistance once the workpiece and tool are in contact. The data used for the thermal conductance for both ALE and CEL are summarized in Table 7.

ALE		CEL	
Conductance	Gap distance	conductance	Gap pressure
[t*mm*s ⁻³ °C ⁻¹]	[mm]	[t*mm*s ⁻³ °C ⁻¹]	[MPa]
500000	0	0	0.01
0	0.01	500000	1

Table 7 Gap conductance data

As illustrated in

(a) (b)

Figure 61 three part instances, the reference workpiece, Eulerian region and Lagrangian tool are included in the assembly.

Eulerian domain

Radius from previous pass

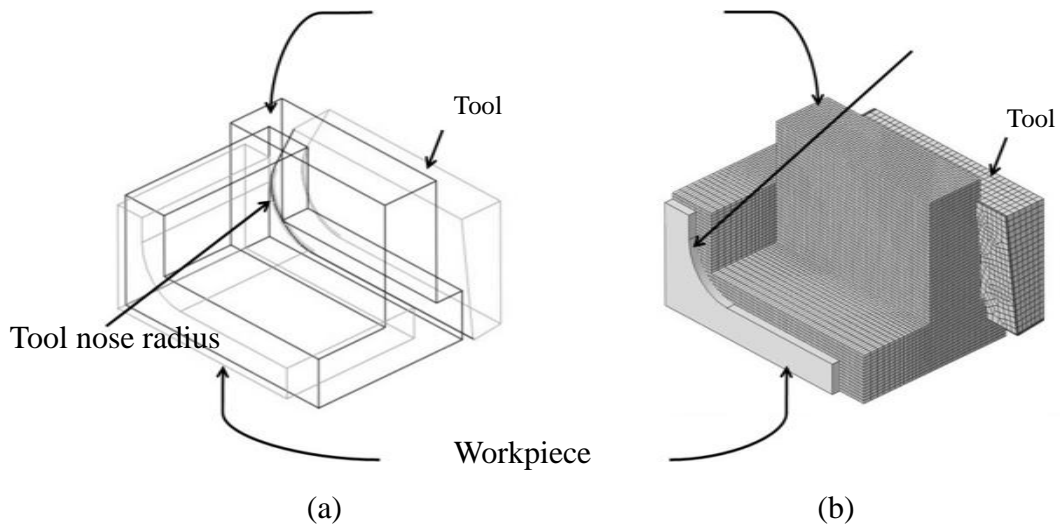


Figure 61 Full 3D ALE assembly (a) wireframe view and (b) mesh view

As shown in

Figure 62 the velocity BC's are applied to the bottom and back planes of the Eulerian region which are initially all zero in the step-1 and then velocity in z-direction is modified to be -4166mm in step-2. On the other hand, the tool is moving in z-direction with a speed of 4166 in step-1 and then fixed in space in step-2.

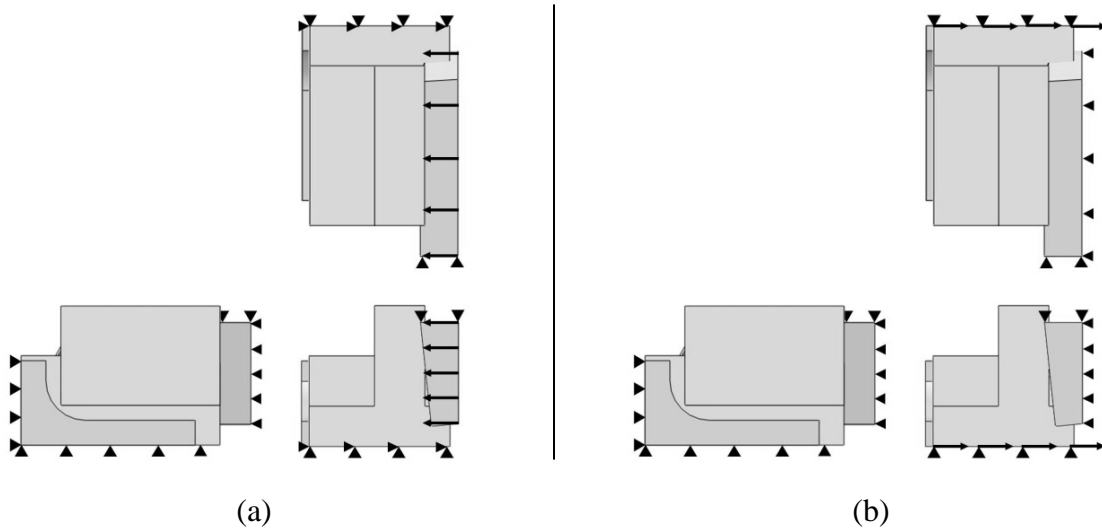


Figure 62 BC's for full-3D ALE model in step-1(a) and step-2(b), front/left/top views

3.3.2.1 Simulation Results:

The simulation was successfully completed for the time span of 0.55ms or cut length of 2.2mm. The maximum stress in the workpiece is comparable to that of the 2D models which is above 1GPa. Figure 62 shows the time-lapse of the full 3D CEL model that starts with an intact workpiece. Chip forms naturally and curve helically which is very close to the shape of the chips from physical experiments from Buchkremer's experiments [13]. The contour of the chip is highlighted with white line in the last frame to highlight the complex curves in the chip that formed from this full 3D cutting configuration.

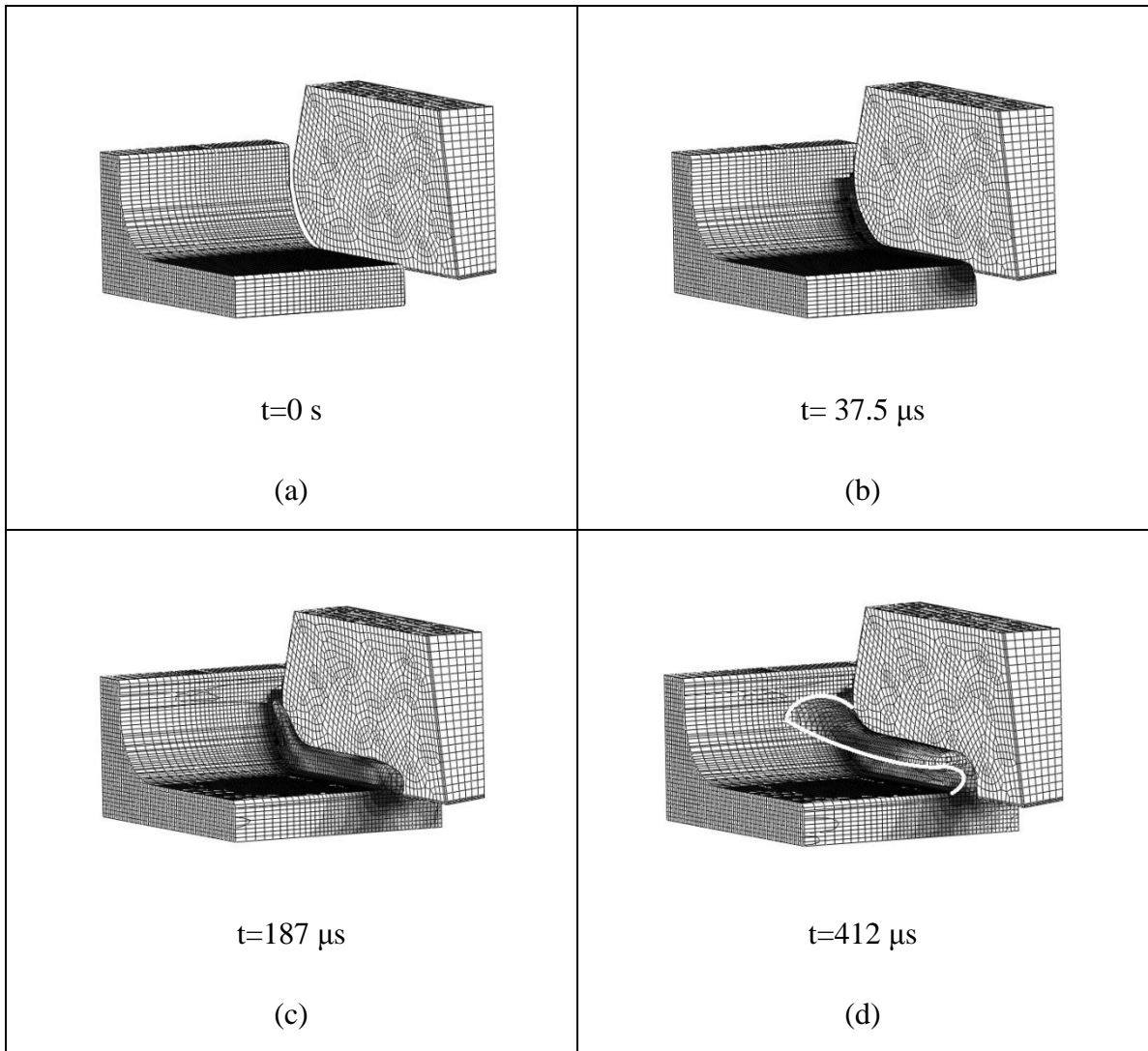


Figure 62 Simulation result of full-3D CEL model at time frame of a) 0s, b) 37.5us, c) 187us and d) 412us

Figure 63 shows the shape of the chip from different angles at the time frame of 525us. The tool is hidden and only showed in the left view to better exhibit the shape of the chip and the stress distribution underneath the cutting tool.

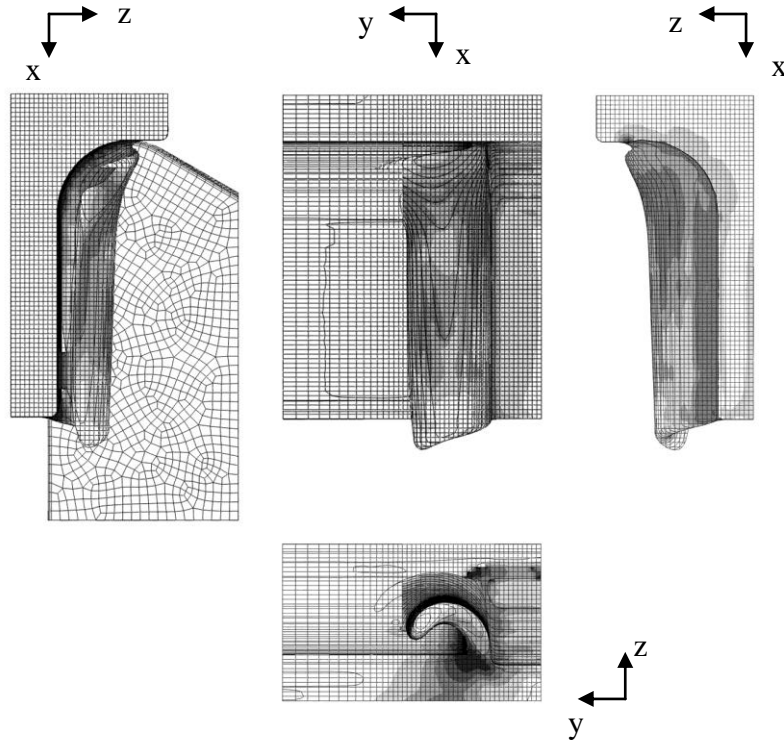


Figure 63 Chip formation at 525 μ s by different views

3.3.3 Comparison of Simulation Results

Cutting forces reached steady state quickly for both models. Forces predicted by the two models are comparatively close, especially for the feeding forces and back forces as shown in Figure 64. The comparison of the other results is summarized in Table 8. Chip thickness is measured at the primary cutting zone.

Table 8 Predicted results of ALE, CEL models at time=0.3ms.

	Chip thickness [mm]	Max Stress [MPa]	Max Strain [-]	Max Temp [°C]
ALE	0.21	1000	4	900
CEL	0.24	1100	4.5	980

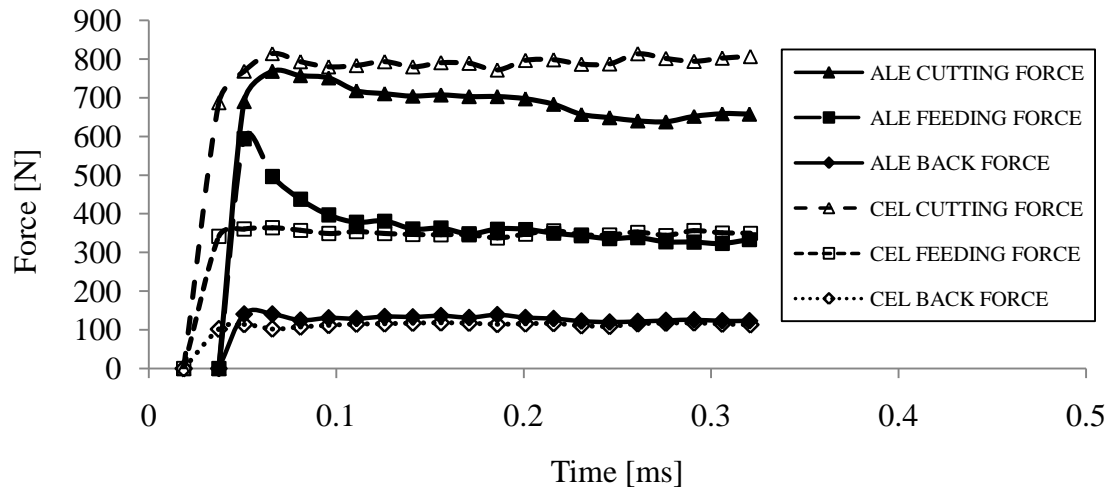


Figure 64 Predicted forces of both ALE and CEL 3D models

CHAPTER 4 DISCUSSIONS

4.1 Natural Transition Friction Model

In chapter 2 of literature reviews the existing models for friction between the workpiece and the tool were discussed. In this chapter a new friction model called Natural Sliding/Sticking Transition friction model will be proposed.

There are two approaches to investigate the tribological phenomena. The first approach is using the cutting process itself, such as measuring the feed/normal forces directly of the tool in an orthogonal cutting process and split-tool test in which the stress distribution on the tool can be derived from the force measurements. The second approach is to use laboratory tests with special setups, such as pin-on-disc test and ring compression test. Cristino had done a detailed review on the common approaches of calibrating friction in metal cutting [40]. However most of these approaches such as pin-on-disc can only determine the overall COF instead of the local COF [40]. For example, the COF deduced by measuring the feeding & cutting forces in orthogonal cutting is actually the COF that Merchant proposed during the early stage of the study of metal removing, which is the ratio of the force tangent and the force perpendicular to the rack face. This COF doesn't reflect the actual ratio

of the shear stress and normal stress along the contact length because it's the ratio of the forces which include the effect of cutting edge radius and the entire rake face but not the ratio of stresses. Zemzemi and Hendrik proposed two new test setups independently for identifying metal cutting friction model [41, 42]. Zemzemi used a rounded pin to rub against a turning cylinder while Hendrik use the cutting tool itself to rub against the workpiece. However these two tests have the same problem as the pin-on-disc experiment. They can only provide information for the ratio of the resultant forces. On the other hand, the split-tool experiment gives insights of the distribution of the shear and normal stresses on the rake face. The COFs deduced by the ratio of the stresses is thus the local COF along the contact length. Özel investigated the influence of different friction models on FE simulations of machining and concluded that simulations based on the measured normal and frictional stresses were generally more accurate when compared with those which are based on characterization procedures [24]. Thus, the split-tool experiment is the most proper experiment to study the phenomena of friction in metal cutting.

The experiment result of the split-tool experiment done by Buryta [32] is showed in Figure 65. Within the contact length, which is 1mm in this case, the normal pressure can easily exceed 100MPa even in the low pressure zone or sliding zone. This value is much higher than those that could possibly

achieved by using conventional dry slide friction tests and most of the pin-on-disc experiments which are aiming at metal cutting friction identification. The severe conditions involved, including the extreme pressure and temperature are really difficult to duplicate in laboratory tests such as pin-on-disc. Thus, again the current laboratory tests are improper approaches in determining the friction behavior of metal cutting.

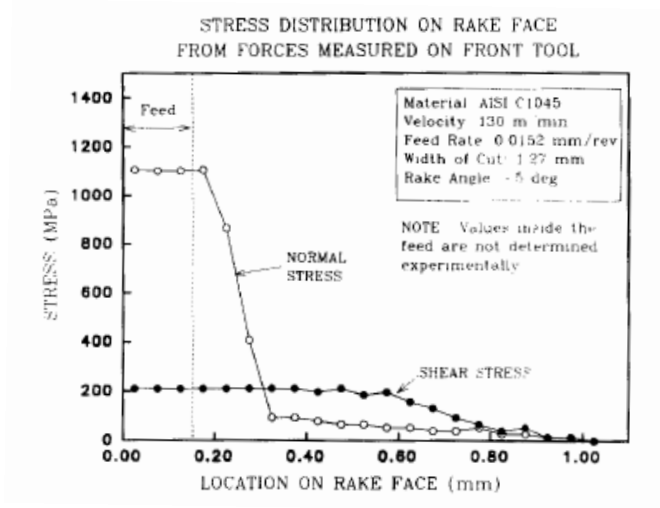


Figure 65 Stress distributions from rear tool forces: AISI C1045 [32]

The global friction coefficient is always smaller than 1 for typical machining processes. This seems to fit one's intuition based on everyday experience of friction. However, there is a common agreement between different researchers that the COF in the low stress friction area is greater than 1 for non-free-cutting mild steels based on split-tool experiments and

photoelastic experiments. Figure 65 and Figure 66 showed the results of the split-tool experiments done independently by Childs and Buryta [31, 32].

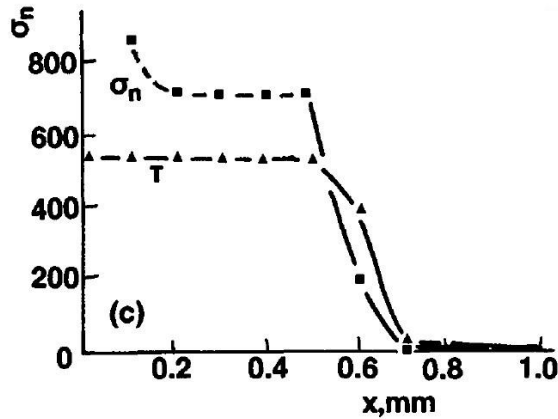


Figure 66 Distribution of normal stress and shear stress along the contact length of mild steel [31]

The x-axis is the length along the tool rake face; the origin point represents the cutting edge of the tool. In both cases as shown in Figure 65 and Figure 66, when look from the right to the left, the friction shear is greater than the normal stress before it saturates at certain value that related to the shear flow stress of the material on the rake face. After the shear stress saturates a plateau is formed. The normal stress grows to a much higher value when compared with the shear stress as the hydro static pressure can grow without limit. This cross over pattern of shear/normal stress implies the variation of the local COF as well as the change of mechanics of friction along the length. When the friction shear is lower than the material flow shear stress

the relative motion of the workpiece and the tool happens at the interface of the workpiece and the tool, which is referred as sliding zone by many authors [24]. In this region the nature of friction is related to both the tool and the workpiece and how they interact. As the normal stress increases the friction shear stress increases as well, until it exceed the limit of the workpiece shear flow stress. Then the relative sliding happens inside the workpiece material because the workpiece material can no longer hold itself together under such an enormous friction shear. The material immediately adjacent to the tool will stick to the rake face and thus the sticking region is formed. In this region the nature of friction is no longer related to the interface of the tool-workpiece but is purely related to the workpiece material properties.

For the past metal cutting FE simulation works done by numbers authors[34], medium carbon steels such as AISI 1045 and AISI 4140 were used as the workpiece and various friction models were employed, none of them can capture the shear and normal stresses cross over pattern as measured in the split-tool experiments as shown in Figure 65 and Figure 66 [43-45]. This obvious discrepancy in the stress pattern implies that the current friction models must be questionable. The past work simulation results of the shear stress and normal stress along the contact length from three different authors can be seen in Figure 67, Figure 68 and Figure 69.

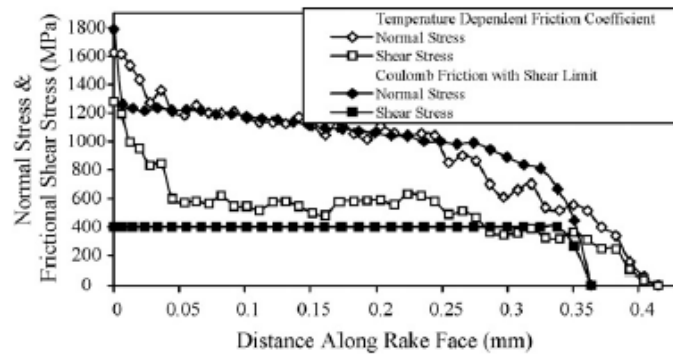


Figure 67 Predicted contact stress [44]

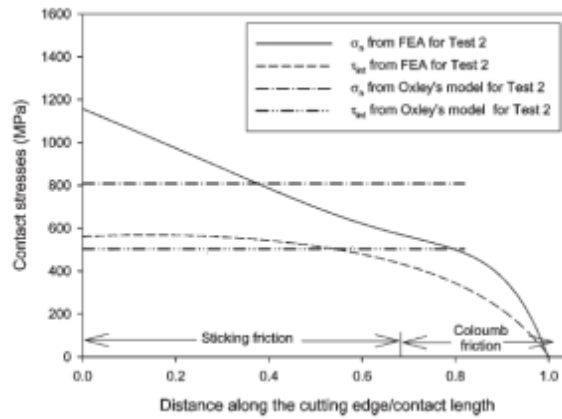


Figure 68 Predicted contact stress [45]

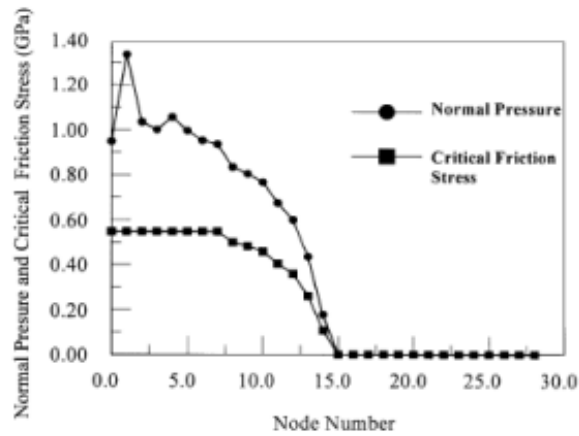


Figure 69 Predicted contact stress [43]

Many authors assert that the local COF can be a function of sliding

velocity and normal stress as shown in Eq.13:

$$\mu = f(V_s, \sigma_n), \quad \text{Eq. 13}$$

The sensitivities of friction to sliding velocity can be observed in many experiments. For example, Zemzemi measure the apparent friction coefficients at different speed by rubbing a pin against a rotating cylinder [41].

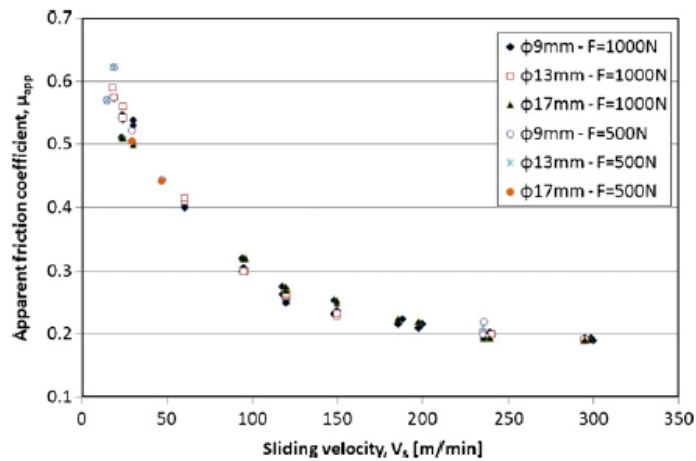


Figure 70 Apparent friction coefficient vs. sliding velocity [41]

Although Zemzemi's experiment doesn't directly show how the local friction coefficient varies as the sliding velocity changes, it does reflect the trend of the frictional phenomena versus the sliding velocity. It is clear that friction is strongly influenced by sliding velocity while the slope becomes much smaller which indicates a modification of the frictional behavior [41]. Although the reason for such modification of the frictional behavior is not understood, it is reasonable to assume that the friction behavior including the

local COF doesn't change in high speed machining with a cutting speed of 200 m/min or higher. Thus Eq.14 can be simplified as for high speed machining

$$\mu = f(\sigma_n), \quad \text{Eq. 14}$$

In the sliding region the friction shear stress is a function of contact pressure. This relationship can be as simple as a linear relationship which implies the local COF is independent of the contact pressure, not always, but within the same friction mechanism region. For example, in dry friction where the apparent pressure is very low, the COF is a constant even the apparent pressure increases or decreases, as long as the friction mechanism doesn't change. The same character might also be true within the intermediate contact pressure domain. Zemzemi from experimental analysis showed that friction is not significantly affected by contact pressure [41]. However, the contact pressure varies for a very large range from the low contact pressure to the intermediate domain and then to the high contact pressure in metal cutting. Thus the variation of COF is not negligible along the length of the sliding region. This variation of COF can be observed from the Figure 65.

Instead of expressing the COF as a empirical function of contact pressure the relationship between the friction shear stress and the contact pressure can be found by extracting the data from Figure 65 directly. Tabulated data as shown in Table 9 can then be used in the FE cutting model.

Table 9 Extracted shear stress and normal stress data from plot [32]

σ_n [MPa]	0	5	11	17	24
τ_{fric} [MPa]	0	13	47	104	190
Local COF	-	2.6	4.3	6.1	7.9

Simulation Results

Figure 71 is a plot of the friction shear and contact normal of the FE simulation. It is plotted with the same manner as the results from the split-tool experiments. The dash line on the left represent the end of the cutting edge radius and the dash line on the right marks the feed of 0.1mm. When compared with the experiment result the quantity and quality similarities are obvious for the simulation results, the important cross-over pattern can be seen as well.

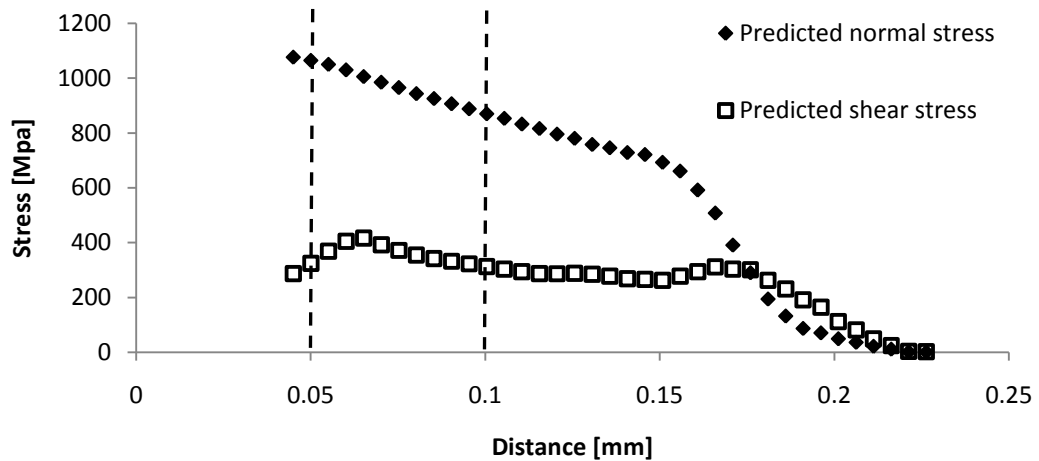


Figure 71 Expected normal stress and shear stress along contact length by natural transition model

The shear stress is initially greater than the normal stress and then saturates at about 300MPa which relates to the local shear flow stress of the workpiece material, as shear happens in the workpiece material but transferred to the rake face of the tool. The boundary of the sticking region and the sliding region was at 0.17 mm where the plateau of the friction shear starts to form. The location of the boundary of the two distinct regions is not pre-assumed but a result of the simulation. The sticking region can also be confirmed by the velocity contour plot as in Figure 72.

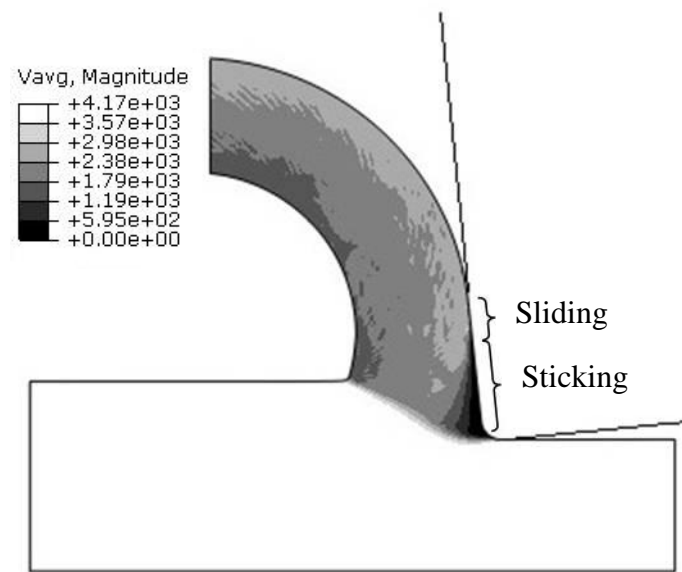


Figure 72 Velocity distribution of natural transition friction model

Within the sticking region, the workpiece material has zero velocity adjacent to the tool, in another word, the material sticks to the rake face of the stationary tool and thus the sticking region forms. The global friction COF can

be estimated by ratio of the integration of both stresses along the contact length. The estimated global COF is about 0.43 which is smaller than 1 and thus agrees with the global COF results of the experiments. This new model of friction in metal cutting is called Natural Sliding/Sticking Transition friction model.

The predicted contact length is much smaller than Figure 65 in which the depth of cut is 0.15 mm. The most likely reason that is responsible for the underestimated contact length is the ignorance of the self-contact of the chip and the workpiece. In the simulation the chip has an Eulerian surface that allows material to exit, the contact between the chip and the surface of the workpiece is ignored. However the contact may play a very important role in determining the contact length as illustrated in Figure 73.

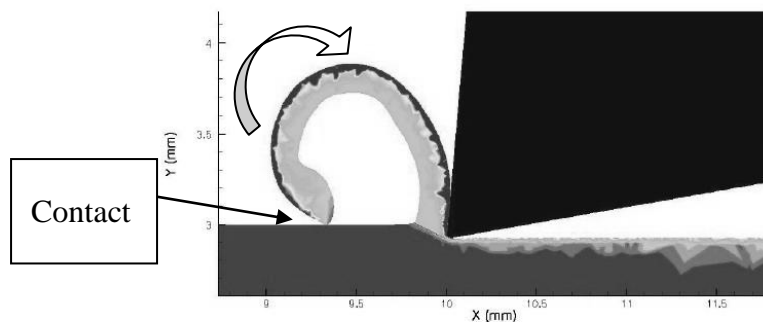


Figure 73 Self-contact that bend the chip over [1]

The question now is that if the friction phenomena can be so easily simulated by simply increase the COF to values higher than 1 then why the constant friction COF with limited shear stress model is so commonly in FE

metal cutting simulations. The reason behind it is probably rooted in the Lagrangian formulation used in early simulations. Lagrangian formulation is not capable to simulate the sticking behavior in the sticking zone, if it did, the mesh would distort excessively as the nodes of the workpiece at the workpiece-tool interface stick to the surface of the tool and the model will crash. In order to artificially imitate the saturated friction shear and prevent the model from crashing the critical shear is introduced, it not only imitate the shear flow stress of the material but also allow the workpiece material nodes along the interface to slide on the rake face instead of sticking to it. As all the relative motions of the workpiece and tool happen at the interface, no severe element distortion will occur inside the workpiece and thus the model will not crash. On the other hand the ALE formulation can actually allow the sticking behavior in the simulation, nodes and material flow are independent thus stagnation and sticking effect of the workpiece material can be addressed properly. Researchers may not have realized this advantage of ALE formulation and have kept using the friction models from Lagrangian models. Therefore it is no longer necessary to rely on the conventional models which were developed for Lagrangian models for the sake of element distortion. One should take advantage of the ALE formulation and apply Natural Sliding/Sticking Transition friction model to the metal cutting simulations.

4.2 MATERIAL MODEL

All the simulation conducted in this study used JC's equation to describe the plastic behaviour of the workpiece. As discussed earlier in chapter 1, JC's equation doesn't capture the blue brittleness effect of low carbon steels while there are other models including the modified JC's equation that does include the blue brittleness effect.

$$\sigma^0 = (B\bar{\epsilon}_{pl}^n) \left[1 + C \ln \left(\frac{\dot{\bar{\epsilon}}_{pl}}{\dot{\epsilon}_0} \right) \right] \left[\left(\frac{T_{melt} - T}{T_{melt} - T_{ref}} \right) + a e^{-0.00005(T-700)^2} \right], \quad \text{Eq.5}$$

where the parameters of this equation are summarized in Table 10[22].

Table 10 Parameters for equation (4) for AISI1045

B (MPa)	C	n	a
996.1	0.097	0.168	0.275

By superimposing the curve of the equation on the top of the experimental results from Jasper[33] the validation of such model can be confirmed. A power of 1.2 is added to the temperature term of equation (4) to yield a better fit as showed in Figure 74. Thus the equation becomes:

$$\sigma^0 = (B\bar{\epsilon}_{pl}^n) \left[1 + C \ln \left(\frac{\dot{\bar{\epsilon}}_{pl}}{\dot{\epsilon}_0} \right) \right] \left[\left(\frac{T_{melt} - T}{T_{melt} - T_{ref}} \right)^{1.2} + a e^{-0.00005(T-700)^2} \right], \quad \text{Eq. 15}$$

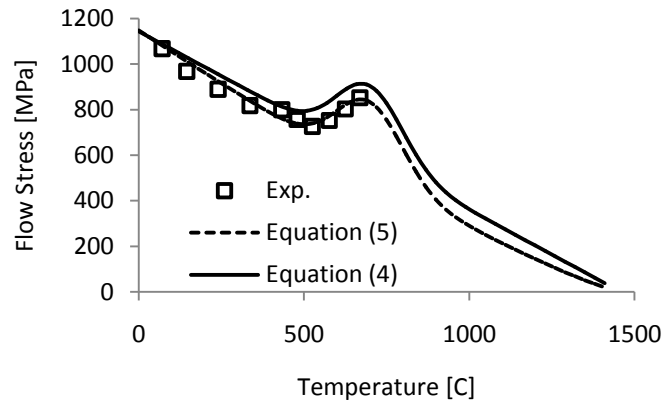


Figure 74 Flow stress versus temperature for AISI1045 at strain rate of 7.5.

Eq.15 was then used in the 2D ALE model instead of the conventional JC's model. The effect of changing the material model is obvious. Not only the stress distribution changed even the shape of the chip changed as well as shown in Figure 75. The cutting simulation is thus determined as very sensitive to the material model. Thus more attention should be put on the study of workpiece material constitutive law in the future studies. In the simulation result a build-up edge appeared in front of the tool by showing the velocity distribution of the workpiece material as shown in Figure 75. Although the presence of the BUE doesn't agree with the available experimental results, it shows the unique capability of ALE model of simulating BUE when compared with Lagrangian formulation.

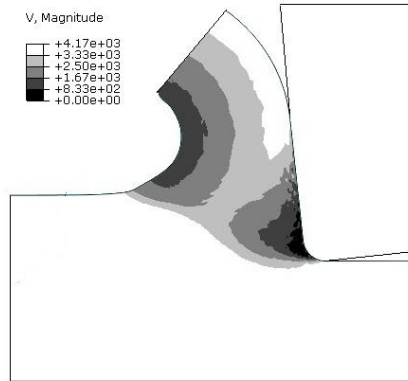


Figure 75 Velocity contour plot reveals the BUE

4.3 Robustness and Limitations of Mesh Smooth Methods

The number one cause of the unexpected termination of 3D ALE is element distortion. Although the mesh smooth methods in 2D models are very robust, it does have some problems when it is applied in 3D model. The goal of the mesh smooth methods is to limit the distortion and maintain the aspect ratio of the elements, but ironically the mesh smooth methods sometimes will actually crash the elements other than prevent the elements from crashing. There are three different mesh smooth methods available in ABAQUS but all of them induced similar problematic results.

To demonstrate this problem, 100 initial sweeps of mesh smoothing will be applied to the workpiece, there is no relative motion between the workpiece and the tool during the simulation, therefore there will be no

stresses nor deformations induced in the workpiece. The motion of the mesh is not a result of the deformation of the material but purely a result of the mesh smooth method, thus the mesh smooth method can be examined exclusively.

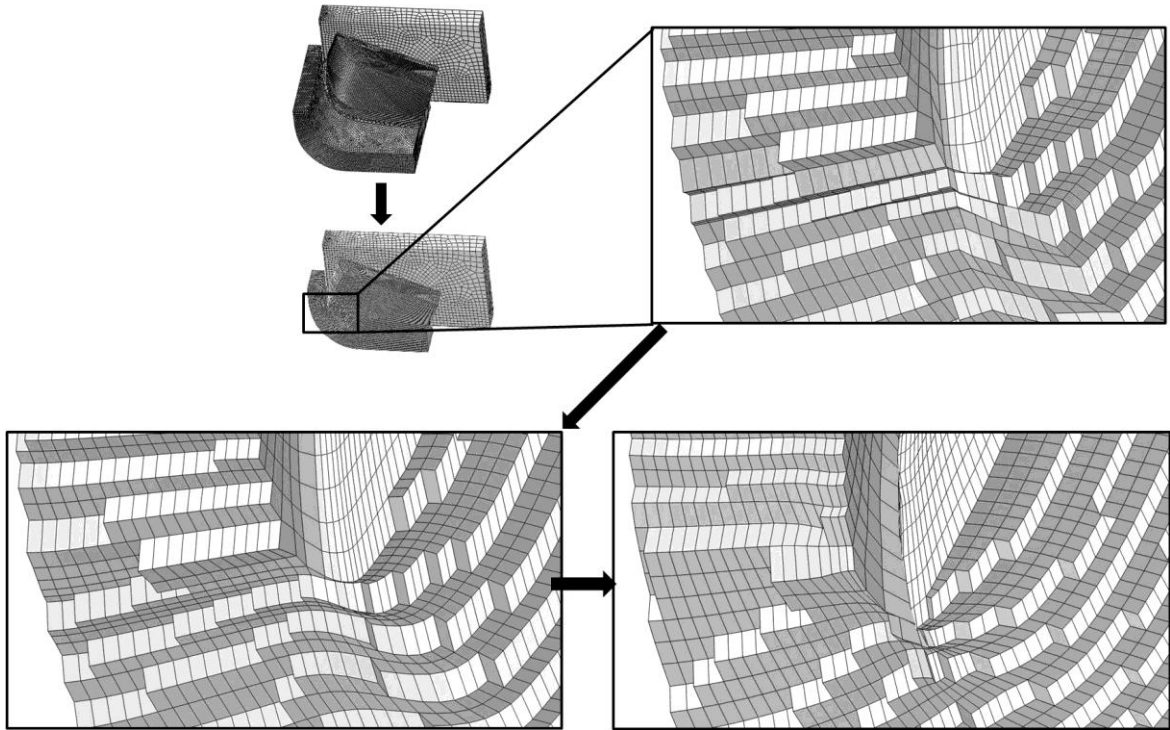


Figure 76 Test of the mesh smooth method in 3D

The first frame in Figure 76 shows the initial mesh before any smoothing actions, the second frame shows the mesh after 10 sweeps of mesh smoothing action, i.e. 10 times of the mesh smooth method has been applied, and the third frame shows the mesh after 100 sweeps. Half of the elements in the front are hidden to reveal the inner problematic area. It's not hard to see the crashed elements in the last frame, and the simulation crashed eventually even without any physical deformations. This kind of faulty mesh smoothing had

never been observed in 2D models it only happens in 3D models. The exact reason of this problem is unknown. But this problem in 3D models is worth more attentions in the future. One of the possible causes could be the regionally uneven distribution of elements. In the initial mesh there are regions which are much denser than the other regions when the size of the elements are compared. The driven force from this regionally uneven distribution is large and some elements at special locations will be sacrificed for the benefit of the majority. For example the elements at the bend can be stretched from both sides as illustrated in the 2D example in Figure 77.

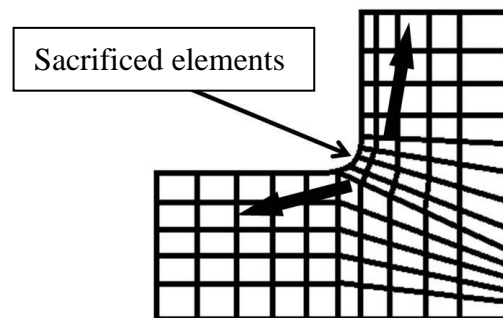


Figure 77 2D example of the problematic mesh smooth method

Black arrows represent driven "force" of the motion of the nodes, the smaller elements at the bend will be stretched. New mesh smooth mesh may be developed to resolve this problem in three dimensional mode but it is out of the scope of this study. The immediate and probably the easiest solution for this problem is to use similar element size throughout the entire part.

4.4 Limitations of CEL Formulation

Although CEL formulation can simplify the modeling process quite a lot, it is worth to point out some of its limitations in modeling metal cutting process. Since the boundary of the Eulerian material is estimated by the volume fraction of the elements and represented by simple planes in each elements some of the details of the Eulerian material will be lost.

Example in Figure 78 shows how a rectangular reference part is converted to volume fractions for each element. Calculated material boundary is no more a rectangular, the corners are rounded. The approximation can be more realistic if finer elements are used as showed in Figure 79.

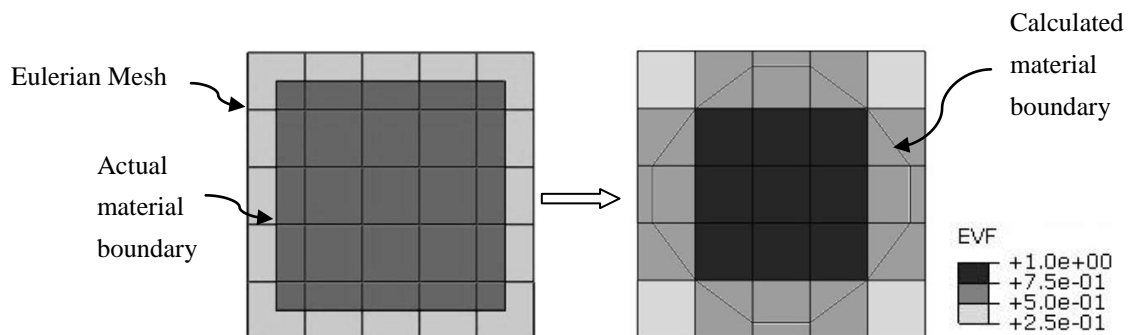


Figure 78 Surface approximation base on volume fraction

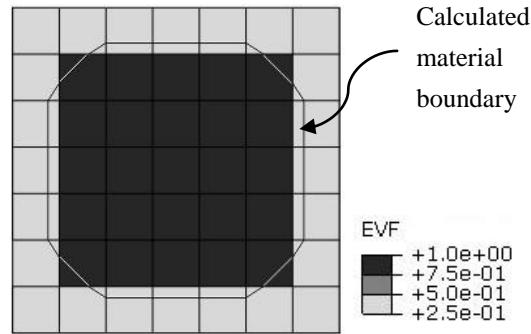


Figure 79 Better boundary approximation with finer mesh

In chapter 3, both 2D CEL and semi-3D CEL models have a much lower strain and temperature along the workpiece/tool interface when compared with the ALE models. Although basic dry friction FE simulations by both CEL and ALE formulations were performed and both results agree with the dry friction model, the reason why CEL models underestimated the strain and temperature is still unknown. It was discovered that the discrepancies disappear when the COF of zero is used for both ALE and CEL model. Thus the discrepancies between CEL and ALE models have to be related to the CEL algorithm of surface interaction and especially related to friction between surfaces because all the discrepancies only happen to region close to the surface of the Eulerian material and such discrepancies disappears when COF was set to zero.

4.5 Proposed Procedure For Building 3D ALE Cutting Model

In chapter 3 the feasibility of building a 3D ALE cutting model was

confirmed. Initial mesh is still the main factor that will determine whether the model can successfully reaches steady state. Although a feasible method of constructing the initial geometry and mesh were proposed in chapter 3 it is not interchangeable when another cutting configuration is to be modeled. A lot of tuning or trials are required to obtain to usable initial mesh design. This is a very time consuming process. Thus the following procedure is proposed as in Figure 80, it ought to be a general procedure for modeling 3D ALE cutting models efficiently in the future.

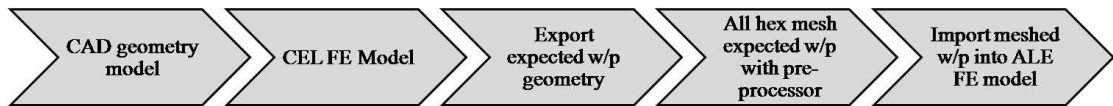


Figure 80 Flow chart of proposed 3D ALE modeling procedure

To build a 3D ALE cutting model, the CAD geometry models of the tools and the workpiece are first modeled base on the cutting configuration. Deformed workpiece which includes the chip geometry can be exported as the simulation result of the CEL model. The deformed workpiece geometry will be the initial geometry for the ALE model. All-hex mesh can then be generated automatically for the deformed workpiece by using Gregson's code. This initial mesh will be really close to the solution of the ALE, thus a successful ALE model is anticipated.

There are two gaps to be bridged before this procedure can be

conducted in the current stage of research. Firstly exporting the deformed geometry of a CEL model is not available in ABAQUS/CAE, thus a code that can convert the volume fraction output of the Eulerian material to a standard CAD file such as STL format or STEP format is required. Secondly, automatic all-hex mesh function is not yet available commercially, so assistances from the meshing researchers are needed. After these two gaps are bridged, the proposed procedure is anticipated to be the simplest way of building a 3D ALE cutting model.

4.6 Considerations of Efficiency Vs. Effectiveness

The advantages of FEM are the potential of saving money on purchasing physical experiment apparatus and the ability to reduce the time required for process optimization. In real industrial applications efficiency is as important as effectiveness, thus both the time spent on building and running models need to be taken into consideration, when evaluate the efficiency of conducting a FE analysis. In this study two new modeling techniques (CEL and ALE) are proposed for simulating 3D metal cutting processes. Information related to the labor hours of conducting each FE analysis are summarized in Table 11

Table 11 Simulation information for each models

Model type	2D		SEMI-3D		FULL 3D	
	ALE	CEL	ALE	CEL	ALE	CEL
Formulation	ALE	CEL	ALE	CEL	ALE	CEL
Number of elements	4353	10967	19569	163296	81133	132308
Smallest element size [mm]	0.004	0.01	0.02	0.02	0.03	0.05
Number of CPU's used	3	3	1	2	1	3
Increment size [s]	2.7E-10	3.6E-10	1.3E-9	1.7E-9	4.6E-10	4.6E-10
Time span of simulation [s]	0.0016	0.0016	0.001	0.001	0.0003	0.0006
Computational time [hours]	1.2	14	3.2	21	17	16.5
Estimated modeling time [hours]	2	0.5	4	1	40	1
Total hours for simulating 0.001s.	2.8	9.3	7.2	22	96	28

For 3D analysis, it's generally more favorable to use CEL formulation because it's less costly than ALE formulation if man hour is considered. However, as far as the computational time is concerned ALE formulation is superior and if the proposed procedure in section 4.5 can be successfully conducted, the man hour for building ALE models will be cut down dramatically. CAE engineers should base on their actual situations to determine whether 2D or 3D model is required and which formulations to be used.

CHAPTER 5 CONCLUSIONS & FUTURE WORK

- It's proved that ALE formulation can be used to model 3D metal cutting process and there is almost no available models of this kind can be found in the literature.
- Acquiring the initial geometry, initial mesh and mesh smooth method are the three important factors which determine a successful 3D ALE cutting model.
- The current available mesh smooth methods are not sophisticated enough to handle complex 3D geometries and can even crash the model in some circumstances.
- CEL formulation was successfully employed in modeling 3D metal cutting process. The simplicity of the process for constructing a 3D cutting model by CEL has been demonstrated. The solutions by using CEL formulation are generally similar to those by using ALE formulation while the reliability of CEL contact algorithm in modeling metal cutting is still questionable.
- Natural transition friction model has been proposed. This new friction model can capture the sticking and sliding zones at the tool/workpiece interface without predefinition. The cross pattern of the shear and normal

stresses along the contact length from split-tool experiments can also be captured.

- Modified Johnson-Cook's model has to be used in order to capture the blue brittleness effect of low carbon steels and the FE models are sensitive to the modification.
- 3D FE models are generally very costly in both man hour and computational time when compared to 2D models.
- There is a lot of room for improving the 3D ALE modeling procedure so that the process of building a 3D ALE cutting model takes less time and efforts but with a higher chance of successful completion.

FUTURE WORK

- A further study of proper material constitutive laws should be carried out.
- 3D models created by CEL and ALE formulations should be compared with the experiments.
- The limitations and solutions for such limitations of CEL formulation need to be studied further.
- Lagrangian surface can be included in to the CEL model on the top of workpiece to study the effect of self-contact of the workpiece and the chip tip on the formation of the chip.
- Method for all hex mesh generation and more effective mesh smooth method for 3D ALE model are to be explored so that the procedure proposed in section 4.5 can be carried out.

REFERENCES

1. Chen C.K.M., *Analysis of the metal cutting process using the shear plane model*, *Mechanical Engineering* 2010, Montana State University.
2. Merchant, M., *Mechanics of the Metal Cutting Process*, *Journal of Applied Physics*, 1945: p. 267-275.
3. Movahhedy M.R., Gadala M.S., Altintas Y., *Simulation of the orthogonal metal cutting process using an arbitrary Lagrangian-Eulerian finite-element method*, *Journal of Materials Processing Technology*, 2000, **103**: p. 267-275.
4. Nasr M.N.A., Ng E., Elbestawi M.A., *Modelling the effects of tool-edge radius on residual stresses when orthogonal cutting AISI 316L*, *International Journal of Machine Tools and Manufacture*, 2007, **47**(2): p. 401-411.
5. ABAQUS, *ABAQUS Documentation V6.12*. 2012.
6. Raczy A., Elmadagli M., Altenhof W.J., Alpas A.T., *An Eulerian Finite-Element Model for Determination of Deformation State of Copper Subjected to Orthogonal Cutting*, *Metallurgical And Materials Transactions A*, 2004, **35A**: p. 2393-2399.
7. Benson D.J., Okazawa S., *Contact in a multi-material Eulerian finite element formulation*. *Computer Methods in Applied Mechanics and Engineering*, 2004, **193**(39-41): p. 4277-4298.
8. Kim K.W., Lee W.Y., Sin H.C., *A finite-element analysis of machining with the tool edge considered*, *Journal of Materials Processing Technology*, 1999. **86**: p. 45-55.
9. Simoneau A., Ng E., Elbestawi M.A., *Grain Size and Orientation Effects When Microcutting AISI 1045 Steel*, *CIRP Annals - Manufacturing Technology*, 2007, **56**(1): p. 57-60.
10. Ng E., Aspinwall D.K., *Modelling of hard part machining*. *Journal of Materials Processing Technology*, 2002, **127**: p. 222-229.
11. Movahhedy M.R., Gadala M.S., Altintas Y., *Simulation of chip formation in orthogonal metal cutting process: an ALE finite element approach*, *Machining Science and Technology*, 2000, **4**: p. 15-42.
12. Arrazola P.J., Ugarte D., Domínguez X., *A new approach for the friction identification during machining through the use of finite element modeling*, *International Journal of Machine Tools and Manufacture*, 2008, **48**(2): p. 173-183.
13. Buchkremer, S., Wu B., Lung D., Munstermann S., Klocke F., Bleck W., *FE-simulation of machining processes with a new material model*, *Journal of Materials Processing Technology*, 2014, **214**(3): p. 599-611.

14. Abouridouane, M., Klocke F., Lung D., Adams O., *A new 3D multiphase FE model for micro cutting ferritic–pearlitic carbon steels*, CIRP Annals - Manufacturing Technology, 2012, **61**(1): p. 71-74.
15. E. Ceretti, C.L., L. Menegardo, T. Altan, *Turning simulations using a three-dimensional FEM code*, Journal of Materials Processing Technology, 2000, **98**: p. 99-103.
16. Fang, G., P. Zeng, *Three-dimensional thermo–elastic–plastic coupled FEM simulations for metal oblique cutting processes*. Journal of Materials Processing Technology, 2005, **168**(1): p. 42-48.
17. Soo, S.L., Aspinwall D.K., Dewes R.C., *3D FE modelling of the cutting of Inconel 718*. Journal of Materials Processing Technology, 2004, **150**(1-2): p. 116-123.
18. Maurel-Pantel, A., Fortaine M., Thibaud S., Gelin J.C., *3D FEM simulations of shoulder milling operations on a 304L stainless steel*. Simulation Modelling Practice and Theory, 2012, **22**: p. 13-27.
19. Sartkulvanich, P., Altan T., Göçmen A., *Effects of flow stress and friction models in finite element simulation of orthogonal cutting—a sensitivity analysis*, Machining Science and Technology, 2005, **9**(1): p. 1-26.
20. Johnson G.R., Cook W.H., *A constitutive model and data for metals subjected to large strain, high strain rate and high temperature*, Seventh International Symposium on Ballistics. 1983: Hague, Netherlands. p. 541-547.
21. Zerilli F.J., Armstrong R.W., *Dislocation-mechanics-based constitutive relations for material dynamics calculations*, J. Appl. Phys., 1987, **61**: p. 1816-1825.
22. Sartkulvanich P., Koppka F., Altan T., *Determination of flow stress for metal cutting simulation—a progress report*, Journal of Materials Processing Technology, 2004, **146**(1): p. 61-71.
23. Klocke, F., Lung D., Buchkremer S., *Inverse identification of the constitutive equation of inconel 718 and AISI 1045 from FE machining simulations*, Procedia CIRP, 2013, **8**: p. 212-217.
24. Özel, T., *The influence of friction models on finite element simulations of machining*, International Journal of Machine Tools and Manufacture, 2006, **46**(5): p. 518-530.
25. Shaw, M.C., *Metal Cutting principles*. Oxford Series on Advanced Manufacturing. 2005.
26. Childs T.H.C., *Friction modelling in metal cutting*, Wear, 2006, **260**(3): p. 310-318.
27. Zorev, N.N., *Interrelation between shear processes occurring along tool face and on shear plane in metal cutting*, ASME, 1963, p. 42-49.
28. Usui E., Shirakashi T., *Mechanics of machining - from descriptive to predictive theory. in on the art of cutting metals - 75 years later*, ASME Publication PED, 1982. **7**: p. 13-35.

29. Dirikolu M.H., Childs T.H.C., Maekawa K., *Finite element simulation of chip flow in metal machining*, International Journal of Mechanical Sciences, 2001, **43**: p. 2699-2713.
30. Kato S., Yamaguchi K., Yamada M., *Stress distribution at the interface between tool and chip in machining*, J. Eng. Ind., Trans. ASME, 1972: p. 683.
31. Childs T.H.C., Mahdi M.I., Barrow G., *On the Stress Distribution Between the Chip and Tool During Metal Turning*. CIRP Annals - Manufacturing Technology, 1989, **38**(1): p. 55-58.
32. Buryta D., Sowerby R., Yellowley I., *Stress Distributions on the Rake Face During Orthogonal Machining*, International Journal of Machine Tools and Manufacture, 1994, **34**: p. 721-739.
33. Jaspers S.P.F.C, Dautzenberg J.H., *Material behaviour in conditions similar to metal cutting: flow stress in the primary shear zone*. Journal of Materials Processing Technology, 2000, **122**: p. 322-330.
34. Tanu-Halim S.M., *Finite element modeling of the orthogonal metal cutting process: modeling the effects of coefficient of friction and tool holding structure on cutting forces and chip thickness*, Masters Thesis, Department of Mechanical Engineering, McMaster University, 2008.
35. Jalili Saffar R., Razfar M.R., Zarei O., Ghassemieh E., *Simulation of three-dimension cutting force and tool deflection in the end milling operation based on finite element method*, Simulation Modelling Practice and Theory, 2008, **16**(10): p. 1677-1688.
36. Gregson J., Sheffer A., Zhang E., *All-Hex Mesh Generation via Volumetric PolyCube Deformation*, Eurographics Symposium on Geometry Processing 2011, **30**(5): p. 1407-1416
37. Nieser M., Reitebuch U., Polthier K., *CUBECOVER-Parameterization of 3D Volumes*, Eurographics Symposium on Geometry Processing 2011, **30**(5): p. 1397-1406
38. Li Y., Liu Y., Xu W., Wang W., Guo B., *All-Hex Meshing using Singularity-Restricted Fiel*, ACM Transactions on Graphics, 2012. **31**(6), Article 177.
39. Kalhori V., *Modelling and Simulation of Mechanical Cutting*, Ph.D. Thesis, Department of Mechanical Engineering, Lulea Tekniska University, 2001.
40. Cristino, V.A.M., Rosa P.A.R., Martins P.A.F., *Revisiting the Calibration of Friction in Metal Cutting*, Tribology Transactions, 2012, **55**(5): p. 652-664.
41. Zemzemi F., Rech J., Ben Salem W., Dogui A., Kapsa P., *Identification of a friction model at tool/chip/workpiece interfaces in dry machining of AISI 4142 treated steels*, Journal of Materials Processing Technology, 2009, **209**(8): p. 3978-3990.
42. Puls H., Klocke F., Lung D., *A new experimental methodology to analyse the*

- friction behaviour at the tool-chip interface in metal cutting*, Production Engineering, 2012, **6**(4-5): p. 349-354.
43. Shi G., Deng X., Shet C., *A finite element study of the effect of friction in orthogonal metal cutting*, Finite Elements in Analysis and Design, 2002, **38**: p. 863-883.
 44. Haglund A.J., Kishawy H.A., Rogers R.J., *An exploration of friction models for the chip–tool interface using an Arbitrary Lagrangian–Eulerian finite element model*, Wear, 2008, **265**(3-4): p. 452-460.
 45. Madhavan, V. Adibi-Sedeh A.H., *Understanding of Finite Element Analysis Results under the Framework of Oxley's Machining Model*, Machining Science and Technology, 2005, **9**(3): p. 345-368.